Dynamics of coronal transients as seen from space observations

A thesis

submitted for the degree of

Doctor of Philosophy

in

The Department of Physics,

Pondicherry University,

Puducherry - 605 014, India

by

Vaibhav Pant

Indian Institute of Astrophysics,

Bangalore - 560 034, India

October 2017

Dynamics of coronal transients as seen from space observations

Vaibhav Pant
Indian Institute of Astrophysics

Indian Institute of Astrophysics
Bangalore - 560 034, India

Title of the thesis	:	**Dynamics of coronal transients as seen from space observations**
Name of the author	:	**Vaibhav Pant**
Address	:	Indian Institute of Astrophysics II Block, Koramangala Bangalore - 560 034, India
Email	:	vaibhav@iiap.res.in
Name of the supervisor	:	**Prof. Dipankar Banerjee**
Address	:	Indian Institute of Astrophysics II Block, Koramangala Bangalore - 560 034, India
Email	:	dipu@iiap.res.in

Declaration of Authorship

I hereby declare that the matter contained in this thesis is the result of the investigations carried out by me at the Indian Institute of Astrophysics, Bangalore, under the supervision of Prof. Dipankar Banerjee. This work has not been submitted for the award of any other degree, diploma, associateship, fellowship, etc. of any other university or institute.

Signed: _____

Date: _____

Certificate

This is to certify that the thesis entitled **'Dynamics of coronal transients as seen from space observations'** submitted to the Pondicherry University by Mr. Vaibhav Pant for the award of the degree of Doctor of Philosophy, is based on the results of the investigations carried out by him under my supervision and guidance, at the Indian Institute of Astrophysics. This thesis has not been submitted for the award of any other degree, diploma, associateship, fellowship, etc. of any other university or institute.

Signed: _____

Date: _____

List of Publications

1. *Flows and Waves in Braided Solar Coronal Magnetic Structures*
   V. Pant, A. Datta and D. Banerjee, 2015, **The Astrophysical Journal Letters**, 801L, 2

2. *Dynamics of On-disk Plumes as Observed with the Interface Region Imaging Spectrograph, the Atmospheric Imaging Assembly, and the Helioseismic and Magnetic Imager*
   V. Pant, L. Dolla, R. Mazumder, D. Banerjee, S. Krishna Prasad and V. Panditi, 2015, **The Astrophysical Journal**, 807, 71

3. *MHD Seismology of a loop-like filament tube by observed kink waves*
   V. Pant, A. K. Srivastava., D. Banerjee, M. Goossens, P. F Chen, N. C Joshi, Y. H Zhou, **Research in Astronomy and Astrophysics**, 2015, 15 , 1713

4. *Propagating disturbances in the solar corona and spicular connection*
   T. Samanta, **V. Pant**, D. Banerjee, 2015, **The Astrophysical Journal Letters**, 815, L16

5. *The effects of transients on photospheric and chromospheric power distributions*
   T. Samanta, V. M. J. Henriques, D. Banerjee, S. Krishna Prasad, M. Mathioudakis, D. Jess, **V. Pant**, 2016, **The Astrophysical Journal**, 828, 23

6. *Reflection of Propagating Slow Magneto-acoustic Waves in Hot Coronal Loops: Multi-instrument Observations and Numerical Modeling*
   S. Mandal, D. Yuan, X. Fang, D. Banerjee, **V. Pant**, T. V. Doorsselaere , 2016, **The Astrophysical Journal**, 828, 72

7. *Transverse Oscillations in a Coronal Loop Triggered by a Jet*
   S. Sarkar, **V. Pant**, A. K Srivastava, D. Banerjee, 2016, **Solar Physics**, 291, 3269

8. *Simultaneous Longitudinal and Transverse Oscillations in an Active-Region Filament*
   V. Pant, R. Mazumder, D. Yuan, D. Banerjee, A. K Srivastava, Y. Shen, 2016, **Solar Physics**, 291, 3303

9. *Automated Detection of Coronal Mass Ejections in STEREO Heliospheric Imager Data*
   V. Pant, S. Willems, L. Rodriguez, M. Mierla, D. Banerjee, J. A Davies, 2016, **The Astrophysical Journal**, 833, 80

10. *First Imaging Observation of Standing Slow Wave in Coronal Fan Loops*
    V. Pant, A. Tiwari, D. Yuan, D. Banerjee 2017, **The Astrophysical Journal Letters**, 847L, 5

11. *Kinematics of Fast and Slow Coronal Mass Ejections in solar cycle 23 and 24*
    V. Pant, A. Chauhan, D. Banerjee, N. Gopalswamy 2016, **Journal of Geophysical Research**, under review

12. *Twisting/Swirling motions during a prominence eruption as seen from SDO/AIA and STEREO/EUVI*
    V. Pant, A. Datta, D. Banerjee, K. Chandrashekhar 2016, **The Astrophysical Journal**, under review

Conference Proceedings

1. *The inner coronagraph on board ADITYA-L1 and automatic detection of CMEs*
   D. Banerjee, R. Patel, **V. Pant**, ADITYA Team, 2017, **IAU symposium No. 335**, under review

Presentations

1. Poster presentation in the *Astronomical Society of India meeting 2014 (ASI:2014)* held at the IISER, Mohali, India, during 20-22 March, 2014.

2. Poster presentation in seventh *Solar Information Processing (SIP)* workshop held at La Roche-en-Ardenne, Belgium, during 18-21 August, 2014.

3. Poster presentation in the international conference on *Coupling and Dynamics of the Solar Atmosphere* held at the IUCAA, Pune, India, during 10-14 November, 2014.

4. Participated in the *India-China workshop on astronomy and astrophysics* held at the IIA, Bangalore, India, during 3-5 December, 2014.

5. Poster presentation in the *Astronomical Society of India meeting 2015 (ASI:2015)* held at the NCRA, Pune, India, during 17-20 February, 2015.

6. Oral presentation in the *Astronomical Society of India meeting 2016 (ASI:2016)* held at the Kashmir University, Kashmir, India, during 5-10 May, 2016.

7. Oral presentation in the *IBUKS meeting* held at the KU Leuven, Belgium, during 13-19 June, 2016.

8. Poster presentation in the *Astronomical Society of India meeting 2017 (ASI:2017)* held at the B. M. Birla Auditorium, Jaipur during 6-10 March, 2017.

9. Poster presentation in the *International Astronomical Union meeting on Space Weather of the Heliosphere: Processes and Forecasts (IAU:2017)* held at the university of Exeter, UK during 17-21 July, 2017.

Acknowledgements

I express my sincere thanks to my supervisor, Prof. Dipankar Banerjee (Dipu daa), for his guidance and encouragement during my PhD. I deeply thank him for sharing not only his research experiences but also personal experiences with me. I also thank all my collaborators for their valuable guidance. I would like to thank the referees of my papers and doctoral committee members for their insightful comments that have helped me to improve the quality of my research work. I would like to thank IIA for providing me with necessary facilities to carry out the research work. I am equally grateful to Royal Observatory of Belgium for hosting me on several occasions. They always made sure that my stay in the observatory was comfortable. Having said that, I am done with those who have explicitly helped me in my research work during the PhD. However, there are many people around me whose names can't be found in the author lists or acknowledgements of my papers. These people made the environment around me conducive for research. Therefore, I want to take this opportunity to thank them.

I acknowledge the support of my parents during my good and bad times. I am obliged to my sister and brother-in-law for inviting me during weekends and saving me from the hostel's food.

I am grateful to my present and past hostel roommates, T. Mageshwaran and Prassana Deshmukh. They never complained even when I played songs with speakers on or continued to work with lights on. I do not think one can get better roommates. I also acknowledge the time I spent with Sudip and Priyanka.

I am indebted to those who have listened to my neuroscience theories and have borne with me at lunch and dinner tables. I owe a million thanks to "Dipu da" for never discouraging me from reading neuroscience and psychology in spite of knowing that I spent more time on neuroscience than solar physics. I acknowledge

Tanmoy's courage for diligently listening to my theories especially on vitamin D. It was really great to spend time with him. I also extend my thanks to Rakesh, who always listened and supported my theories, though I don't know how much he has understood them.

I would also like to express my gratitude for Marilena, who accommodated me for a couple of days in her house at times when I needed it. I would like to thank Barnalli for patiently listening to my theories and complementing them with philosophical arguments. I am indebted to my friend–cum–counsellor Poulami, who has also patiently listened to my theories but in the end, she always proved them wrong by giving strong arguments, which can't be further argued on. Finally, I owe zillion thanks to Shweta, who supported and rejected my theories depending on her mood. I really enjoyed arguing and spending time with her in IIA.

I thank my juniors and project students, Ritesh, Ajay, Shilpa, Anwesha, and Radhika for not keeping any grudges against me even when I scolded them for some stupid reasons. I must confess that all of them are diligent and sincere.

I thank Anmol and Bhupendra for hilarious discussions that we had together.

I am grateful to Coursera for providing the world-class education for free. I want to particularly acknowledge the course on "Machine Learning" by Andrew Nag that has motivated me to pursue this subject in more detail.

Last but not the least, I am indebted and grateful to my grandmother, who continues to encourage me since my childhood. She is and will always be a source of inspiration to me.

Data Usage Acknowledgements

Data from several space-based instruments are used in the studies that are presented in this thesis. I acknowledge the usage of the data from these facilities. Furthermore, I thank the respective instrument team members for providing the data in the public domain.

The CDAW CME catalog used in this thesis is generated and maintained at the CDAW Data Center by NASA and The Catholic University of America in cooperation with the Naval Research Laboratory. SOHO is a project of international cooperation between ESA and NASA. This thesis uses data from the CACTus CME catalog, generated and maintained by the SIDC at the Royal Observatory of Belgium. HELCATS-FP7 catalog that is used in the thesis has received funding from the European Union's Seventh Framework Programme for research, technological development and demonstration under grant agreement no. 606692.

The SDO Data used is the courtesy of NASA/SDO and the AIA, EVE, and HMI science teams.

IRIS is a NASA small explorer mission developed and operated by LMSAL with mission operations executed at NASA Ames Research center and major contributions to downlink communications funded by ESA and the Norwegian Space Centre.

Dedicated to

my

Grandmother

Abstract

The thesis is focused on the study of the coronal transients at different spatial and temporal scales seen in different layers of the solar atmosphere using space-based imaging and spectroscopic instruments. The first part of the thesis is focused on the study of the dynamics of the small-scale coronal transients found in the solar atmosphere. We explored the interaction between different small-scale transients observed in different layers of the solar atmosphere. We studied the role of small-scale transients (transition region jets) in sustaining the propagating disturbances (PDs) in the coronal plumes. We explored the connection between transition region (TR) jets and the propagating disturbances (PDs) seen in an on-disk plume combining the observations of Interface Region Imaging Spectrograph (IRIS) and Solar Dynamics Observatory (SDO). We demonstrated that the PDs in plumes are the signatures of the slow magnetoacoustic waves which are connected with the reconnection outflows at the supergranulation boundaries, $i.e,$ TR jets. We presented one-to-one correspondence between TR jets and PDs at the footpoint of the plume.

We studied long-period (60 minutes) transverse oscillations in a coronal loop triggered by a coronal jet which carries much less energy than CMEs or blast waves. We found that the jet consisted of hot and cool components. Hot component of jet interacted with the coronal loop and triggered transverse oscillations. We estimated the energy density inside the loop and found that it was large enough to sustain the transverse oscillations. Thus we inferred that the coronal jet triggered the long-period transverse oscillations in the coronal loop.

We studied the quasi-periodic intensity disturbances of 20–25 minutes periodicity in the open magnetic structures such as fan loops. We showed that these intensity disturbances were the signatures of standing oscillations that were excited by transients such as EUV waves (blast waves) originating at a distant active region. This is the

first observation of standing oscillations in the coronal fan loops. Though, standing oscillations in the hot coronal loops (T$\sim$10 MK) were reported earlier.

The second part of the thesis is focused on the study of the large-scale coronal transients, i.e., coronal mass ejections (CMEs). CMEs are the large-scale eruptions of magnetic field and plasma from the atmosphere of the Sun to the heliosphere. Several automated detection algorithms exist to detect CMEs automatically in the coronagraph images. However, these methods could not be successfully implemented for detecting CMEs/ICMEs in heliosphere using inner Heliospheric Imager (HI-1) images due to heavy contamination of stars and planets. We developed an automated detection algorithm to detect CMEs in heliosphere using the data from HI-1 onboard Solar Terrestrial Relations Observatory (STEREO). We used the principle of Hough transform as implemented in Computer Aided CME tracking (CACTus) to detect CMEs in HI-1 images. We found that the output of automated catalog matches well with the manual catalog. The catalog is now running on real-time and is available for public use.
Finally, we studied the kinematics of fast and slow CMEs in solar cycle 23 and 24 using Coordinated Data Analysis Workshops (CDAW) and CACTus catalogs that list the properties of CMEs, which are manually and automatically identified, respectively, using Large Angle and Spectrometric Coronagraph (LASCO) C2 and C3 images. The width distribution of the CMEs is believed to follow a power law with power index of $\sim$-1.7. We reported that fast and slow CMEs have different power laws which could be due to their different energy sources. We also studied the rate of occurrences in the slow and fast CMEs in solar cycles 23 and 24. We found that cycle 24 is producing more slower CMEs as compared to cycle 23, which could be due to the weak heliospheric field.

Contents

List of Figures

List of Tables

Abbreviations

NASA	**N**ational **A**eronautics and **S**pace **A**dministration
SOHO	**SO**lar and **H**eliospheric **O**bservatory
EIT	**E**xtreme ultraviolet **I**maging **T**elescope
TRACE	**T**ransition **R**egion and **C**oronal **E**xplorer
STEREO	**S**olar **T**errestrial **R**elations **O**bservatory
SDO	**S**olar **D**ynamics **O**bservatory
AIA	**A**tmospheric **I**maging **A**ssembly
HMI	**H**elioseismic and **M**agnetic **I**mager
IRIS	**I**nterface **R**egion **I**maging **S**pectrograph
MHD	**M**agneto**H**ydro**D**ynamics
CCD	**C**harge **C**oupled **D**evice
EUV	**E**xtreme **U**ltra**V**iolet
UT	**U**niversal **T**ime
TR	**T**ransition **R**egion
$\mathbf{R}_\odot$	Solar **R**adius

Chapter 1

Introduction

The Sun is a main sequence star of spectral type G2V and absolute magnitude 4.8. It is about 4.6 billion years old having a mass of $\sim 1.99 \times 10^{30}$ kg, a radius of ∼696000 km, and an effective surface temperature of ∼5780 K. Unlike a solid body, it does not rotate uniformly at all latitudes. The equator of the Sun takes ∼25 days to complete one rotation while the poles take ∼35 days. The Sun is a huge ball of hot plasma. It mainly consists of 92.1% H and 7.8% He. The source of the energy of the Sun is the thermonuclear fusion happening at its core. It is our nearest star and Proxima Centauri is the nearest neighbour star (∼4.25 light-years away) of the Sun. Due to its close proximity to the Earth ($\sim 1.496 \times 10^{11}$ m), the Sun is observed in unprecedented details which have helped us to understand many astrophysical phenomena that happen on other stars. Next, the overall structure of the Sun is briefly described.

1.1 The solar interior

The solar interior broadly comprises the core, radiative zone and convective zone. The central part of the Sun is called core, where the temperature ($\sim$1.5$\times$10^7 K) and density ($\sim$160 g cm^{-3}) are high enough for thermonuclear reactions to happen. Beyond core, radiative zone extends from 0.25–0.7 $R_\odot$. In radiative zone, the energy transfer takes place by radiative diffusion. The gamma rays produced during thermonuclear fusion are absorbed and re-emitted. This process continues for millions of years till photons reach the surface of the Sun and escape to the interplanetary space. The gamma-ray photons loose energy in every collision. Therefore, by the time they reach the surface of the Sun, their wavelengths fall mostly in the visible range. Beyond radiative zone, the energy transfer takes place by convective motions. This region is termed as convection/convective zone (see Figure 1.1). It extends from $\sim$0.7 $R_\odot$ to the surface of the Sun. The core and radiative zone rotate uniformly while the upper layers of convection zone rotate differentially. These two regions are separated by a thin layer called Tachocline. Due to the large shear flows, the magnetic field of the Sun is believed to be generated in this layer.

1.2 The solar atmosphere

The solar atmosphere consists of four layers, namely the photosphere, chromosphere, transition region, and corona. The visible surface of the Sun is called photosphere. The photosphere is a layer with a depth of $\sim$500 km. The photosphere is the region where optical depth (τ_{5000}) at 5000 Å is equal to 1. When seen in high resolution, the photosphere appears to be covered with irregular granular structures. These patterns arise from solar convection and are termed as "granulation". The photosphere has an average temperature of $\sim$5700 K. It

also harbours sunspots, which are the regions of intense concentration of magnetic flux. They appear as dark spots on the surface of the Sun as shown in the Figure 1.1. The photosphere extends up to a layer, temperature minimum, where the temperature decreases to 4300 K. The chromosphere lies above the photosphere and extends from temperature minimum to the height where the temperature becomes ∼20000 K. The chromosphere is highly inhomogeneous and manifests different type of transients like spicules, mottles, filaments/prominences, fibrils etc. A narrow region of ∼100 km in thickness lies above the chromosphere and is called transition region. In this region, the temperature increases to 10^6 K and electron density rapidly falls off from 10^{11} cm^{-3} to 10^9 cm^{-3}. The outermost layer of solar atmosphere is called corona. It starts beyond transition region. Corona is heated to temperatures of $\sim 10^6$ K. Figure 1.2 shows the variation of the temperature and density in the solar atmosphere as proposed by Vernazza *et al.* (1981). Note that it is a one-dimensional model averaged over the quiet Sun. The actual variation may be different in the different regions and structures of the Sun. The mechanism of the heating of the solar corona is not well understood. Two possible scenarios proposed for the heating of the solar corona are: (a) energy dissipation from waves and (b) energy dissipation from magnetic reconnection. Electrons in the corona scatter off the photospheric light, therefore it can be seen in white light either during an eclipse or by creating an artificial eclipse using a coronagraph. The corona is also seen in extreme ultraviolet (EUV) radiation emitted by highly ionised Fe and other ions present in the corona.

The solar atmosphere is highly inhomogeneous and dynamic due to the presence of magnetic fields. Most of the structures found in the solar atmosphere such as sunspots, filaments, coronal loops, coronal streamers, and extreme events like flares owe their existence to the magnetic field. In past few years, with the launch of new space-based and ground-based instruments, it is now possible to study different structures in different layers of the atmosphere of the Sun with high spatial and temporal resolutions. One of the newly launched instruments, Interface

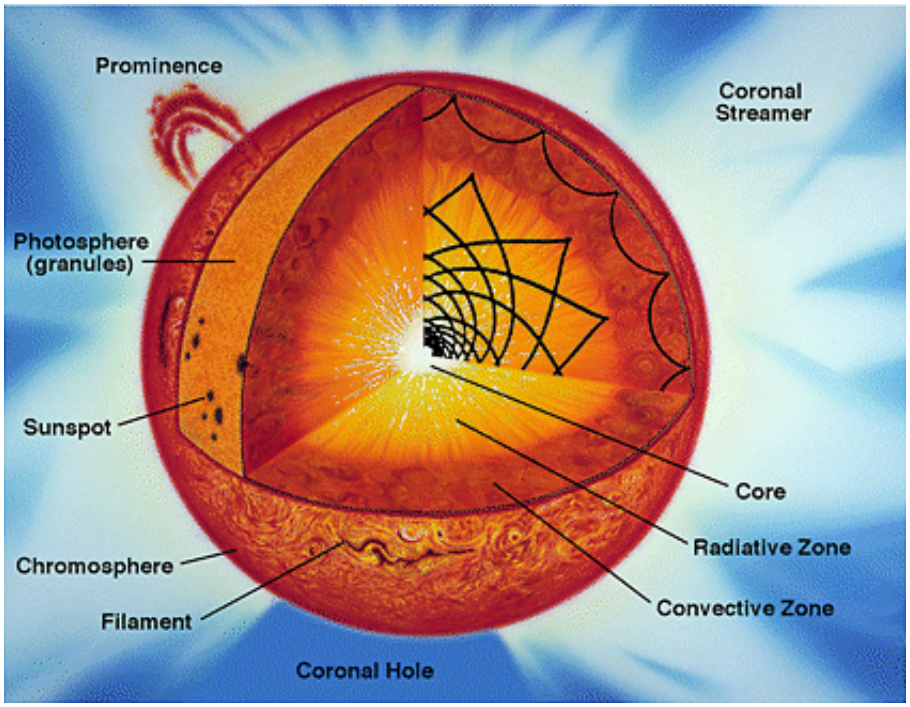

FIGURE 1.1: A sectional view of the structure of the Sun indicating its various layers. A few prominent features are also marked in the figure. *Credit*: `http://solar.bnsc.rl.ac.uk/sb99/people/KGalsgaa/sb99_num.html`

Region Imaging Telescope (IRIS), has greatly improved our understanding of the dynamics happening in the transition region of the Sun. Atmospheric Imaging Assembly (AIA) and Extreme Ultraviolet Imager (EUVI) have shed lights on the different transient phenomena happening in the chromosphere and corona. Such high-cadence and high-resolution observations covering photosphere to corona are required to study the features that change rapidly with time in different layers of the solar atmosphere.

In the next section, I will give a brief overview on the history of the solar transients.

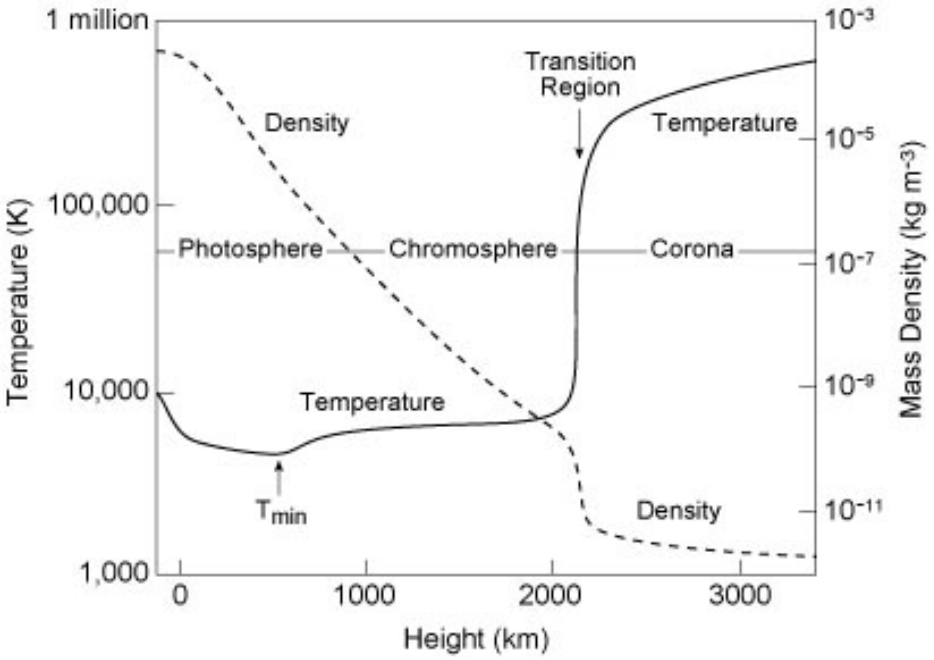

FIGURE 1.2: Temperature and density variation in the solar atmosphere. *Credit*: `https://ase.tufts.edu/cosmos/view_picture.asp?id=174`

1.3 Brief history of observations of solar transients

A transient is defined as a feature that varies rapidly with time. However, the term transient is relative and depends on the time scales with which comparisons are made. For example, the Sun is a transient on a cosmological timescale. In the context of this thesis, I define transients as the features on the surface and the atmosphere of the Sun that vary over a period of seconds to days. From spicules to coronal mass ejections (CMEs), transition region jets to sunspots; transients of different spatial and temporal scales are found in the solar atmosphere. Brightenings due to flares and waves can also be considered as transient features because they are short-lived and evanescent. The early observations of the transient features on the Sun are dated back to 1610 when Galileo began a systematic study of sunspots using the telescope. In 1844, Schwabe reported the periodic variation of the sunspot numbers over eleven years. The first-ever reported eruptive transient

phenomenon on the surface of the Sun was the observation of the brightenings associated with a solar flare recorded by R. C Carrington in 1859 (Carrington 1859). These brightenings were seen in white-light continuum and sustained for five minutes. In the last century, researchers have observed diverse features on the surface of the Sun due to the advent of high-resolution ground-based and space-based telescopes. Large scale chromospheric wave and its interaction with filaments were first reported by Moreton and Ramsey (1960). Later, Ramsey and Smith (1966) reported large amplitude long period oscillations in filaments in Hα. The authors termed them "winking" filaments because filaments disappeared and appeared in Hα passband periodically due to the large line-of-sight (LOS) velocity. By 1960s, spicules and their physical properties were studied in great detail using Hα observations (see Beckers 1968, for details). Macrospicules were first reported by Bohlin *et al.* (1975) using He II spectroheliograms obtained with extreme ultraviolet (EUV) spectrograph during the Skylab mission. As the technology advanced and the capability of instruments for making high-resolution observations were improved, different transient features were observed in the solar atmosphere such as explosive events (Brueckner and Bartoe 1983), EUV brightenings (Gallagher *et al.* 1999), X-ray jets (Shibata *et al.* 1992), propagating disturbances (PDs) in polar plumes (Deforest and Gurman 1998), PDs in coronal loops (Berghmans *et al.* 1999), and transverse oscillations in coronal loops (Nakariakov *et al.* 1999a) etc.
Apart from small scale transients as discussed above, large scale transients such as CMEs were also reported using eclipse observations and space-based telescopes. Although radio bursts and interplanetary shocks due to CMEs were observed as early as in 1947 (Payne-Scott *et al.* 1947; Sonett *et al.* 1964), first white light observation of CMEs was made by white light coronagraph on board Orbiting Solar Observatory (OSO–7) mission (Tousey 1973). After the launch of Solar and Heliospheric Observatory (SOHO) and Solar Terrestrial Relations Observatory (STEREO) in 1996 and 2006 respectively, CMEs have been routinely observed and studied.

1.4 Motivation

Having outlined a brief history of solar transients, in this section I will discuss the current understanding of solar transients and few long-standing problems that have motivated me to further explore the dynamics of solar transients.

In spite of decades of observations, our understanding of the solar transients is still poor. For example, the nature of PDs is still a matter of debate. Ofman *et al.* (1997); Deforest and Gurman (1998) interpreted PDs as the signatures of slow magnetoacoustic/compressive waves while Sakao *et al.* (2007); Tian *et al.* (2011a) interpreted them as quasi-periodic upflows. Recently, De Moortel *et al.* (2015) reported that it is not trivial to distinguish between waves and upflows using only imaging observations. They proposed a dual model, where upflows at the base of coronal loops generate slow magnetoacoustic waves that propagate along the loops (see also Nishizuka and Hara 2011). This model might account for the observational discrepancies found in the literature. However, this scenario has not been explored in greater detail. Apart from the nature of PDs, their sources are also not well understood. Deforest *et al.* (1997) observed that plumes are rooted in chromospheric network boundaries. Thus the PDs seen in plumes must be associated with the dynamics happening at the network boundaries. However one-to-one correspondence of PDs with network dynamics has not been established conclusively. Therefore, coordinated observations from different observatories covering photosphere to corona are required to understand the nature and origin of PDs in coronal plumes and coronal loops.

Solar transients also play an important role in sustaining large scale structures. Recent studies have shown that small scale transient features, "jetlets", help in sustaining large scale structures, plumes. A plume disappears shortly after the disappearance of these "jetlets" (Raouafi and Stenborg 2014). Such studies were possible due to high-resolution imaging capabilities of AIA and HMI on board Solar

Dynamics Observatory (SDO). In a recent study, a new class of transients called small-scale jets, with a lifetime of few seconds, were discovered in the solar network regions using IRIS instrument (Tian *et al.* 2014). These authors have shown that such small-scale jets carry enough mass to sustain the solar wind. The connection between small-scale jets in the network boundaries and the coronal features such as plumes rooted in the network boundaries, is not explored in greater details mainly because of lack of coordinated imaging and spectroscopic observations covering the chromosphere, transition region, and corona.

Transients interact with the magnetic structures present in the solar atmosphere. This interaction often excites waves. Transients like shock waves/blast waves and CMEs may excite transverse oscillations in coronal loops and prominences/filaments. Based on the interaction angle between the shock wave and filaments, it may generate longitudinal oscillations, transverse oscillations or both simultaneously (Shen *et al.* 2014; Pant *et al.* 2016a). A recent study by Zimovets and Nakariakov (2015a) has shown that the kink oscillations ($\sim$95%) were associated with CMEs, low coronal eruptions, such as plasma ejections. However, it is not yet properly understood if such low coronal eruptions have enough energy to excite transverse oscillations in the coronal loops. In addition to transverse oscillations, transients like a flare at one or both footpoints may produce reflecting or standing waves in hot and flaring coronal loops (Kumar *et al.* 2013; Fang *et al.* 2015; Mandal *et al.* 2016). Such oscillations are heavily damped and have been exclusively seen in hot and flaring coronal loops. There are only a few reports of such oscillations because of observational limitations. Thus, excitation mechanisms for these waves are also not well studied.

Transients also affect the space weather. Space weather describes the phenomena or time varying conditions happening in the outer space that impact the systems and technologies on the Earth and in the space. Large scale transients (CMEs) are important to understand the variability of the space weather. An Earth-directed

CME may disrupt the communications and cause massive power blackouts. With increasing dependence on the technology, it has now become quite imperative to monitor CMEs in the heliosphere. The first step towards monitoring CMEs is to identify them in the coronagraph images. An automated detection is faster and more objective than visual inspection by human operators. NASA has launched heliospheric imager (HI) on board STEREO to study CMEs in the heliosphere. However, due to low signal-to-noise and bright star-lights, an automated algorithm to detect CMEs in heliosphere could not have been designed. The occurrence of CMEs is found to be correlated with the sunspot cycle. Solar cycle 24 gained special interest because it produced weak heliospheric field. It was proposed that weak heliospheric field cause weak CMEs to escape the Sun and thus the total number of CMEs in solar cycle 24 are more than cycle 23. Later, it was reported that the increase in the occurrences of CMEs was due to human subjectivity and when the automated catalogs were used then it was found that solar cycle 24 was producing fewer CMEs than cycle 23 (Wang and Colaninno 2014). A few recent studies have revealed that the CMEs per sunspot has indeed increased in solar cycle 24 (Petrie 2015). It is not yet precisely known whether or not solar cycle 24 is producing more CMEs than cycle 23 because the visual inspection of CMEs suffers from human subjectivity and automated methods have their own limitations in terms of thresholds and thus may miss several weak CMEs or can detect false events. Furthermore, it was reported that solar cycle 24 produced more halo CMEs than solar cycle 23 due to the weak heliospheric field in solar cycle 24, which allowed narrow CMEs to expand anomalously to become halos. However, these halo CMEs produced weak geomagnetic storms because the magnetic field strength inside them got diluted due to the anomalous expansion. These studies show the importance of studying solar cycle variations of CMEs because it may help us in predicting the space weather for a given solar cycle.

Motivated by these studies, I attempted to study the properties of few small and large scale transients combining multi-wavelength observations using space-based

instruments hoping to address some of the long standing problems. I used co-ordinated observations from IRIS, AIA and HMI to explore the nature and the sources of PDs in an on-disk plume (Pant *et al.* 2015). The interaction between a coronal jet and a coronal loop was studied. It was found that a jet excited the transverse oscillations in the coronal loop. The energy stored in the jet was estimated and compared with the energy density of the oscillating loops (Sarkar *et al.* 2016). I studied the interaction between blast waves and fan loops and proposed a different excitation mechanism for exciting standing slow waves in coronal fan loops (Pant *et al.* 2017). An automated algorithm was designed to detect CMEs in the heliosphere using the data from inner heliospheric imager (HI-1) on board STEREO (Pant *et al.* 2016b). It is now running on real–time at Solar Influences Data Analysis Centre (SIDC), Royal Observatory of Belgium (ROB). Finally, I studied the kinematics of fast and slow CMEs separately in solar cycles 23 and 24 and conjectured that they have different energy sources (Pant et al, 2017 under review).

1.5 Outline of the Thesis

This thesis is the compilation of the studies of different small and large scale transients in the solar atmosphere using high-resolution space-based imaging and spectroscopic instruments. The interactions between different transients and the effects of large scale transients on space weather are studied. A summary of each chapter of the thesis is outlined here.

In chapter 1, an overview of the overall structure of the Sun and a brief history of the observations of the solar transients is already presented. The motivation for the current study and its relevance in the context of the solar physics is also

discussed.

In chapter 2, I describe space-based instruments and the catalogs, which are used to perform studies presented in this thesis. To understand the dynamics of the chromosphere and most importantly the transition region, we used IRIS. Its high-resolution imaging and spectroscopic capabilities led us to study the properties of transients like TR jets, which are primarily seen in the transition region network boundaries. Data from AIA on board SDO and EUVI on board STEREO cover a broad range of temperatures and are used to study small scale transients in the corona. HI-1 on STEREO and LASCO based CME catalogs are used to study large scale coronal transients, primarily CMEs and Co-rotating Interaction regions (CIRs). A brief description of the above instruments is presented in this chapter.

The role of small scale transients in the evolution of a solar coronal plume is examined in chapter 3. The dynamics of a plume footpoints seen in the vicinity of a coronal hole is studied using the imaging data from the AIA, Helioseismic and Magnetic Imager (HMI) on board the SDO, and spectroscopic data from the IRIS. Quasi-periodic brightenings that are associated with underlying magnetic flux changes are observed at the base of the plume. With the high spectral and spatial resolution of IRIS, we identify the sources of these brightenings. Enhanced line width, intensity and a large deviation from the average Doppler shift in the line profiles at specific instances are found, which indicates the presence of flows (jet-like features) at the footpoint of the plume. These jet-like features are also responsible for the generation of intensity disturbances which propagate along the plume to larger distances as recorded from multiple AIA channels. Thus, the interaction between small scale transients and intensity disturbances in the plume is presented in this chapter.

Chapter 4 presents a unique case of transverse oscillations in a coronal loop triggered by a coronal transient, jet. Observations are made using SDO/AIA and

STEREO/EUVI. The jet is believed to trigger transverse oscillations in the coronal loop. The jet originated from a region close to the coronal loop. Only one complete oscillation is detected with an average period of ∼32±5 minutes. Using magnetohydrodynamic (MHD) seismologic inversion techniques, the magnetic field inside the coronal loop is estimated between 2.68–4.5 G. The velocities of the hot and cool components of the jet were estimated to be 168 km s^{-1} and 43 km s^{-1}, respectively. The energy density of the jet is found to be greater than the energy density of the oscillating coronal loop, therefore it is concluded that the jet has excited transverse oscillations in the coronal loop. This is the first coronal loop seismology study using the properties of a jet propagation to trigger oscillations. In this work, we report the interaction between two different coronal transients, *i.e.*, a coronal jet and transverse oscillations in the coronal loop.

In chapter 5, we report the intensity oscillations in magnetic structures like fan loops seen in AIA 171 and 193 Å. These intensity oscillations are triggered by the interaction of blast wave with the fan loops. Blast waves mostly excite transverse oscillations in the coronal loops. In this work, we report longitudinal oscillations in fan loops triggered by blast waves generated at a distant active region. The blast wave compressed the fan loop and thus perturbed the density inside it. These perturbations then propagated along the loop and got reflected from the other footpoint. The amplitude of oscillations changes from one footpoint to another, which led us to believe that these oscillations are the signatures of standing slow wave. The observations match well with the simulations carried out by Yuan *et al.* (2015) using forward modelling of hot and flaring coronal loops. To best of our knowledge, this is the first report of the existence of the standing oscillations in the fan loops.

The first successful automated detection of coronal mass ejections (CMEs) in the heliosphere is presented in chapter 6 using the data from the inner heliospheric imager (HI-1) cameras on the STEREO-A spacecraft. Detection of CMEs is done

in time–height maps based on the application of the Hough transform, using a modified version of the Computer Aided CME Tracking (CACTus) software package, conventionally applied to coronagraph data. In this chapter, the method of detection is discussed in detail. The results of the application of the technique to a few CMEs, which are well detected in the HI-1 imagery are presented and these results are compared with those based on manual-cataloging methodologies. The advantages and disadvantages of this method are also outlined.

Chapter 7 is devoted to a statistical study of the kinematics of slow and fast CMEs in solar cycles 23 and 24. The distribution of the width of slow and fast CMEs using Coordinated Data Analysis Workshops (CDAW) and Computer Aided CME Tracking (CACTus) catalogs is investigated. We note that the width distribution of slow and fast CMEs have different power laws. The width distribution by isolating the limb CMEs extracted from CDAW catalog is also studied and it is found that results are similar to non-limb CMEs. The variation of occurrences of CMEs with solar cycles 23 and 24 is studied. While the occurrence rate of fast CMEs is well correlated with the sunspot numbers, slow CMEs did not follow this trend, at least in cycle 23. We also found that solar cycle 24 produces many more slow and poor CMEs as compared to fast CMEs in cycle 24 and slow CMEs in cycle 23 which may be due to the weak polar and heliospheric field in solar cycle 24. This chapter presents the kinematics of large scale coronal transients over a time period of two solar cycles and its possible relation to space weather.

Chapter 8 summarises the entire thesis work. Main conclusions drawn from different studies are outlined here and possible future prospects are also listed.

Chapter 2

Instruments

The Sun is very well observed from ground and space-based telescopes. Because of its proximity to Earth, it is possible to spatially resolve the features in the atmosphere of the Sun. In spite of this, there are several limitations in the solar observations. For example, X-ray and extreme ultraviolet observations cannot be made using ground-based instruments because X-ray and ultraviolet radiation are mostly blocked by the Earth's atmosphere. Therefore, the observations in these wavelengths are made using space-based telescopes. But space-based instruments are limited by the size of the telescopes and thus unlike ground-based instruments, they can not make observations in high resolutions. However, one advantage of using space-based observations is that it is free from atmospheric extinction, seeing and turbulence. The solar corona is hot ($> 10^6$ K) and tenuous. Therefore, it emits radiation in X-ray and Extreme Ultraviolet (EUV) part of the electromagnetic spectrum. The solar corona is also observed in visible wavelengths because electrons in solar corona scatter the photospheric light.

To study the coronal transients at different spatial and temporal scales, multi-wavelength studies were performed in this thesis using different space-based instruments. In this chapter, I will describe briefly the instruments and the catalogs that were used to perform these studies.

2.1 Solar Dynamics Observatory

Solar Dynamics Observatory (SDO) was launched on February 11, 2010, under NASA's Living With a Star (LWS) program (Pesnell *et al.* 2012). It observes the Sun near simultaneously in different EUV emission lines. It also measures line of sight (LOS) and vector magnetic field at the photosphere of the Sun. One of the main science objectives of SDO is to perform high-resolution multi-wavelength observations of the Sun to understand the dynamic processes in the chromosphere and corona and their relation to the magnetic field at the photosphere. SDO consists of three instruments (see Figure 2.1)

- Atmospheric Imaging Assembly (AIA; Lemen *et al.* 2012a)
- Extreme Ultraviolet Variability Experiment (EVE; Woods *et al.* 2012)
- Helioseismic and Magnetic Imager (HMI; Schou *et al.* 2012)

I have primarily used AIA and HMI for the studies presented in this thesis.

2.1.1 AIA

AIA was built in collaboration with Lockheed Martin Solar Astrophysics Laboratory (LMSAL), California. AIA comprises an array of four telescopes (see

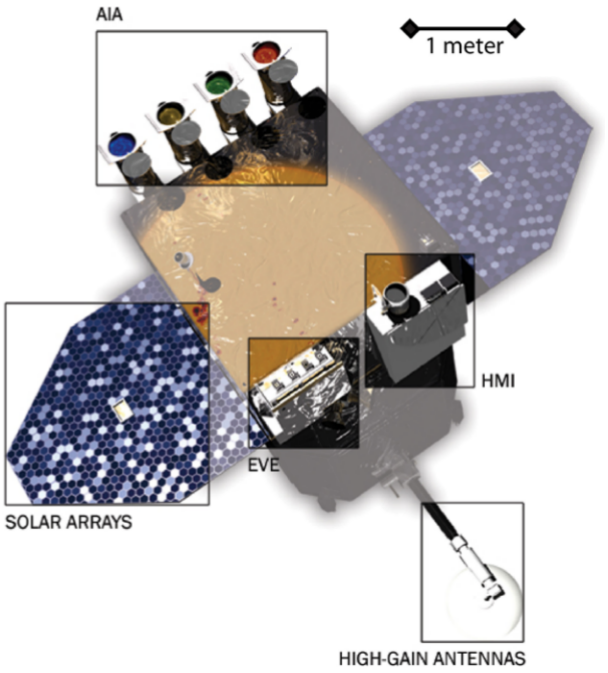

FIGURE 2.1: The SDO spacecraft with locations of AIA, HMI and EVE highlighted. *Credit*: Pesnell *et al.* (2012)

Figure 2.2) that obtain the narrow-band images of the Sun in seven EUV and three UV-visible wavelengths. Observing solar atmosphere in ten different passbands allows AIA to cover the full thermal range of the solar atmosphere (6×10^4 K – 2×10^7 K). AIA uses CCDs having a pixel size of 12 μm and each CCD has 4096×4096 pixels. AIA operates in full-disk synoptic mode and take UV or visible-light image every 12 s. However, small regions of interest in solar atmosphere can also be observed with the cadence of 2 s. The longest exposure time that can be obtained with 12 s cadence, is 2.9 s. AIA takes high-resolution images of solar atmosphere with a pixel resolution of $0.6''$ pixel^{-1}.

2.1.2 HMI

HMI was also built by LMSAL, California in collaboration with Stanford University. It maps the velocity and magnetic fields at the photosphere using Fe I

absorption line at 6173 Å. HMI measures Stokes parameters using Zeeman effect to create LOS magnetic field map and vector magnetic field map (vector magnetogram) over the full disk of the Sun with a cadence of 45 s and spatial resolution of 0.5″ pixel^{-1}.

HMI also measures Doppler shifts at the photosphere to construct the full-disk Dopplergram with cadence and spatial resolution similar to the vector magnetogram.

FIGURE 2.2: The array of four AIA telescopes mounted on the SDO spacecraft. *Credit*: Lemen *et al.* (2012a)

2.1.3 EVE

EVE was built by Laboratory for Atmospheric and Space Physics (LASP), University of Colorado. EVE is designed to measure the solar spectral irradiance in ultraviolet part of the solar spectrum, *i.e,* 0.1–105 nm and at 121.6 nm (Lyman-α). EVE continuously monitors the solar spectral irradiance in the ultraviolet at a cadence of 10 s.

2.2 Solar Terrestrial Relations Observatory

Solar TErrestrial RElations Observatory (STEREO) was launched on October 25, 2006. It employs two space-based observatories one ahead (STEREO-A) and one behind (STEREO-B) of Earth in its orbit (Driesman *et al.* 2008). STEREO provides first-ever stereoscopic view of Sun and heliosphere from out-of-Earth orbit vantage points. The main objective of the STEREO mission is to improve our understanding of the three-dimensional nature of the solar corona. Each of the two STEREO spacecraft comprises the following four instrument packages (see Figure 2.3):

- Sun Earth Connection Coronal and Heliospheric Investigation (SECCHI; Kaiser 2005; Howard *et al.* 2008)
- STEREO/WAVES (SWAVES; Bougeret *et al.* 2008)
- In-situ Measurements of Particles and CME Transients (IMPACT; Luhmann *et al.* 2008)
- Plasma and Suprathermal Ion Composition (PLASTIC; Galvin *et al.* 2008)

2.2.1 SECCHI

The SECCHI instrument on each STEREO spacecraft is a suite of five telescopes that image the solar corona and the heliosphere from solar disk to 1 AU and beyond. SECCHI on each STEREO spacecraft comprises an extreme ultraviolet imager (EUVI), two coronagraphs (COR1 and COR2) and two heliospheric imagers (HI-1 and HI-2) as shown in Figure 2.3 (b). All telescopes use backside illuminated CCDs with 2048×2048 pixels.

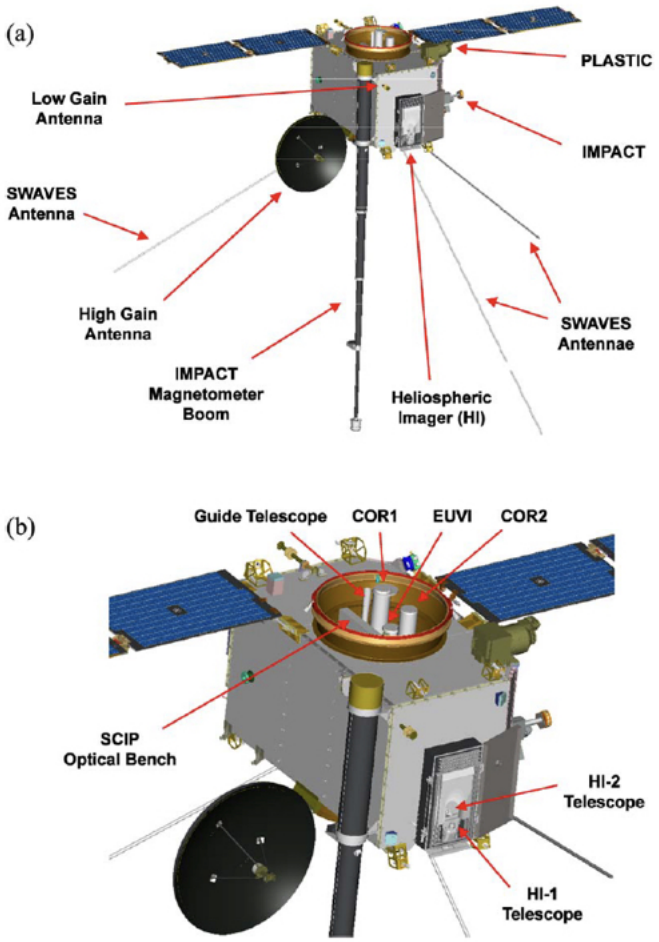

FIGURE 2.3: (a): An artist's drawing of STEREO-B spacecraft with the locations of different instruments. (b): A close–up view of SECCHI. *Credit*: Eyles *et al.* (2009)

2.2.1.1 EUVI

The EUVI observes the chromosphere and corona in four different EUV emission lines *i.e,* 304 Å, 171 Å, 195 Å, and 284 Å. It obtains the full-disk image of the Sun with a spatial resolution of 1.6″ pixel^{-1} at a nominal cadence of 20 minutes in the synoptic mode. EUVI has a field-of-view (FOV) of ± 1.7 $R_{\odot}$.

2.2.1.2 Inner coronagraph (COR1) and outer coronagraph (COR2)

A coronagraph is an instrument that artificially blocks the solar disk in order to observe the solar corona whose brightness is typically million times fainter than the brightness of the solar–disk. COR1 and COR2 on board STEREO are designed to obtain the unvignetted view of the solar corona from 1.4–4 $R_{\odot}$ and 2.5–15 $R_{\odot}$, respectively. Unlike COR1 which is an internally occulted coronagraph, COR2 is externally occulted. The COR1 and COR2 obtain polarized brightness (pB) images of solar corona (it greatly reduces the contribution of the stray light) at 633–658 nm and 650–750 nm bandpass with the spatial resolution of 4.17″ pixel^{-1} and 15″ pixel^{-1}, respectively. The images of solar corona are taken with the variable cadence that can range from 5–20 minutes.

2.2.1.3 Heliospheric Imager

Heliospheric Imager consists of two wide–angle telescopes (HI-1 and HI-2) that extend the imaging capabilities of the COR1 and COR2 to 1 AU and beyond (Eyles *et al.* 2009). The main objective of HI is to track CMEs in the heliosphere and to predict their arrival times on Earth. The angular FOVs of HI-1 and HI-2 are 20° and 70°, with the FOVs centered at 14° and 54° elongations, respectively. HI-1 and HI-2 effectively image the heliosphere with spatial resolutions of 70″ and 240″ pixel^{-1} at the cadence of 40 minutes and 120 minutes, respectively during nominal spacecraft operations. The pixels on the CCD detector of HI are binned 2×2 onboard to generate the science images. The schematic layout of the HI is shown in Figure 2.4 (b)

SWAVES measures the interplanetary type II and type III radio bursts to understand the propagation of CMEs and CME-driven shocks. IMPACT maps the three-dimensional distribution of solar wind plasma, solar energetic particles and

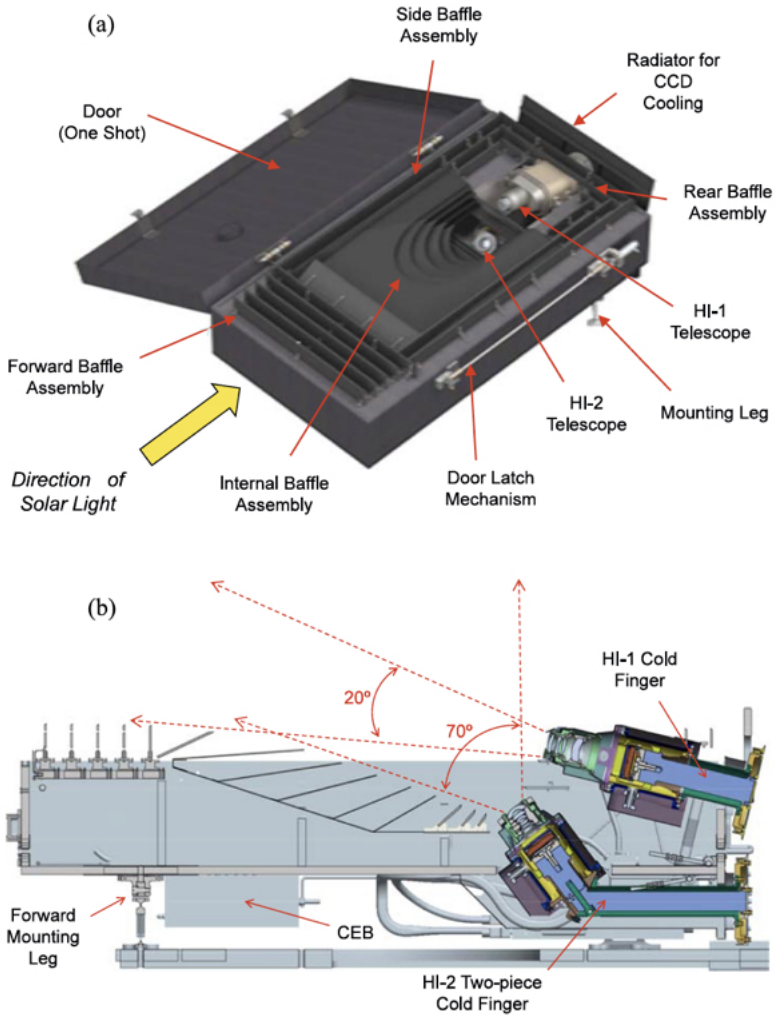

FIGURE 2.4: (a): Design concept of heliospheric Imager with two telescopes HI-1 and HI-2 mounted on it. (b): The side–view through the HI instrument highlighting the FOVs of two telescopes. *Credit*: Eyles *et al.* (2009)

local vector magnetic field and PLASTIC measures kinetic properties and composition of solar wind and suprathermal particles.

2.3 Interface Region Imaging Spectrograph

Interface Region Imaging Spectrograph (IRIS) was launched on June 27, 2013, using a Pegasus-XL rocket. IRIS is a small explorer spacecraft that obtains high

resolution UV spectra and images simultaneously over a FOV of up to 175″× 175″ for slit-jaw images (SJIs) and up to 130″× 175″ for the spectrograph. A schematic design concept of IRIS is shown in Figure 2.5. IRIS obtains the spectra in three spectral windows, one in near UV (NUV; 2782.7–2835.1 Å) and two in far UV (FUV1; 1331.7–1358.4 Å and FUV2; 1389–1407 Å) with spectral resolution of ∼12.98 mÅ pixel^{-1} in FUV1 and FUV2 spectral windows and 25.46 mÅ pixel^{-1} in NUV spectral window. These three spectral windows effectively cover the temperature range from $10^{3.7}$–10^{7} K. Some of the brightest emission lines in spectral windows are C II 1335Å, Si IV 1394Å, Si IV 1403Å, Mg II k 2796Å and Mg II h 2803Å. In addition to spectra, IRIS also obtains SJIs in six different broadband filters; four of which are used for solar observations. IRIS has an effective spatial resolution of 0.16″ pixel^{-1} in SJIs and cadence up to ∼3 s in SG. High spatial and temporal resolution of IRIS together with simultaneous spectral and imaging capabilities make it suitable for the study of small scale transients in the solar atmosphere.

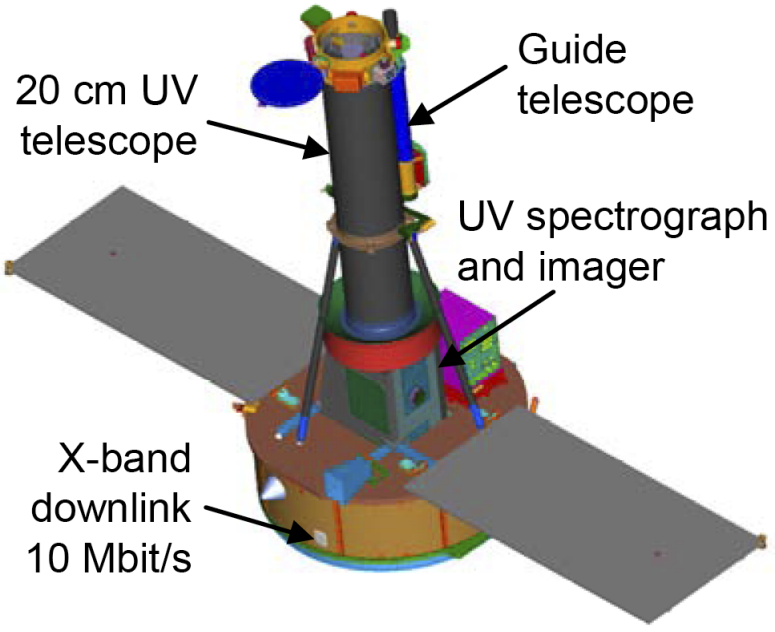

FIGURE 2.5: The schematic view of IRIS. *Credit*: De Pontieu *et al.* (2014)

2.4 Coronal Mass Ejections Catalogs

The type and properties of CMEs are listed in different e-catalogs. I have used manual and automated catalogs of coronal mass ejections (CMEs) to study their dynamics over solar cycles 23 and 24. In this section, I will briefly describe Coordinated Data Analysis Workshops (CDAW), Computer Aided CME Tracking (CACTus) and Heliospheric Cataloging Analysis and Techniques Service (HELCATS) catalogs.

2.4.1 CDAW catalog[1]

CDAW catalog is maintained at Goddard Space Flight Center and is supported by NASA's LWS program and the SOHO project. CDAW catalog is created by visual inspection of CMEs in Large Angle and Spectrometric Coronagraph (LASCO) C2/C3 images (Yashiro *et al.* 2004). A CME is defined as an enhancement in the brightness moving outward in at least two consecutive LASCO images. CDAW catalog lists the time at which the CME first appear in LASCO/C2 coronagraph FOV. The height of CME in every image is calculated at the position angle where the leading edge of a CME moves fastest. The height–time map is, then, used to estimate the linear velocity, second-order velocity and acceleration of a CME. CDAW catalog also lists the position angle (measured as counter-clockwise from solar north) and width of a CME in degrees. All the parameters listed in the CDAW catalog are projected in the plane of sky (POS). CDAW catalog also categorise a CME into "very poor" and "poor" CMEs based on the intensity of a CME in coronagraph FOV. Thus manual catalogs are subjected to human judgements especially for "very poor" and narrow CMEs. Each CME in the catalog is also characterised by a mass and a kinetic energy.

[1] `https://cdaw.gsfc.nasa.gov/CME_list/`

2.4.2 CACTus catalog[2]

CACTus is run and maintained at Solar Influences Data Analysis Center (SIDC), Royal Observatory of Belgium (ROB), Belgium. It detects CMEs automatically in LASCO/C2 and C3 and SECCHI/COR2 images without any human intervention (Robbrecht and Berghmans 2004). It has two main modules for detecting CMEs. The first module is the image processing module that removes the noise and enhances signal-to-noise in coronagraph images. The second module is the image recognition module that detects a CME based on several defined parameters. CACTus produces output similar to CDAW catalog. However, its methodology of making those measurements is quite different. CACTus works on the principle of Hough transform that detects straight lines in noisy data. Therefore, CACTus lists only linear velocity of a CME. CACTus also lists the position angle and the width of a CME. In contrast to the CDAW catalog, CMEs detection by CACTus is faster and more objective.

2.4.3 HELCATS catalog[3]

HELCATS WP2[4] catalog is produced from visual inspection of CMEs in STEREO/HI images. It lists the time of appearance, northernmost and southernmost principal angle extent. HELCATS WP3[5] catalog estimates the three-dimensional speed of a CME using three different geometrical models: Fixed-ϕ fitting, Self-Similar Fitting and Harmonic mean fitting. HELCATS manual catalog does not consider any brightness change of angular width less than 20° as a CME. It categorises a CME into "good", "fair", and "poor" which indicates a confidence with which an event can by definition be considered as a CME.

[2] `http://sidc.oma.be/cactus/catalog.php`
[3] `https://www.helcats-fp7.eu`
[4] `http://www.helcats-fp7.eu/catalogues/wp2_cat.html`
[5] `http://www.helcats-fp7.eu/catalogues/wp3_cat.html`

TABLE 2.1: Instruments and catalogs used to study transients

Instrument/catalog	Spatial resolution (arcsec pixel^{-1})	Cadence (s)	Type of transient
IRIS SJI/SG	0.166	5-12	Transition region Jets
AIA	0.6	12	coronal jets and waves in coronal loops
EUVI	1.6	300–1200	coronal jets and loops
HI-1/HELCATS	70	2400	CMEs in heliosphere
CDAW/CACTus	–	–	CMEs

I have used several space-based instruments, automated and manual catalogs to study the dynamics of the coronal transients at different spatial and temporal scales. Table 2.1 summarises the instruments used to study different types of transients.

Chapter 3

Dynamics of coronal plume as seen from Interface Region Imaging Spectrograph, Atmospheric Imaging Assembly and the Helioseismic and Magnetic Imager[†]

[†]Results of this work are published in Pant *et al.* (2015)

All the animations that are referred to in this chapter are available at `http://dx.doi.org/10.1088/0004-637X/807/1/71`

3.1 Introduction

Coronal plumes, extending as bright narrow structures from the solar chromosphere into the high corona are mostly rooted in coronal holes (CHs) or their neighbourhood (van de Hulst 1950; Saito 1958, 1965; DeForest *et al.* 2001). They are plasma density enhancements in the low and extended corona aligned along the magnetic field (Velli *et al.* 2011; Wilhelm *et al.* 2011). Plume footpoints are typically $4''$ wide and plumes expand rapidly with height (Deforest *et al.* 1997). Raouafi *et al.* (2006, 2007) showed that plumes are more than five times denser than the interplume regions at the base of the corona. Multi-wavelength UV–EUV imaging and spectral observations from the Solar and Heliospheric Observatory (SOHO), the Solar TErrestrial RElations Observatory (STEREO) and the Solar Dynamics Observatory (SDO) allowed us to study the formation and evolution of plumes (see review by Wilhelm *et al.* 2011). Plumes are difficult to observe in low-latitude CHs because of the bright foreground and background emission (Wang and Muglach 2008). The low-latitude plumes appear to be similar to their polar counterparts (Tian *et al.* 2011c). Saito and Tanaka (1957) first pointed out the association of polar plumes with magnetic flux concentrations. It was also revealed by many studies that polar plumes arise from unipolar magnetic regions associated with the supergranular network boundaries (Harvey 1965; Newkirk and Harvey 1968; Fisher and Guhathakurta 1995; Deforest *et al.* 1997; DeForest *et al.* 2001; Young *et al.* 1999). Coronal plumes can be formed due to magnetic reconnection of newly emerging magnetic flux with the pre-existing dominant unipolar fields (Grappin *et al.* 2011), which can further lead to localized heating (Wang and Sheeley 1995). Raouafi *et al.* (2008) and Raouafi and Stenborg (2014) discovered that coronal jets are the precursors of plumes.

Ofman *et al.* (1997) reported quasi-periodic variations in polar CHs and conjectured compressive waves to be responsible for them. Quasi-periodic brightness

variations in plumes have been observed with Extreme ultraviolet Imaging Telescope (EIT) by Deforest and Gurman (1998). They found the presence of propagating disturbances (PDs) in several plumes with periods between 10 and 15 minutes and speeds between 75 and 150 km s^{-1} in the height range from 0.01 $R_\odot$ to 0.2 $R_\odot$. They conjectured such PDs to be the compressive waves. A number of studies followed, reporting such oscillations in plumes, interplumes, and CHs, using spectroscopic data obtained with the Coronal Diagnostic Spectrometer (CDS) and Solar Ultraviolet Measurements of Emitted Radiation (SUMER) on board SOHO and the Extreme ultraviolet Imaging Spectrometer (EIS) on board Hinode (Banerjee *et al.* 2001, 2000; O'Shea *et al.* 2006; Banerjee *et al.* 2009; Gupta *et al.* 2009). Using extreme ultraviolet (EUV) observations from STEREO, McIntosh *et al.* (2010) analyzed several plume structures and suggested that PDs along polar plumes could be due to the collimated high-speed plasma jets that have similar properties to slow magnetoacoustic waves. Further, they conjectured that these jets could be responsible for loading a significant amount of heated plasma into the fast solar wind. Indeed, recent high-resolution observations have revealed jet-like flows at the bases of plumes (Raouafi and Stenborg 2014) and at the network boundaries in CHs (Tian *et al.* 2014). The plume formation and dynamics are still a matter of debate related to the broader issue of wave propagation, plasma jets, and their role in the acceleration of the fast solar wind.

To understand the nature of the source regions of plumes and the PDs, we study the footpoints of an on-disk plume adjacent to a CH as seen in the Atmospheric Imaging Assembly (AIA) EUV coronal images (Lemen *et al.* 2012a) and in the Helioseismic and Magnetic Imager (HMI) magnetogram (Schou *et al.* 2012) on the SDO and simultaneously with the Interface Region Imaging Spectrograph (IRIS; De Pontieu *et al.* 2014). Combining imaging and spectroscopic observations, we focus on the dynamics of this plume. We show that the jet-like features (termed as "jetlets") load mass to the plumes and can also be responsible for the generation of the PDs as observed at greater heights.

3.2 Data analysis and Results

3.2.1 Observation and Data Reduction

Observational data were obtained from IRIS, AIA, and HMI instruments from 16:26 UT to 17:51 UT on July 12, 2014. We used AIA passbands at 193, 171, and 1600 Å and HMI line of sight (LOS) magnetograms. We used standard AIA prep routines to produce level 1.5 images. IRIS data were taken in sit-and-stare mode with the slit centered at $239'', -559''$ pointing adjacent to a coronal hole. This dataset has three spectral lines, namely C II 1335.71 Å, Si IV 1402.77 Å, and Mg II k 2796 Å. We used Si IV 1402.77 Å for this study. Slit-jaw images (SJIs) were available only with the 1330 Å filter. We used IRIS Level 2 processed data which are corrected for dark current, flat field and geometrical corrections etc. The cadence of 1330 Å SJIs and spectra was ∼5 s with a pixel size of $0.166''$. AIA and HMI images were de-rotated before AIA 1600 Å images were co-aligned with IRIS SJIs 1330 Å using cross-correlation. Figure 3.1 shows the plume as seen in various AIA channels, IRIS 1330 Å SJI, and HMI LOS magnetogram. The magnetogram (Figure 3.1 (b)) shows that the plume is dominated by negative-polarity magnetic field marked with red contours (-50 G). We made an animation (associated with Figure 3.1 and available online) with HMI LOS magnetogram images; it shows the evolution of negative and positive flux with time. In the animation, red and green contours represent the magnetic field strengths of -50 G and 20 G respectively.

Figure 3.1 clearly shows that the IRIS slit is crossing the footpoints of the plume. We extrapolate the coronal magnetic field with a potential field approximation, using the LOS magnetic field observed by HMI as the boundary condition at the photosphere (Figure 3.2). We select a large field of view (FOV) around this plume structure to approximately satisfy the flux balance condition. This FOV magnetogram is projected to disk center correcting for the difference between

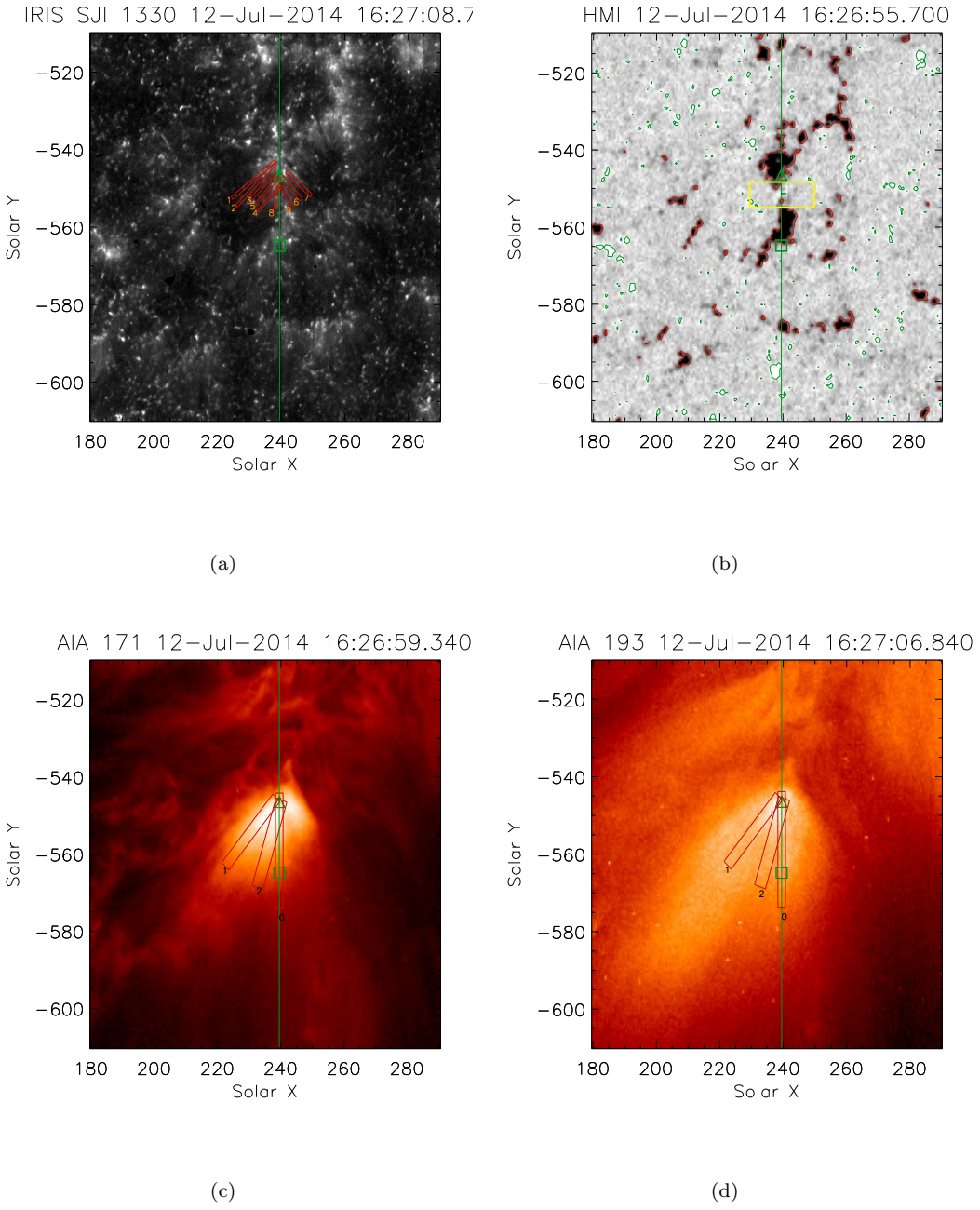

FIGURE 3.1: (a) IRIS 1330 Å SJI represents our region of interest (ROI), covering an on-disk plume adjacent to a coronal hole. Nine artificial slices are placed for further analysis. (b) HMI LOS magnetogram. The yellow box represents the region used for calculating the positive flux (see Figure 3.5). (c) AIA/SDO 171 Å image overplotted with three artificial slices used to create time–distance maps (see Figure 3.6). (d) Same as (c) for AIA/SDO 193 Å. The vertical green line on each image represents the position of the IRIS slit. The green triangle is the location where we study the variation of different parameters of the Si IV 1402.77 Å line (see Figure 3.5). The green triangle and square symbols represent the 'Y' positions along the IRIS slit used to analyze spectra (see Figure 3.4).
(An animation of this figure is available.)

normal and LOS values, and we compute the potential field in a 3D box (Gary 1989) encompassing the plume structure.

We trace field lines having footpoints in strong magnetic patches ($|B_z| > 25$ G). In Figures 3.2 (a) and (b), they are overlaid on the boundary magnetogram along with contours ($\pm$ 25 G). Most of the field lines from the magnetic regions are open (yellow). The shapes of the two major open-field structures associated with the strong negative magnetic patches are consistent with the funnel structure of the plume originating from the network boundary, as revealed from the AIA images (Figure 3.1 (c) and (d)). However, only the northernmost structure appears bright in the AIA images at the time of the observations. Note that the difference in the orientation is due to projection, which is corrected in this model. It is also noted that the plume originates from the network boundary, as revealed from IRIS SJIs (Figure 3.1 (a)).

Apart from these open field lines, low-lying field lines (blue) connect the weak field regions in the immediate neighbourhood of the main plume structure. The animation of Figure 3.1 shows the continuous emergence of positive flux followed by flux cancellation. Reconciling the model of Shibata *et al.* (1994), the open-dipped field lines at the edges of the plume, in a dynamical scenario, facilitate continuous reconnection with the neighbouring closed field lines to supply heat and energy for sustaining the plume.

3.2.2 Spectroscopic analysis

We have focused on the dynamics of two footpoints (negative polarity) as marked by a triangle and square (at 'Y' positions -546″ and -564″ respectively) in Figure 3.1. We study the time evolution of this small region as seen in IRIS Si IV

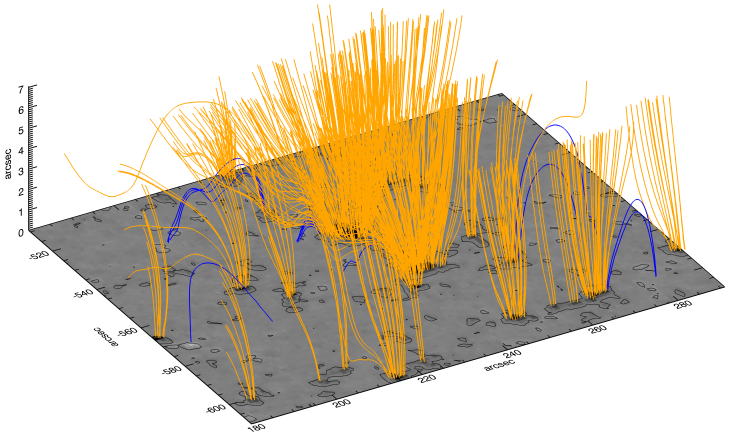

(a)

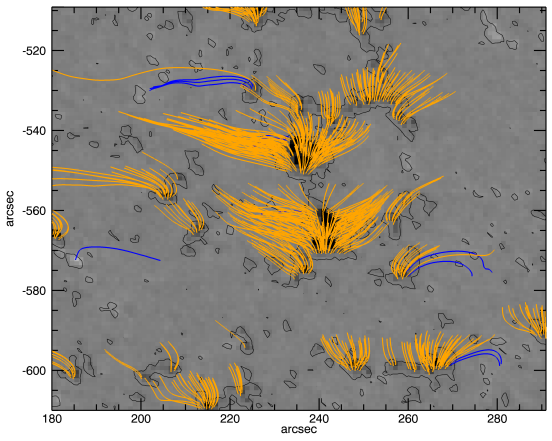

(b)

FIGURE 3.2: (a) 3D view of extrapolated field lines. (b) 2D view of extrapolated field lines.

1402.77 Å spectral profiles. At first, a single Gaussian fit is performed on the weighted averaged (three pixels along the slit and three in time) spectral profile. We average the spectral profiles to increase the signal-to-noise ratio, using error bars as calculated by *iris_pixel_error.pro* as weights. From the single Gaussian fit, we derive peak intensity, Doppler shift, line width, and asymmetry coefficient (see Figure 3.3). We use the median of the centroid of the fitted Gaussians as the rest wavelength to estimate the Doppler velocity. We did not take the mean value of a

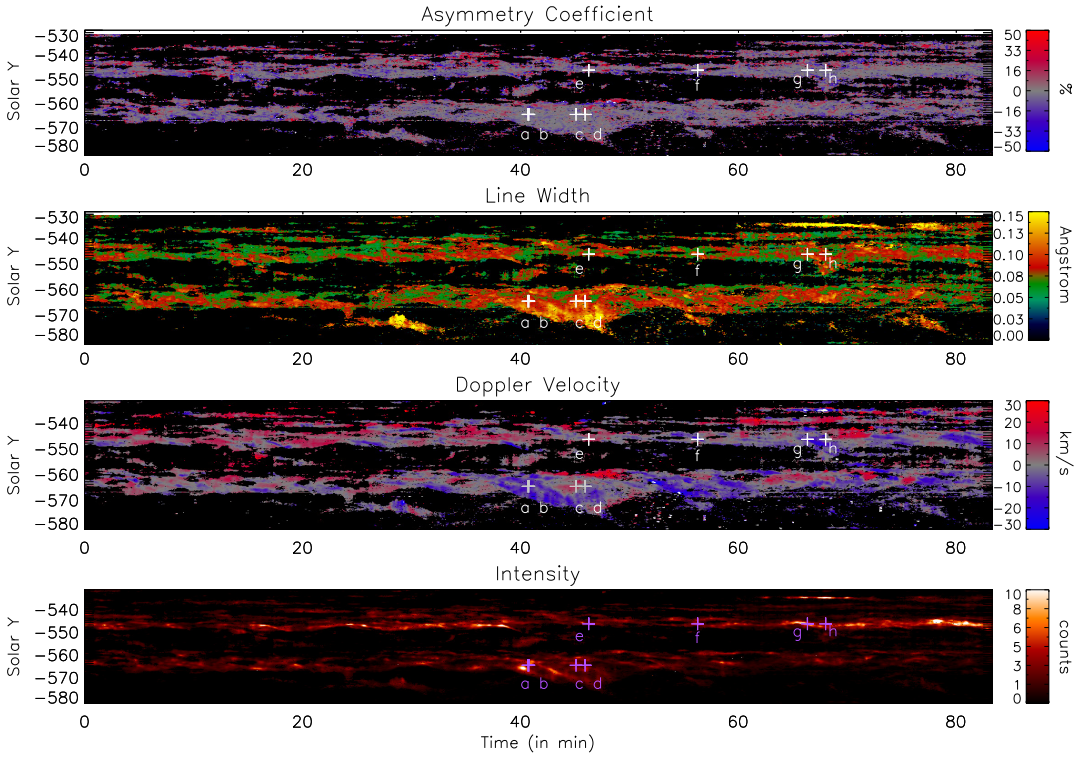

FIGURE 3.3: Time evolution of peak intensity, Doppler velocity, line width, and asymmetry coefficient as derived from single Gaussian fitting over Si IV 1402.77 Å spectra. Positions marked as (a)–(h) are used to show individual spectral profiles (see Figure 3.4).
(An animation of this figure is available.)

quiet region because the quiet region does not have enough signal to perform a reliable Gaussian fitting. The evolution of the spectral profile at these two positions as a function of time is shown in the animation of Figure 3.3 (available online). In this animation, IRIS 1330 Å SJIs are also included to show the jet-like features at network boundaries. To analyze the non-Gaussian aspect of the spectral profiles, we use the coefficient of asymmetry defined in Dolla and Zhukov (2011). However, contrary to what was done in that reference, we do not normalize by the error bars of spectral intensities, because we are interested here in quantifying the asymmetry and not in assessing its statistical significance. The coefficient of asymmetry therefore provides the percentage of area in the profile that deviates from the fitted single Gaussian, according to the pattern defined by the following formula:

$$A = \frac{1}{I_0} \sum_k \epsilon(\lambda) \cdot \mathrm{sgn}(\Delta_k(\lambda)) \cdot \Delta_k(\lambda), \tag{3.1}$$

where λ is the wavelength, I_0 is the total intensity in the spectral line and $\Delta(\lambda) = s_k(\lambda) - f_k(\lambda)$ is the difference between the spectrum $s_k(\lambda)$ and the fitted Gaussian $f_k(\lambda)$, which are discretized on bin k. The contribution factor $\epsilon(\lambda)$ is defined as follows:

$$\epsilon(\lambda) = \begin{cases} -1 & \text{if } \lambda \in [\lambda_0 - 2\,\sigma; \lambda_0 - \sigma) \\ 1 & \text{if } \lambda \in [\lambda_0 - \sigma; \lambda_0) \\ -1 & \text{if } \lambda \in (\lambda_0; \lambda_0 + \sigma] \\ 1 & \text{if } \lambda \in (\lambda_0 + \sigma; \lambda_0 + 2\,\sigma] \\ 0 & \text{otherwise,} \end{cases} \tag{3.2}$$

where λ_0 is the center and σ the half-width at $1/\sqrt{e}$ of the fitted Gaussian. The sign of the coefficient of asymmetry indicates in which wing of the profile most imbalance is present (negative and positive on the blue and red wings, respectively). Another method of quantifying the profile asymmetry is the red–blue (RB) asymmetry method. The RB technique has been widely used in both optically thick (e.g., in Hα, Madjarska *et al.* 2009; Huang *et al.* 2014) and optically thin (e.g., De Pontieu *et al.* 2009; Tian *et al.* 2011b) spectral-line analysis.

Figure 3.4 shows spectral profiles at different instances (as marked in Figure 3.3) along the slit. We find that the spectral profiles are significantly non-Gaussian with two or more components present. We fit the spectral profiles at these instances with a single Gaussian (shown in orange) and double Gaussian (in green). Spectra averaged during the first 20 minutes of observations at the same 'Y' positions are shown in blue. Both components of the double Gaussian are shown in gray. We observe both blueward and redward asymmetries at different instances (see Figure 3.4). The large asymmetry and double Gaussian behaviour of the spectral profile indicates the presence of flows at these instances. Such behaviour can also

be attributed to waves (Verwichte *et al.* 2010b) but we can discard this interpretation in our observations because the associated fluctuations in intensity are too large to correspond to linear waves only (see Figure 3.5). Non-Gaussian behaviour is present on several occasions during the time of observation of IRIS at the positions marked by the triangle and square in Figure 3.1 (see animation of Figure 3.3). IRIS 1330 Å SJIs show the presence of several small-scale jets throughout the time of observation at these two positions. Reconnection jets cause enhancements at the line wings, which lead to large asymmetries, larger line width, greater intensity and large Doppler shift. The red shift in spectra could be a projection effect as the plume is close to the south pole. Besides this the redshifts may indeed imply that at least part of the material is falling back. This is consistent with Figure 3.5 where the brightenings are associated with strong blueshifts, with progressive evolution not only toward zero but also redshifts (i.e velocities slightly positive). There is probably a combination of both blueshifts and redshifts during this recovery phase.

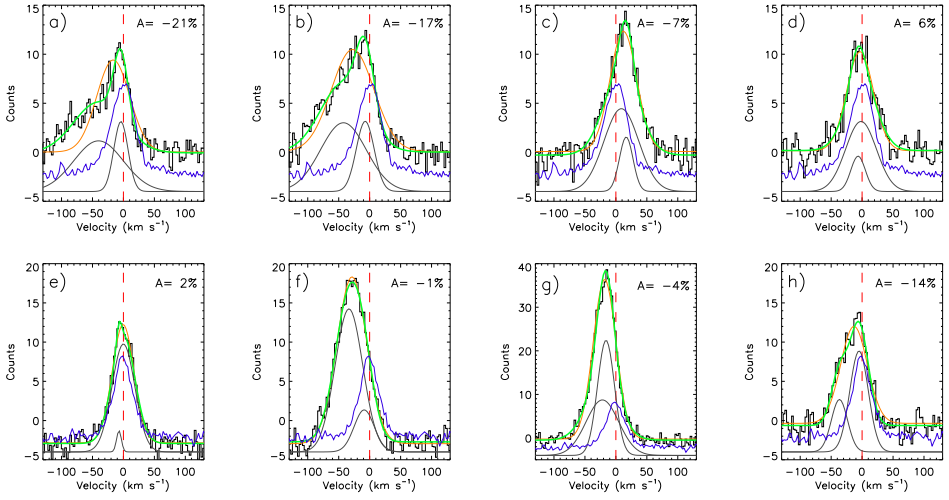

FIGURE 3.4: Representative line profiles at different positions as marked in Figure 3.3. Orange and green curves represent the best-fit single Gaussian and double Gaussian over spectra. Two components of the double Gaussian fit are shown in gray and shifted to the bottom for better visibility. The blue curve represents the average spectrum over the first 20 minutes of the observation at the respective positions.

In Figure 3.5, we show the wavelet analysis of spectral intensity, Doppler shift,

and line width at the plume footpoint marked by a triangle (see Figure 3.1). The missing values in the left panel of Figure 3.5 correspond to the positions where a single Gaussian could not be fitted due to low counts. The green stars marks in Figure 3.5 represent the instances we have chosen to show individual spectral profiles (see Figures 3.4 (e-h)). In the right panel global wavelet power peaks at 15.6 and 7.1 minutes for intensity, 26.2 and 7.1 minutes for Doppler velocity, and 11 and 17 minutes for line width. A small peak ∼16 minutes in global wavelet power of Doppler velocity is also present. The horizontal dashed line is the cutoff above which edge effects come into play; thus periods above the dashed line cannot be trusted. The dotted line marks the 99% significance level for a white noise process (Torrence and Compo 1998).

It is quite evident from Figure 3.5 that the instances of the intensity peaks correspond to instances of large Doppler shifts and line widths and the flux cancellation of emerging positive flux. The animation of Figure 3.1 shows the evidence of positive polarity field around the dominant negative polarity. Cancellation of a positive polarity at the edges of dominant negative polarity (region enclosed in a yellow box in the animation of Figure 3.1) leads to the formation of reconnection jets that are characterized by intensity enhancement in spectra and apparent outflows in IRIS 1330 Å SJIs.

3.2.3 Imaging Analysis

In order to compare dynamics at the transition region (as seen from IRIS) and the corona (as seen from AIA), we create smooth background-subtracted time–distance maps of AIA 171 and AIA 193 Å for the artificial slice 0 (see Figures 3.1 (c) and (d)) co-spatial with the IRIS slit shown in green color in Figure 3.1. We choose the width of the slice to be four pixels. We average along the width of the slice to increase signal to noise. Resulting time–distance maps are shown in

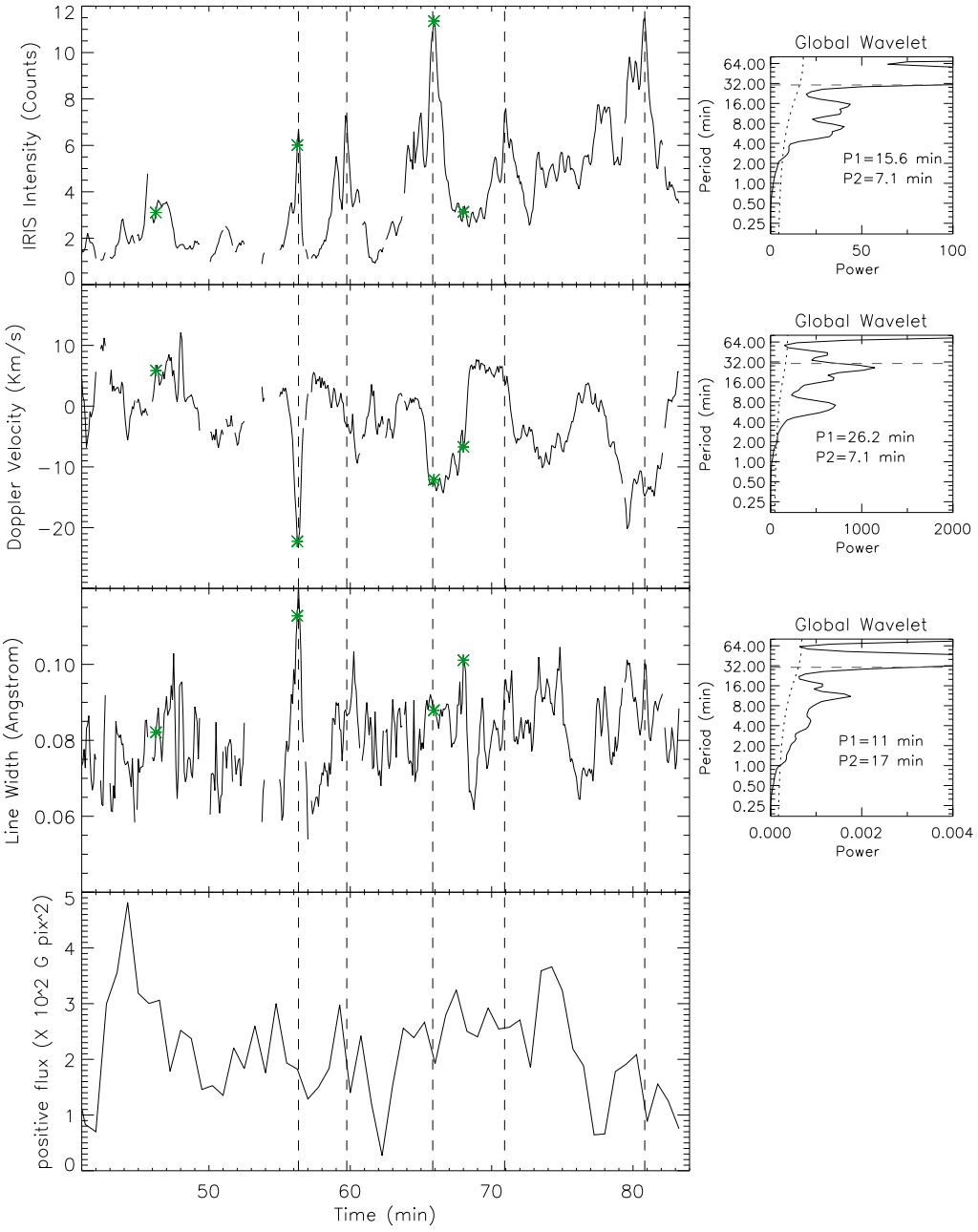

FIGURE 3.5: *Left*: Time variation of the Si IV line parameters at the triangle location (IRIS) and of the positive magnetic flux within the yellow box (HMI), as shown in Figure 3.1. The green stars identify the times at which we show individual spectral profiles in Figure 3.4. *Right*: Corresponding global wavelet power spectra. The 99% significance levels are overplotted with dotted lines. The first two significant periods are indicated.

Figure 3.6 (left panel). We observe quasi-periodic alternate bright and dark ridges. We fit the ridges with a straight line as done in Kiddie *et al.* (2012) and Krishna Prasad *et al.* (2012). We isolate a ridge and estimate the position of maximum intensity. We then fit the points of maximum intensity with a straight line, and thus the mean value of slope and error bars are estimated. The slope of the straight line gives an estimate of the speed of the PDs. Since we are interested in the average behaviour of the PD, we take the mean of the speeds of all the ridges, and therefore some of the ridges in AIA 171 Å seem to be more inclined than overplotted straight lines. We find the average velocity of PDs is 51±3 and 66±8 km s^{-1} in AIA 171 and 193 Å respectively.

We carry out a similar analysis for two artificial slices marked as 1 and 2 in Figures 3.1 (c) and (d) for AIA 171 and 193 Å respectively. The slices are placed by looking at the direction of propagation of significant PDs in unsharp mask images. The widths of slices 1 and 2 are chosen to be 5 and 6 pixels respectively. Corresponding time–distance maps with best-fit overplotted ridges for slices 1 and 2 are shown in Figure 3.6 (middle and right panels respectively). We note that the velocity is higher in the hotter channel (AIA 193 Å) and the ratio between the velocity observed in AIA 193 and 171 Å is 1.29±0.23, 1.23±0.1, and 1.32±0.07 (as compared to the theoretical value of 1.25 if the PDs are magnetoacoustic waves) for slices 0, 1, and 2 respectively.

We also estimate the velocities of PDs in slice 0, 1 and 2 using a cross-correlation method as done in Kiddie *et al.* (2012). We isolate individual ridges and estimate the time lag using cross-correlation between two positions. The velocity of the ridge is estimated by dividing the distance between two positions by the time lag. Thus, we compute the velocities of several ridges, and their mean value and standard deviation are estimated. Mean velocities and error bars (standard deviation for cross-correlation) using two different methods for slices 0, 1, and 2 are summarized in Table. 3.1.

Since the velocity is higher in the hotter channel (AIA 193 Å) using two different

TABLE 3.1: Velocity of PDs Using Two Different Methods of Ridge Fitting

Slice	Channel	Velocity (km s^{-1})	
		Using Best-fit Straight Line	Using Correlation
0	AIA 171 Å	51±3	61±12
	AIA 193 Å	66±8	81±11
1	AIA 171 Å	59±3	60±14
	AIA 193 Å	72.5±1	80±18
2	AIA 171 Å	72±5	63±10
	AIA 193 Å	95±3	83±25

methods, we believe that these are propagating slow magnetoacoustic waves. We carry out a wavelet analysis at positions marked with dashed lines in Figure 3.6 (left panel). We find that there exist at least two dominant significant periodicities close to the footpoint of the plume (see global wavelet power plot in Figure 3.7). We choose the significance level to be 99% for a white noise process. We find that the periodicities in intensity in AIA 171 and 193 Å at slice 0 are similar to those in IRIS Si IV 1402.77 Å peak intensity (see Figure 3.5 top panel). We also find that the periodicity of 7.2 minutes is present in both AIA 171 Å, AIA 193 Å and IRIS spectral intensity, which suggests that the quasi-periodic reconnection jet outflows could be responsible for quasi-periodic PDs seen in AIA 171 and 193 Å.

For slices 1 and 2 the rows marked with dashed lines in Figure 3.6 are used in the wavelet analysis (Figure 3.7). We find the two dominant periodicities of 13.2 and 7.2 minutes (24.3 and 7.2 minutes) and 17.1 and 6.6 minutes (26.4 and 6.6 minutes) in AIA 171 Å (193 Å) for slices 1 and 2 respectively (see Table 3.2).
We also carry out the wavelet analysis at other positions (10 Mm and 15 Mm in x–t map). The results are summarised in Table 3.2.

Since the periodicity ∼7 minutes is present in slices 0, 1, and 2, we create time–distance maps using Fourier filtered images. We perform a Fourier transform at

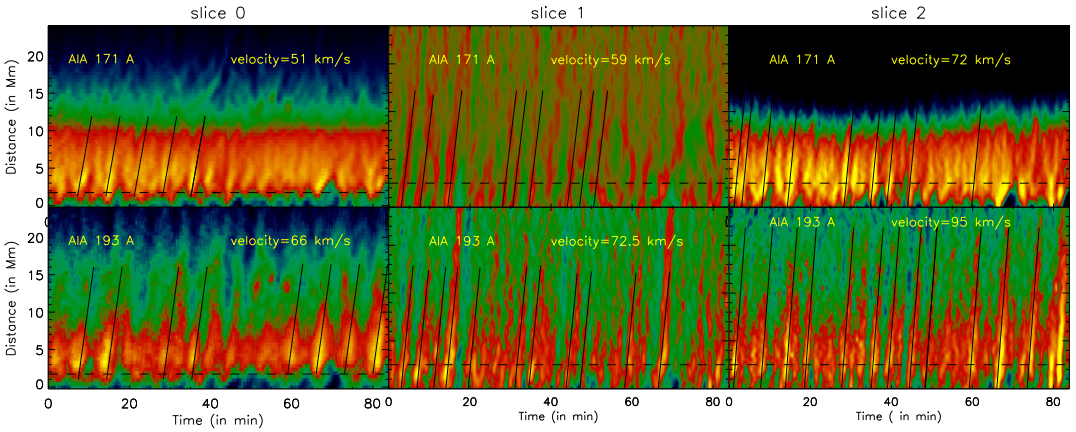

FIGURE 3.6: (Top panels): *left*: Smooth background-subtracted x–t map of slice 0 as shown in Figure 3.1 (c) for AIA 171 Å. Ridges are overplotted with the best-fit straight line. *Middle*: Smooth background divided x–t map of slice 1 for AIA 171 Å. Ridges are overplotted with the best fitted straight line. *Right*: Same as (a) for slice 2. The dashed black line represents the position used for wavelet analysis as shown in Figure 3.7. (Bottom panels): same as the top panel for AIA 193 Å.

each pixel location. Fourier power is then multiplied by a Gaussian peaking at 7 minutes with FWHM of ∼1 minute and the inverse Fourier transform is applied to get the reconstructed light curve at the same pixel location. The animations of the Figure 3.9 showing Fourier filtered movies of AIA 171 and 193 Å are available online. Time–distance maps for slices 1 and 2 using Fourier filtered images are shown in Figure 3.9. We find that the periodicity of ∼7 minutes is significant in AIA 193 Å and mostly toward the end of observation (from 60 to 80 minutes in Figure 3.9 lower right panel) at the position of slice 2. This is also evident from wavelet plots as shown in Figure 3.8 where we note that a periodicity of ∼7 minutes is present at the position of the slice 2 at the start and toward the end of the observation from 60 to 80 minutes (see Figure 3.8 (d)). This fact is also supported by the animations of the Figure 3.9 where we see the significant PDs propagating outwards at the position of slice 2 toward the end of observation. A Similar behaviour is found in AIA 171 Å wavelet plots in slices 1 and 2 but the presence of the 7 minutes periodicity at later times is most prominent in AIA 193 Å at the position of slice 2. This indicates that these PDs are triggered by some drivers at specific instances.

TABLE 3.2: Dominant Periodicity Using Wavelet Transform

Slice	Distance Along Slice	AIA 171 Å		AIA 193 Å	
	(Mm)	P1 (minutes)	P2 (minutes)	P1 (minutes)	P2 (minutes)
0	2	14.4	7.2	7.9	14.4
	5	5.6	9.4	7.2	12.1
	10	22.2	6.6	13.2	7.2
	15	12.1	7.2	12.1	7.2
1	2.5	13.2	7.2	24.3	7.2
2	2.5	6.6	–	26.4	6.6

Since significant PDs are observed at later times at the position of slice 2, we fit the significant ridges with a straight line between 60 and 80 minutes in AIA 171 Å and 193 Å. Fourier filtered time–distance maps for slit 2 as shown in Figure 3.9 right panel. The method of fitting is the same as explained in Section 3.2.3. We estimate the velocity to be 64±3 km s^{-1} (73±3 km s^{-1}) and 55±3 km s^{-1} (79±2 km s^{-1}) in AIA 171 Å (193 Å) for slices 1 and 2 respectively. We find that PDs of 7 minutes period are propagating with larger velocity in the hotter channel (AIA 193 Å) which further supports the fact that these could be propagating slow magnetoacoustic waves. However, we would like to point out that the PDs of 7 minutes period are not so clearly observed in AIA 171 Å and we see uneven ridges that could affect the velocity estimation. At the position of slice 1 (Figure 3.9 left panel) PDs of 7 minutes period are not clearly seen maybe because the period of 7 minutes is not the dominant one in the time series as shown in Figure 3.8 (a). Thus we could fit only two ridges, one at 15 minutes and another at 65 minutes after the start of observation. We fit the corresponding ridges in AIA 193 Å and find that in slice 1, too, the velocity is higher in the hotter channel.

3.2.3.1 Jet-like features in SJI 1300 Å

In this subsection, we study the dynamic properties of the observed jet-like features. To determine the apparent speed of jets seen at the network boundary we

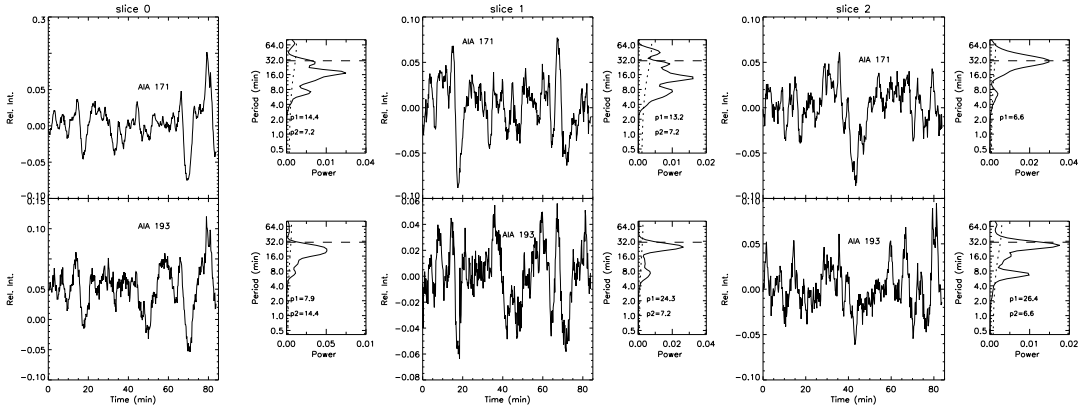

FIGURE 3.7: (Top panels): *left*: detrended light curves corresponding to black dashed lines for slice 0 as shown in Figure 3.6 left panel. Corresponding global wavelet plots are shown with the first two dominant periods. *Middle*: same as the left panel for slice 1. *Right*: same as the left panel for slice 2. (Bottom panels): same as the top panel for AIA 193 Å.

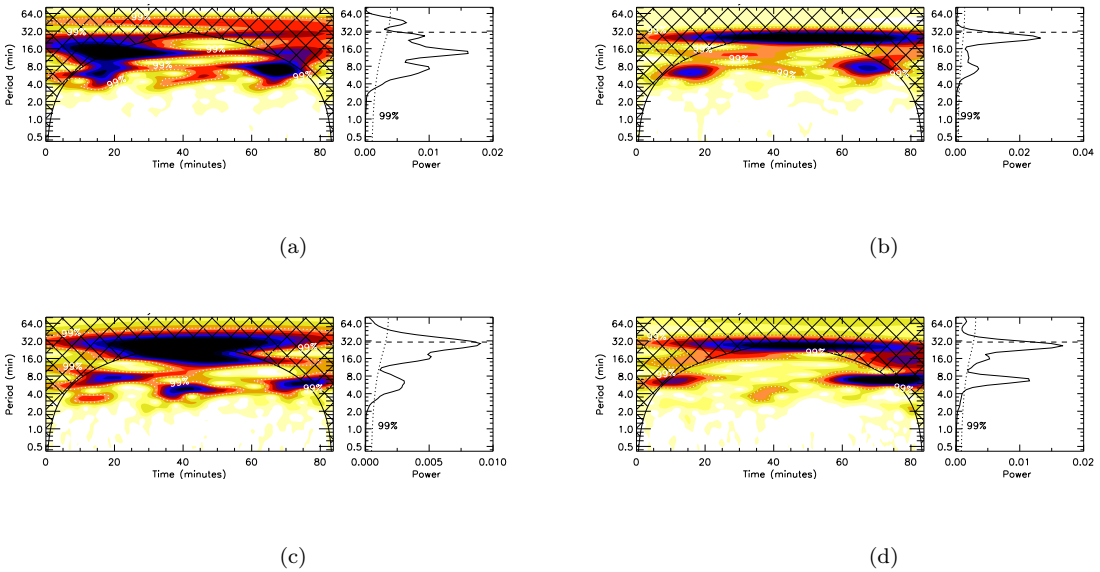

FIGURE 3.8: (a) Wavelet map and global wavelet of AIA 171 Å for slice 1 at position marked as dashed line in Figure 3.6. (b) Same as (a) for AIA 193 Å. (c) Wavelet map of AIA 171 Å for slice 2 at position marked as dashed line in Figure 3.6. (d) Same as (c) for AIA 193 Å.

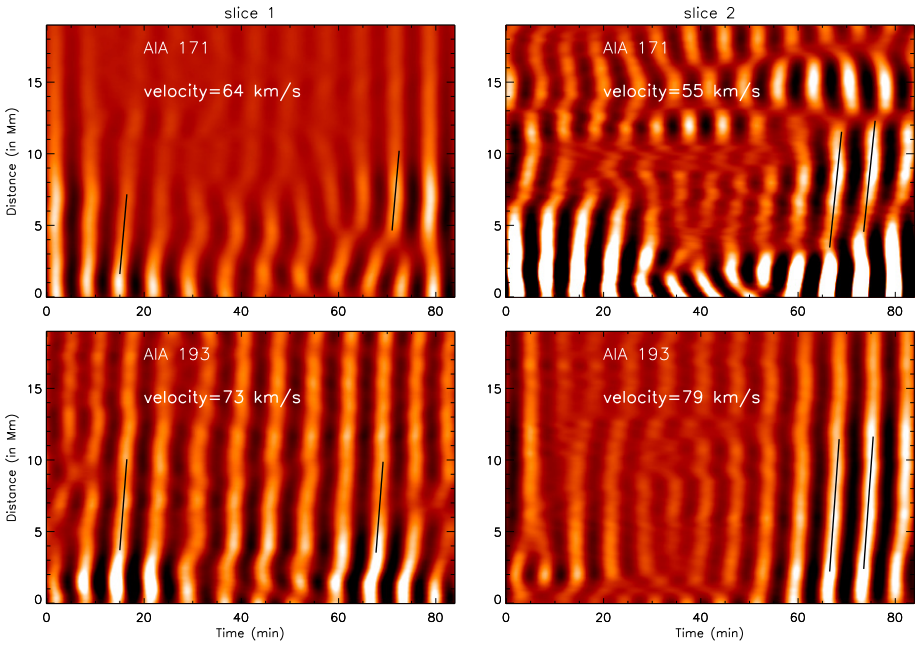

FIGURE 3.9: (Top panels): *left*: x–t map at the position of slice 1; *right*: x–t map at the position of slice 2 as shown in Figure 3.1 (c) using the 7 minutes Fourier filtered AIA 171 Å image overplotted with the best-fit straight line using the method mentioned in Section 3.2.3. (Bottom panels): same as the top panel for AIA 193 Å.
(Two animations of this figure are available.)

place nine artificial box slices five pixels wide in SJI 1330 Å as shown in Figure 3.1 (a). Slices are placed based on the direction of propagation of significant jets as seen in SJI 1330 Å in the animation of Figure 3.3 (available online). We average along the width of each box slice to increase signal to noise ratio. Corresponding time–distance maps are shown in Figure 3.10. In the time–distance maps we fit significant ridges with straight lines. We find that several jets are preceded by brightenings seen in time–distance maps, which suggests that small-scale reconnections could be triggering these jet-like features. We identify 62 jet-like features and fit them with dashed green curves as shown in Figure 3.10. The slope of the overplotted green dashed line gives an estimate of the apparent speed of the jet projected in the plane of sky. The velocity distribution of these jet-like features is shown in Figure 3.10 (last panel). We find that the distribution peaks around 10 km s^{-1}, which is similar to what has been reported by Shibata *et al.* (2007). Apart

from outflows we see several downflows in the time–distance maps, which suggests that a certain amount of the jet material is falling back (see slit 4 in Figure 3.10).

3.2.3.2 Correspondence between Jet-like features in SJI 1300 Å and PDs in AIA 171 and 193 Å

In this subsection, we explore whether the jet-like features can be responsible for the generation of the PDs.

To understand the source of PDs generated in the corona, we compare the spectral intensity of IRIS slit spectra at the footpoint (marked by the triangle in Figure 3.1) and the intensity of PDs observed in the time–distance map of slit 0 (see Figure 3.6) at 2 Mm, which coincides with the position of the triangle marked in Figure 3.1, for AIA 171 and 193 Å. The left panel of Figure 3.11 compares the peak intensity of IRIS slit spectra (top left), PDs (along slit 0) observed in AIA 171 Å (middle left) and PDs (along slit 0) observed in AIA 193 Å (bottom left). The dotted–dashed line in black represents the peak spectral intensity while the green line represents the corresponding intensity peaks in AIA 171 and 193 Å. We find that IRIS spectral intensity peaks precede the AIA intensity peaks and we estimate a lag of 24–84 s with a mean lag of ∼60 s.

Some of the peaks in spectral intensity do not correspond to sharp peaks in AIA 171 and 193 Å, maybe because the jet is aligned sideways, and does not move along the slice 0 placed co-spatially with the IRIS slit. We also compare the light curves at 0.5 Mm at box slice 8 placed in SJI 1330 Å (see Figure 3.1 (a)) and 3 Mm at box slice 2 placed in AIA 171 and 193 Å (see Figures 3.1 (c) and (d)). These two positions are also co-spatial.

From Figure 3.11, we note that there is fairly good one-to-one correspondence between jet-like features in slice 8 in IRIS SJI and PDs in slice 2 in AIA 171 and 193 Å. The dotted–dashed line represents the peak in IRIS SJI intensity. We also note that there is no significant lag except at the last ridge (marked by the

dotted–dashed green line) where the lag is ∼120 s. We carry out a similar analysis for co-spatial positions at slice 3 placed in SJI 1330 Å and at slice 1 placed in AIA 171 and 193 Å. We found a lag of 84 s at two positions marked with green dotted–dashed lines.

It should be noted that the time lag between peaks in IRIS SJI and AIA is not uniform. Apart from the fact that some jets are preceded by the brightenings in x–t maps, at some positions we may not capture the exact time when a jet starts in IRIS SJI (see slice 8 in Figure 3.10 between 40 and 80 minutes). What we know is when a jet appears at the position of slices placed in IRIS SJI. It is also possible that when jets appear in a given slice, they have already covered some distance in the vertical direction (projection effect) and have generated the PDs visible in coronal channels. Thus they may appear co-temporal with PDs observed in AIA 171 and 193 Å.

These results allow us to propose that jet-like features in the transition region may cause PDs as observed in the corona.

3.3 Summary and Conclusions

We study the dynamics at the footpoints of an on-disk plume adjacent to a coronal hole using combined imaging, spectroscopic and magnetic measurements. We find that there is continuous emergence of new magnetic flux of positive polarity and there is fairly good correspondence between intensity enhancement and the positive magnetic flux cancellation. This suggests that the emerging flux interacts with the existing fields, which results in reconnection and cancellation of the flux, resulting in small jet-like outflows termed as "jetlets" as observed in AIA by Raouafi and Stenborg (2014). They conjectured that such small-scale jets are the consequences of flux cancellation at the footpoints of the plume. We think that

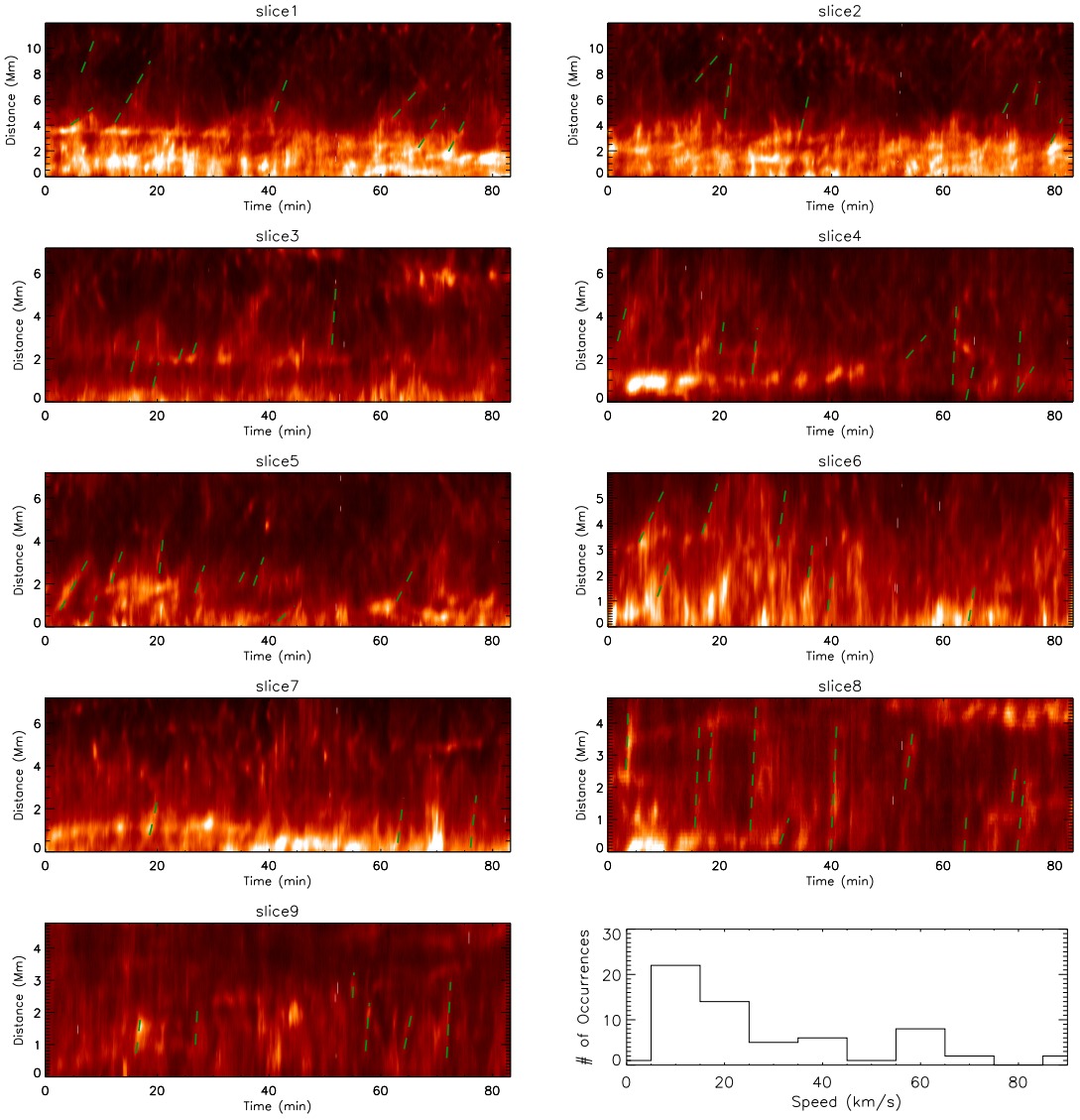

FIGURE 3.10: x–t maps for nine box slices as shown in Figure 3.1 (a). The significant ridges in x–t maps are overplotted with dashed straight lines marked in green. The slope of the ridges gives an estimate of the velocity of the outward moving features (jet-like features). The distribution of jet apparent speeds is shown in the last panel. It peaks at 10 kms^{-1}.

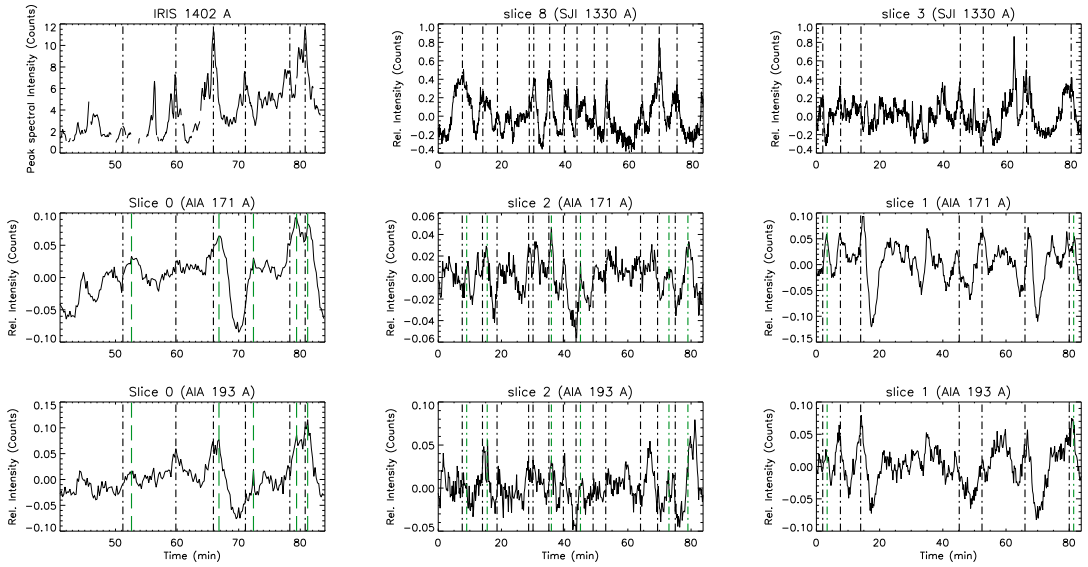

FIGURE 3.11: (Left panel): *Top*: IRIS spectral intensity at the position marked by the triangle in Figure 3.1. *Middle*: Light curve of AIA 171 Å at the same position. *Bottom*: Same as the middle panel but for AIA 193 Å. Black dotted–dashed lines correspond to the peak in spectral intensity. Green dotted–dashed lines mark the corresponding peaks in AIA 171 and 193 Å. The time lag can be estimated by estimating the time difference between the black and green lines. (Middle panel): *Top*: IRIS SJI 1330 Å light curve at 0.5 Mm for the x–t map created using box slice 8 as shown in Figure 3.10 (a). *Middle*: AIA 171 Å light curve at 3 Mm (co-spatial with the position of the light curve of the top middle panel) for the x–t map created using box slice 2 in AIA 171 Å as shown in Figure 3.6 (top right panel). *Bottom*: AIA 193 Å light curve at 3 Mm for the x–t map created using slice 2 as shown in Figure 3.6 (bottom right panel). (Right panel): Same as the middle panel at a position co-spatial with slice 3 as shown in IRIS SJI and slice 1 in AIA 171 and 193 Å.

jet-like features observed by Raouafi and Stenborg (2014) are the PDs that we observe in AIA channels. They associated the jetlets seen in AIA channels with the underlying magnetic flux change. In this study, we report that underlying magnetic flux changes generate jet-like features, which trigger PDs in the corona. These PDs can be explained in terms of magnetoacoustic waves. The small-scale jets are quite evident in the IRIS 1330 Å SJIs (Movie 2 online) and the signature of reconnections is also prominent in the evolution of the line profiles. We observe enhanced line profile asymmetry, enhanced line width and large deviation from the average Doppler shift at specific instances. Association of plumes with supergranular network boundaries has been studied by several authors. In this study,

we find that plume footpoints coincide with network boundaries as seen in IRIS 1330 Å SJI. Observations of the origin of these jet-like features in connection with plumes are still lacking. Footpoints of plumes are just enhanced network boundaries where we often see clear network jets in IRIS SJIs (Tian *et al.* 2014). The IRIS spectra at a plume footpoint show the presence of more than one Gaussian component, enhanced wings, high Doppler shifts and large fluctuations in intensity. This confirms the presence of flows (Tian *et al.* 2011a, 2012) at the footpoint of the plume. These jet-like features load mass into plumes.

We estimate the speed of the jet-like features by placing several slices in IRIS SJI. These jet-like features originate from network boundaries due to small-scale magnetic reconnections. We find that the speed distribution peaks at 10 kms^{-1} which is the typical velocity for a chromospheric anemone jets as reported by Shibata *et al.* (2007). Thus most of the jets could be chromospheric in origin. Recently, Rouppe van der Voort *et al.* (2015) have reported jets of similar velocity range seen in IRIS SJI 1330 Å to be associated with rapid blueshifted or redshifted excursions seen in Hα images. We find speeds of jets that are far lower than the 150 km s^{-1} reported in Tian *et al.* (2014). The datasets used by Tian *et al.* (2014) were centered on CHs while in this study the plume is located in quiet Sun region. The open field lines in CHs may accelerate the jets to larger velocities. Apart from this, the effect of projection of jets in the plane of the sky cannot be ruled out.

We compare IRIS spectral intensity with PDs observed in AIA 171 and 193 Å and find that at several time instances the intensity enhancement in IRIS spectra precedes PDs observed in AIA channels. We find a lag of 24–84 s with a mean lag of 60 s. We also compare jet-like features in IRIS SJI with PDs observed in AIA channels at two different slice positions and find fairly good correspondence. However, at some instances we could not find one-to-one correspondence between IRIS SJI jet-like features and PDs observed in AIA channels. One reason could be that if jets are short-lived then they appear in IRIS SJIs but PDs in the corona may not be observed. We should point out that IRIS SJI 1330 Å has a strong contribution from C II which forms in the upper chromosphere. Thus IRIS SJI 1330 Å reflects

the upper chromosphere and lower transition region, while emission in AIA 171 and 193 Å represents the million degree plasma. Thus if reconnection happens at larger heights (upper transition region or lower corona) and the plasma is heated to coronal temperatures then we may see faint jets in IRIS SJI but strong PDs in AIA channels. In this scenario our observed jets may not propagate to greater heights and they may not be responsible for the generation of PDs in the corona. In the future, one can address this issue with better coordinated observations at several heights from chromosphere to corona. Therefore, we propose that there is some observational evidence that jet-like features at network boundaries may cause the generation of PDs in the corona.

Time–distance maps for AIA 171 and 193 Å reveal that the speed of quasi-periodic propagating intensity disturbances is larger in the hotter channel (AIA 193 Å) than in AIA 171 Å. Therefore, we believe that these are propagating slow magnetoacoustic waves. Ofman *et al.* (2012) reported that the impulsive onset of flows with subsonic speed results in excitation of damped slow magnetoacoustic waves in active region loops. Wang *et al.* (2013) performed 3D MHD modelling of active region fan loops and report that the PDs observed in coronal fan loops are due to several tiny upflows caused by nanoflares at the loop footpoints. Nishizuka and Hara (2011) reported the presence of flows close to the footpoint and upward propagating slow magnetoacoustic waves at higher locations using EIS on board *Hinode*. Thus it appears that any form of reconnection outflow may generate slow waves in an expanding loop system. In this study, we report that the periodicities of intensity disturbances found in the corona using AIA 171 Å and 193 Å match well with periodicities found in IRIS spectral intensity and in IRIS SJI intensity in the transition region. Therefore, some jets observed in the transition region may be connected to PDs observed in the corona. This fact, together with the good correspondence between some jet-like features in IRIS images and some PDs in AIA coronal passbands, allows us to propose that the small jet-like upflows (jetlets) at lower heights (the transition region) are the drivers of slow magnetoacoustic waves seen at coronal heights in plumes.

Chapter 4

Transverse oscillations in a coronal loop triggered by a jet[†]

4.1 Introduction

Magnetohydrodynamics (MHD) waves are ubiquitous in the solar atmosphere. With the advent of high-resolution observations after the launch of the Solar and Heliospheric Observatory (SOHO), the Transition Region and Coronal Explorer (TRACE), Hinode, the Solar Terrestrial Relations Observatory (STEREO), and the Solar Dynamics Observatory (SDO), MHD waves have been well studied in recent years (Aschwanden *et al.* 1999; Nakariakov *et al.* 1999b; Ofman and Wang 2002; O'Shea *et al.* 2007; Verwichte *et al.* 2009; Srivastava and Dwivedi 2010; Aschwanden and Schrijver 2011; White and Verwichte 2012; Mathioudakis *et al.* 2013).

[†]Results of this work are published in Sarkar *et al.* (2016).

All the animations that are referred to in this chapter are available at `http://dx.doi.org/10.1007/s11207-016-1019-6`

The MHD waves and oscillations provide an important input in diagnosing the local plasma conditions using the principles of MHD seismology; as first suggested by Uchida (1970) using Moreton waves and Rosenberg (1970) using intensity fluctuations associated with type IV radio emission. Using the principles of MHD seismology, the magnetic field strength in the solar corona was estimated by Aschwanden *et al.* (1999), Nakariakov (2000), Nakariakov and Ofman (2001), Schrijver *et al.* (2002), Aschwanden *et al.* (2002), Nakariakov and Verwichte (2005), Aschwanden (2006), Ruderman and Erdélyi (2009), and Aschwanden and Schrijver (2011).

Edwin and Roberts (1983) and Roberts *et al.* (1984) interpreted transverse oscillations as a nearly incompressible fast kink mode in the MHD regime. The first observations of transverse oscillations in coronal loops were reported by Nakariakov *et al.* (1999b), Aschwanden *et al.* (1999), and Schrijver *et al.* (1999). Transverse loop oscillations are often excited by nearby flares (Aschwanden *et al.* 1999; Nakariakov *et al.* 1999b; Hori *et al.* 2005; Verwichte *et al.* 2010a; Wang *et al.* 2012) and reconnection at the loop top (White and Verwichte 2012). Other methods of measuring coronal magnetic field include gyro-resonance modelling of radio emission (Lee *et al.* 1999), but this can only be applied to strong magnetic field regions like sunspots.

Transverse oscillations are often found to be damped most likely as a result of resonant absorption (Ruderman and Roberts 2002; Goossens *et al.* 2002; Hollweg and Yang 1988). Recently, there have been a few reports on decayless oscillations in coronal loops (Nisticò *et al.* 2013; Anfinogentov *et al.* 2015). The driving mechanisms of such oscillations are not clearly understood. Recently, Zimovets and Nakariakov (2015b) have provided a statistical investigation of coronal loop oscillations observed with the SDO in association with blast waves that were due to a nearby flare, coronal mass ejections, type II radio bursts, etc. The authors found that kink oscillations ($\sim$95% of them) were triggered by nearby low coronal eruptions (LCE) observed in the extreme ultraviolet band. Thus different types of

transients can trigger oscillations in nearby magnetic structures, which provides additional data for coronal seismology. Here we explore whether transients such as jets, which carry much less energy than coronal mass ejections (CMEs) or blast waves, can trigger oscillations in nearby coronal loops.

In Section 4.2 we report the observations and the data analysis. In Section 4.3 we describe the observations from STEREO. In Section 4.4 we present a time–distance analysis to study the dynamics of the jet, which is followed by Section 4.5, where we carry out MHD seismology to estimate the magnetic field strength. In Section 4.6 we calculate the energy stored in jet and coronal loop oscillations. In Section 4.7 we report the coupling between oscillations in the jet with coronal loop oscillations, which is followed by our conclusions.

4.2 Observations and Data analysis

A jet was observed at the south-east limb of the Sun on 19 September 2014 at 02:01:35 UT. A narrow CME was detected at 04:37 UT with the Large Angle Spectroscopic Coronagraph (LASCO) on board SOHO. The CME may be the coronographic counterpart of the jet (Feng *et al.* 2012; Paraschiv *et al.* 2010; Nisticò *et al.* 2009). The observation was made using the extreme ultraviolet (EUV) passbands of the Atmospheric Imaging Assembly (AIA) on board SDO. The AIA instrument provides almost simultaneous full-disk images of the Sun at ten different wavelengths, of which seven are in the EUV band. AIA has a spatial resolution of 1.3″, a pixel size of 0.6″ and a cadence of 12 s (Lemen *et al.* 2012b). At 02:12:11 UT (∼12 minutes after the jet was started), transverse oscillations in a coronal loop were observed. The region where the jet and the coronal loop were observed is outlined with a red box in Figure 4.1. The jet is marked with an arrow. A sequence of images was taken, encompassing 1.5 hr, covering 1 minute before

and 1.48 hr after the jet. Since the jet becomes fainter as it propagates outward, we made an unsharp mask movie to clearly show the propagation of the jet and its interaction with the coronal loop (see movie 1 online). We note that only one complete transverse oscillation of the coronal loop was clearly observed. Moreover, we also note that the jet oscillates in the transverse direction to its propagation (see Section 4.4).

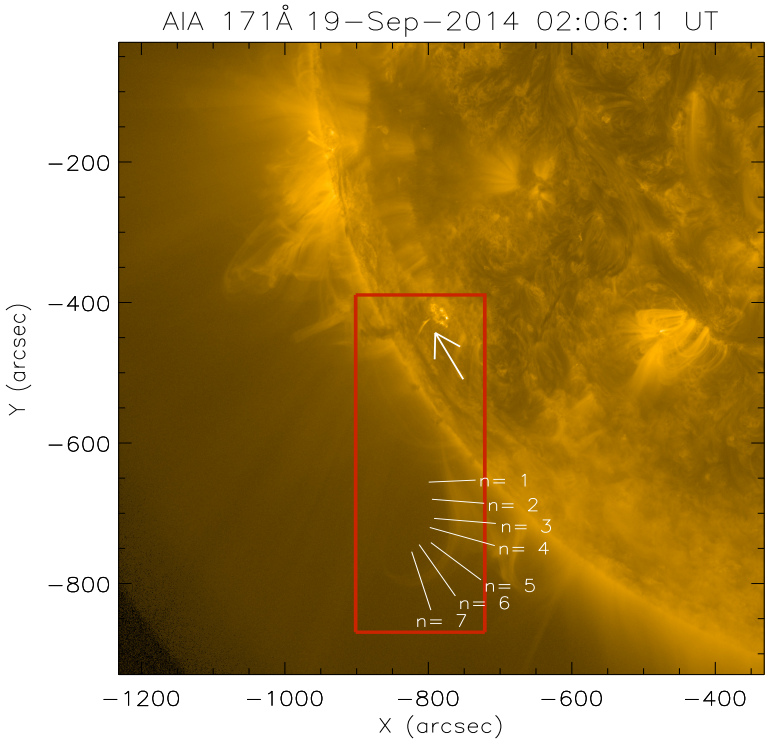

FIGURE 4.1: AIA/SDO image of 171 Å, taken on 19 September 2014 at 02:06:11 UT. The red box highlights the jet (top) and the coronal loop (bottom). The white arrow points at the location of the jet. Seven artificial slices are placed perpendicular to different parts of the loop to detect the transverse oscillations (see Figure 4.3). An animation is available online as movie 1.

Figure 4.1 shows that only half of the coronal loop is clearly visible. To enhance the contrast, we smoothed the images (to remove noise) and convolved them with the Laplacian operator to enhance the regions of the sharp change in brightness. The processed image is shown in the left panel of Figure 4.2. In order to estimate the length of the loop, we use the image obtained after the application of Laplacian operator and choose ten points along the length of the loop. Then we interpolate

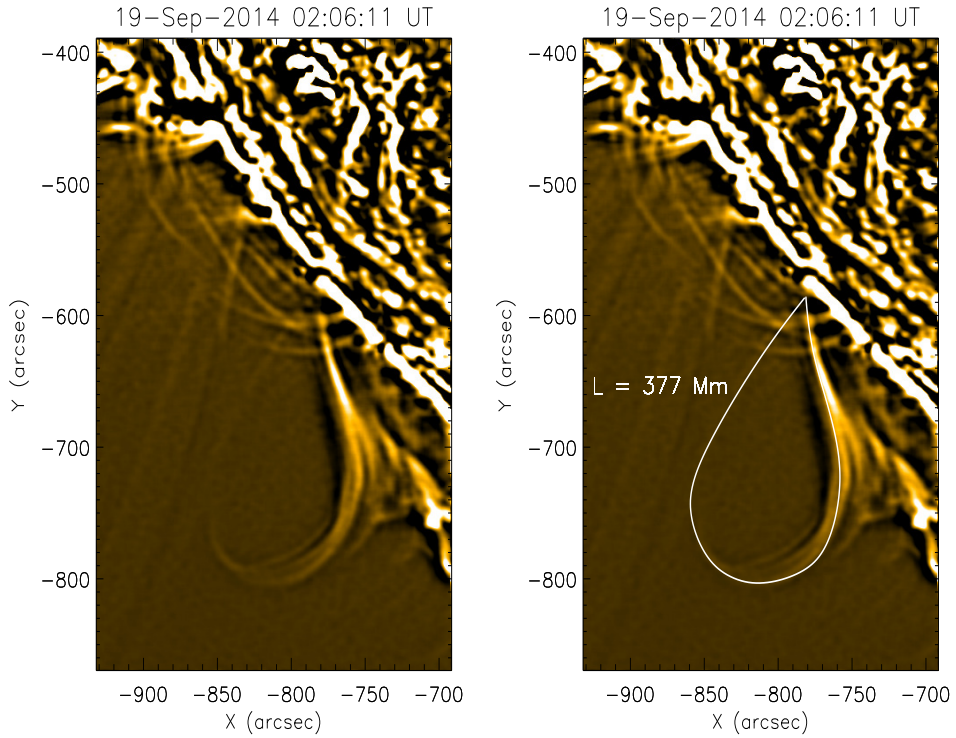

FIGURE 4.2: The left panel shows the coronal loop using feature enhancement by the Laplacian operator. The right panel shows the tracing of the loop, using cubic spline fitting.

a curve passing through these points using cubic spline fitting as shown in the right panel of Figure 4.2. This procedure is repeated several times to calculate the mean projected length L and the standard deviation of the coronal loop; which is estimated to be $\sim$ 377 Mm and 7 Mm, respectively. The length of the coronal loop estimated using this method can be taken as a lower limit of the loop length. Furthermore, we estimate the length of the loop assuming it to be a semicircle. We calculate the radius by estimating the distance between the solar limb and the coronal loop top. Since there is uncertainty in the estimation of the coronal loop top (because the coronal loop is quite thick), we take the thickness of the coronal loop as the error in the measurement of the radius. Using this, we estimate the length of the coronal loop to be 539 $\pm$ 30 Mm. This can be taken as the upper limit of the loop length. It is worth noting that the calculated radius is projected in the plane of sky. Thus the estimated length of the coronal loop still underestimates its true length.

4.2.1 Transverse oscillations in the coronal loop

Seven artificial slices are placed perpendicular to the coronal loop to detect transverse oscillations. Corresponding to each slice, we generate a time–distance map, which is henceforth referred to as x–t map throughout the chapter. The x-axis represents time and the y-axis represents the distance along the slice.

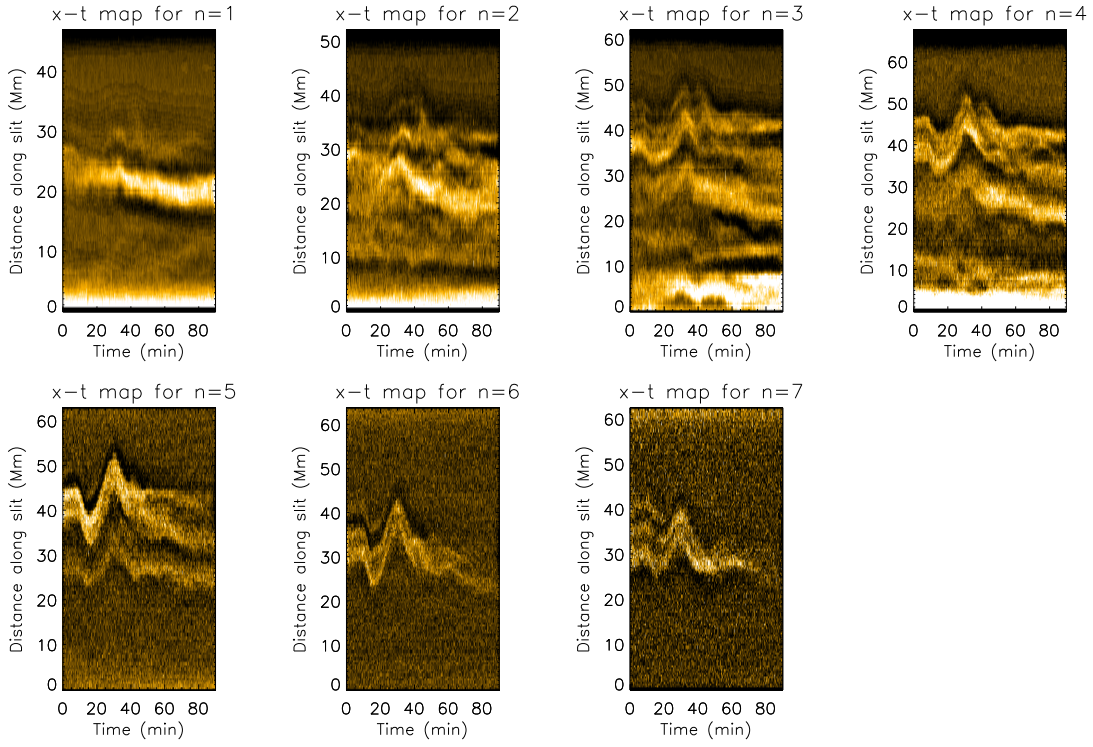

FIGURE 4.3: Sharpened x–t maps corresponding to the seven slices placed on the loop (see Figure 4.1). x–t maps were sharpened using an unsharp mask. The x–t graph shows the evidence of transverse oscillations in the coronal loop. We also note that the coronal loop is not monolithic, but a bundle of fine strands that oscillate coherently.

Time-distance maps are sharpened using the unsharp mask technique. The sharpened maps are shown in Figure 4.3. It is quite evident from the x–t maps that the coronal loop undergoes transverse oscillations. It is also worth noting that

the loop under study is not monolithic, but consists of many fine strands, which oscillate coherently.

To calculate the dynamic parameters for the coronal loop, first a Gaussian is fitted along each column of a given x–t map, and the mean values and one-sigma errors are estimated. We apply this procedure on the x–t maps for slices n = 4, 5, 6, and 7 only because slices n = 1, 2, and 3 are located near the footpoint of the coronal loop, thus the displacement of the coronal loop is very small. Moreover, near the footpoint of the coronal loop under study, there are many other fine loops along the line of sight that make the detection of transverse oscillation even more difficult. From the x–t maps, we note that the oscillations have a very poor quality factor (only one complete cycle is observed with no clear gradual decrease of the amplitude), and therefore we fit the x–t maps with an undamped sinusoidal function having the expression

$$A(t) = C + A_0 \sin(\omega t + \phi) \ , \tag{4.1}$$

where C is the equilibrium position of the loop, A_0 is the displacement amplitude, ω is the oscillation frequency, and ϕ is the phase.
We use the MPFIT function (Markwardt 2009) in the Interactive Data Language (IDL) to obtain the best-fit values of the undamped sinusoidal equation parameters. The best-fit sinusoidal curves with the best-fit parameters are shown in Figure 4.4.

From the fitted curves in Figure 4.4, we estimate the average oscillation period ($P = \frac{2\pi}{\omega}$) to be $\sim$32$\pm$5 minutes. We note that oscillations at different positions along the coronal loop are in phase. This oscillation mode is called the global kink mode. We also note that the one footpoint of the loop appears to be anchored at the limb. Using the Laplacian filtered image (see Figure 4.2), we find that the other footpoint may be anchored behind the limb, thus we infer that this oscillation

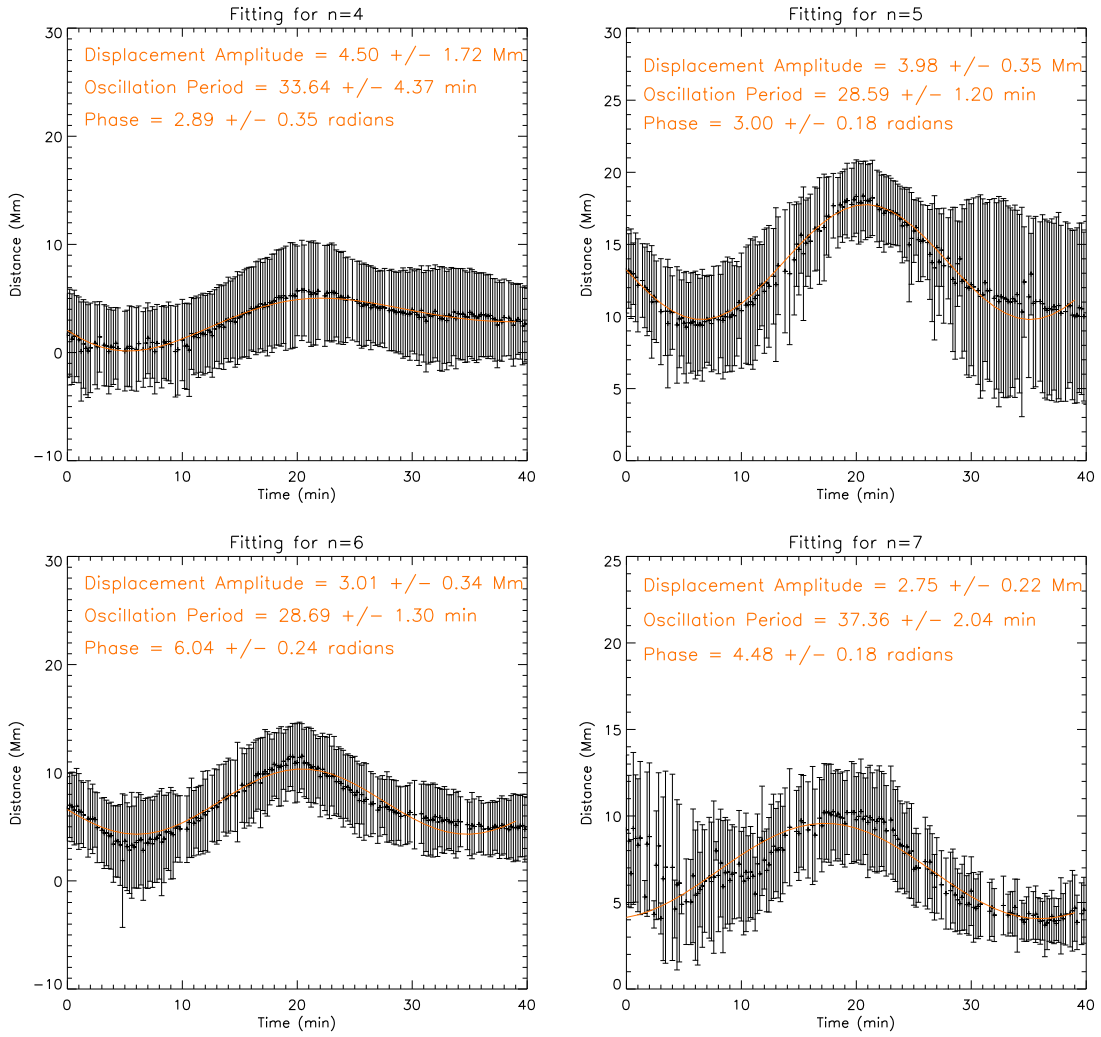

FIGURE 4.4: Best-fit sinusoidal curves with fitting parameters for four slices denoted by n = 4, 5, 6, and 7.

mode is the fundamental standing mode.

4.3 Observations using STEREO

In this section, we use STEREO/EUVI-B 171, 195, and 304 Å images to obtain an additional perspective of the coronal loop and the jet. We explore whether it is possible to obtain a stereoscopic view of the loop and the jet. In Figure 4.5, the

limb of the Sun as seen from AIA is overplotted on an EUVI 171 Å image, and the solar limb as seen from EUVI is overplotted on an AIA 171 Å image. We find that the jet source region is not observed in the EUVI 171 Å image because it is behind the limb. Since the cadence of EUVI 171 Å is one hour, we could not see the trajectory of the jet in EUVI 171 Å. In addition to this, only a few parts of the coronal loop under study are seen in EUVI 171 Å. The possible position of the loop under study is marked with a red arrow in EUVI 171 Å. The corresponding position in AIA 171 Å is also marked with a red arrow. We could not associate the loop features seen from EUVI 171 Å with the corresponding loop features seen from AIA 171 Å. For example, the loop we see in EUVI 171 Å (marked with a red arrow in EUVI 171 Å) could be the other footpoint of the coronal loop that is not clearly seen in the AIA 171 Å image (marked with a red arrow in AIA 171 Å). Thus it is extremely difficult to perform the triangulation in this scenario. We repeat the same analysis with EUVI 195 Å images (see Figure 4.6). Since EUVI 195 Å has a better cadence of 5 minutes, we are able to see the jet in one frame in EUVI 195. We have made a normal-intensity movie and a difference movie (movies 3 and 4) to illustrate it. Similarly the jet is also seen in EUVI 304 Å difference images (see Figure 4.7). We have also made normal-intensity and a running-difference movies (movies 5 and 6) using EUVI 304 Å and AIA 304 Å.

4.3.1 EUVI 195 Å

In the difference movie of EUVI 195 Å and AIA 193 Å (movie 4), a disturbance is seen to be moving inward towards the solar disk in EUVI 195 Å. On close inspection of EUVI 195 Å images (see movie 3), we note that the plasma disappears at the location where we see a dark feature in difference images. It starts near the limb and propagates inward towards the disk (marked in Figure 4.8 (left panel)). This disappearance of plasma is visible as a dark feature in EUVI 195 Å difference images (see Figure 4.8). This is unlikely to be caused by an eruption because

then it would have been propagating outward. However, if the eruption is oblique towards the disk center (which is not the scenario in this case) then it may appear to be propagating inward. Some scenarios might explain this: the disappearance may have been caused by the heating of the plasma from a nearby flare or some other event (a jet in this case) that transfers the energy to the surrounding medium. Secondly, a change in the magnetic field topology may have been brought about by magnetic reconnection, which might have caused plasma to escape through open field lines, which would appear as a dark feature in EUV 195 Å. Furthermore, it is also possible that the inward feature that is seen in EUVI-B 195 Å is the jet material falling down to the surface following the local magnetic field lines. We note from movie 4 that the dark feature first appears in AIA 193 Å. It interacts with the coronal loop and displaces it. Subsequently, it appears in EUVI 195 Å and propagates inward. This means that the disturbance seen in EUVI 195 Å must be associated with the jet as seen in AIA.

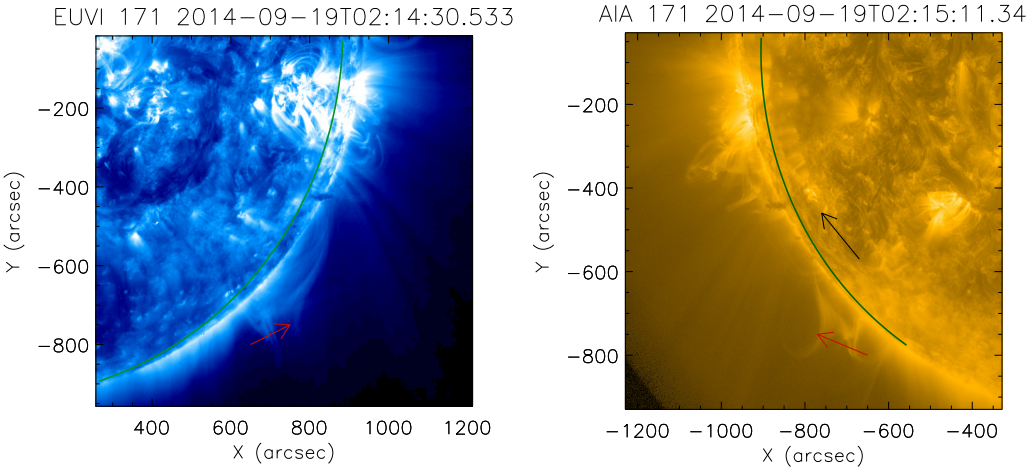

FIGURE 4.5: Left: STEREO/EUVI 171 Å image with the solar limb as seen from AIA 171 Å overplotted in green. The possible position of the loop corresponding to the loop seen in AIA 171 Å is marked with a red arrow. Right: SDO/AIA 171 Å image with the limb as seen from EUVI 171 Å overplotted in green. The loop under study is marked with a red arrow. The black arrow represents the location of the source region (footpoint) of the jet. Since the source region is behind the limb as seen from EUVI, it is not seen in the EUVI 171 Å image.

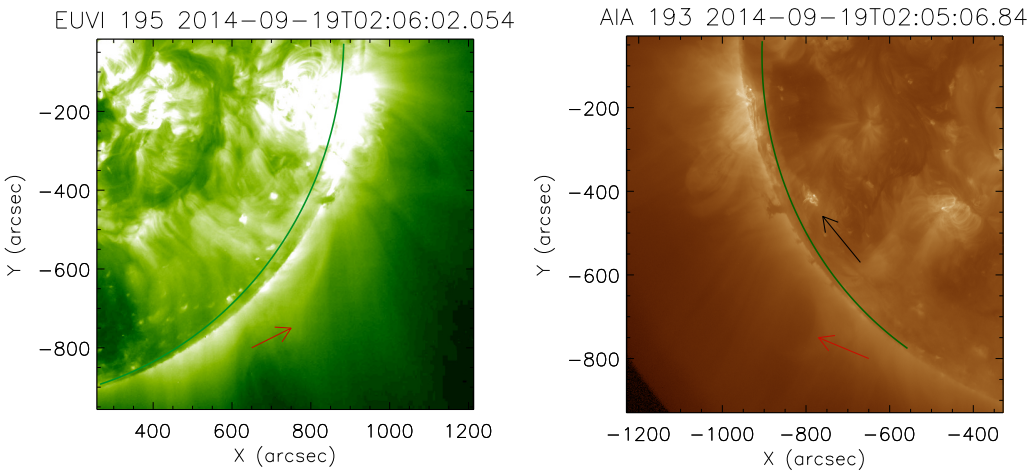

FIGURE 4.6: Left: STEREO/EUVI 195 Å image with the solar limb as seen from AIA 193 Å overplotted in green. Right: SDO/AIA 193 Å image with the limb as seen from EUVI 195 Å overplotted in green. The black arrow represents the location of the source region (foot point) of the jet. Since the source region is behind the limb as seen from EUVI, it is not seen in EUVI 195 Å image. The animations are available online as movies 3 and 4.

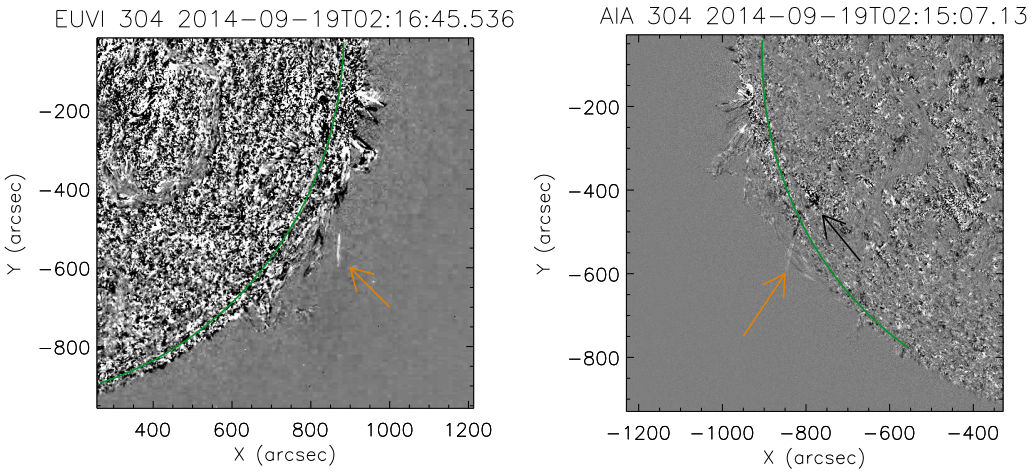

FIGURE 4.7: Left: STEREO/EUVI 304 Å difference image with the solar limb as seen from AIA 193 Å overplotted in green. Right: SDO/AIA 304 Å image with the limb as seen from EUVI 195 Å overplotted in green. The black arrow represents the location of the source region (footpoint) of jet. The orange arrow represents the jet in EUVI 304 Å and AIA 304 Å. The animations are available online as movies 5 and 6.

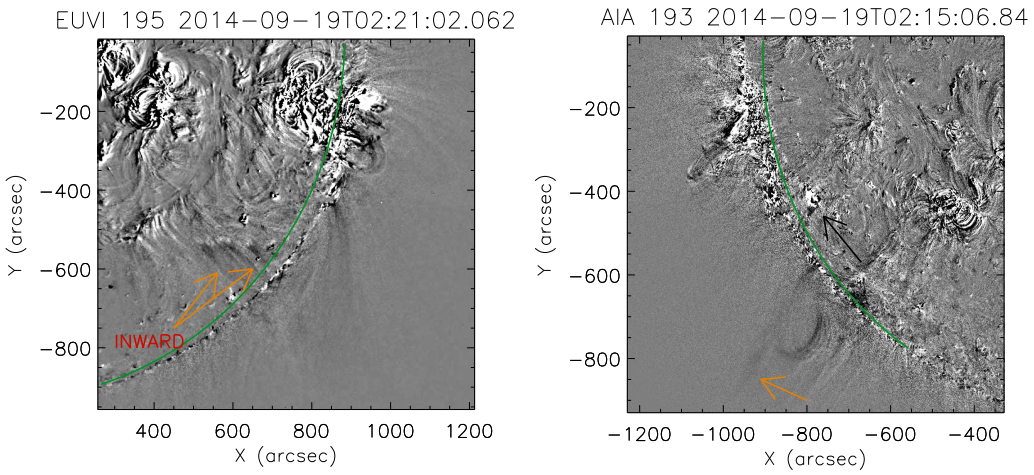

FIGURE 4.8: Left: STEREO/EUVI 195 Å difference image with the solar limb as seen from AIA 193 Å overplotted in green. Right: SDO/AIA 193 Å image with the limb as seen from EUVI 195 Å overplotted in green. The black arrow represents the location of the source region (footpoint) of the jet. The orange arrows represent the dark feature in EUVI 195 Å and AIA 193 Å.

4.4 Analysis of the jet

High-resolution images obtained from AIA/SDO enable us to resolve the jet and characterise its properties. Jets are often observed near coronal holes (Chandrashekhar *et al.* 2014). The appearance and dynamics of jets have been well studied because they contribute to coronal heating and solar wind acceleration (Chandrashekhar *et al.* 2014; Mueller and Antiochos 2008; Savcheva *et al.* 2007; Shibata *et al.* 1995).

The jet is seen in AIA 304 Å, 171 Å, 193 Å, 211 Å and to some extent in 94 Å. In AIA 304 and 171 Å, the jet is seen as a bright collimated plasma propagating outward while in hotter channels like AIA 211 Å and to some extent in 193 Å, we initially note bright collimated plasma, which becomes fainter at later times, followed by a dark emission that is most likely due to the heating of the plasma (see Figure 4.10). In 94 Å we see a faint emission that suggests that the jet is multithermal in nature, having both cool and hot components (see movie 7 and 8).

As explained above in AIA 211 Å and 193 Å, a dark feature seen in difference images is the manifestation of the dark emission seen in normal-intensity images. At the same location in AIA 94 Å a faint emission is seen that is the signature of heating (see Figure 4.9). The animations of difference images of AIA 211 Å and 94 Å are available online as movie 7 and 8, respectively. It is worth noting at this point that the dark feature seen in AIA 211 Å could either be the hot component of the jet, or it could be the signature of heating caused by the jet. However, low signal-to-noise ratio prevented us from finding the bright emission in 94 Å, but a faint emission is clearly seen in the difference images. The heating mechanism is beyond the scope of the present study.

We found that the jet is associated with a B9 class flare as recorded by GOES-15, whose peak is recorded at 02:13 UT. It may also be possible that the inward-moving dark features observed with STEREO/EUVI-B 195 Å are the faint EUV wavefront triggered by the jet (Liu and Ofman 2014) or that they are the result of jet material falling back to the solar surface (Culhane *et al.* 2007). We also estimate the temperature at the location of dark emission using the DEM technique developed by Aschwanden *et al.* (2013). We find at the location of dark emission seen in AIA 211 Å difference images that the temperature is hotter than in other regions. The right panel of Figure 4.10 shows the temperature map with contours of log(T)=6.3 overplotted, and the left panel shows the difference image of AIA 211 Å with contours of log(T)=6.3 overplotted in red. We note that the contours surround most of the dark emission seen in AIA 211 Å. We conjecture that the jet interacts with the loops, causing transverse oscillations, and it interacts with the ambient medium, transferring part of its energy and heating the local plasma. This heating causes plasma to disappear from the AIA 193 and 211 Å passbands, thus dark features appear in the hotter channel. When this heating shifts towards the far side, beyond the limb, we see it as a dark feature propagating inward in EUVI 195 Å. Moreover, as pointed out in Section 4.3.1, the propagating dark feature seen in EUVI 195 Å could be the jet plasma falling back towards the Sun.

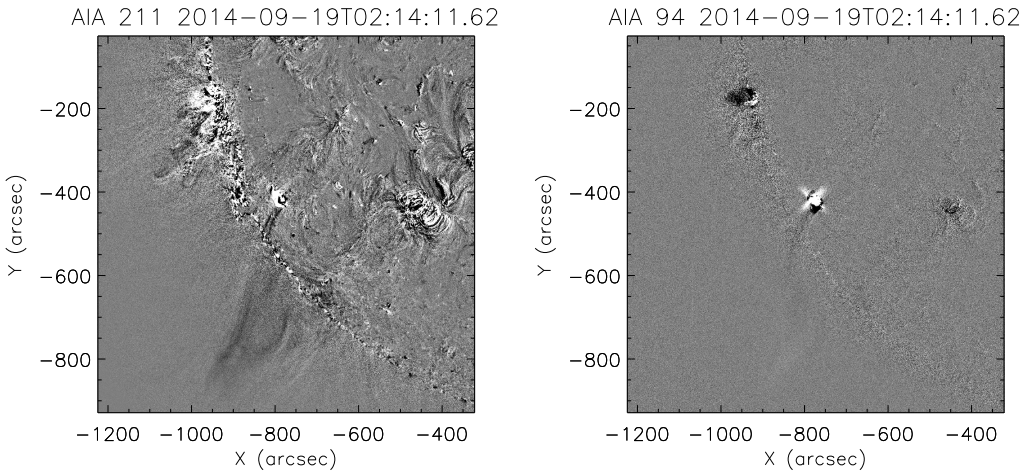

FIGURE 4.9: Left: SDO/AIA 211 Å difference image. A dark feature is visible near the loop. Right: SDO/AIA 94 Å image. A faint bright emission is visible near the loop. The animations are available online as movies 7 and 8.

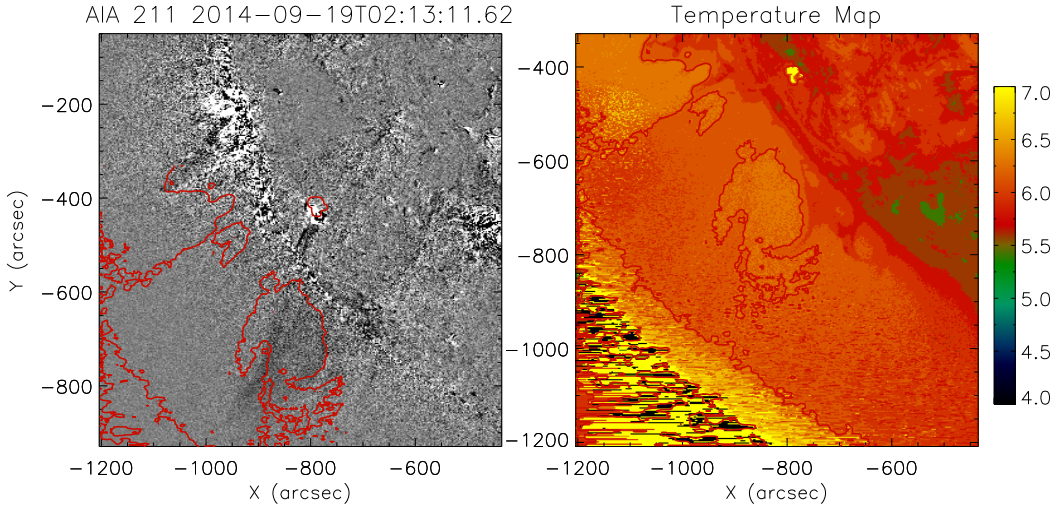

FIGURE 4.10: Left: SDO/AIA 211 Å difference image with contours of log(T)=6.3 (∼2 MK) overplotted. Right: Temperature map (note the difference in field of view). The colorbar on the right represents log(T).

We estimate the velocity of the jet by creating an x–t map. To generate the x–t map, we isolate the trajectory of the jet. We choose a few points along the path through which the jet propagates (starting from the time of jet eruption until the jet vanishes). Next, we interpolate a curve between these points using cubic spline fitting. We plot another curve, 50 pixels apart, parallel to it, so that the jet propagates within the region outlined by the two white curves as shown in the

left hand panel of Figure 4.11, in spite of the transverse displacement of the jet. The trajectory of the jet, marked with white curves, is shown in a movie available online (see movie 2). Finally, we average the intensity between the two curves and create the x–t map. The x–t map is shown in the right panel of Figure 4.11. The inclined ridge in the x–t map represents the jet propagating outward along the chosen curved artificial slice. We fit a straight line by eye estimation. The velocity of the jet is estimated by calculating the slope of the fitted line, which is found to be $\sim$43$\pm$4 km s^{-1}. We use the same analysis in the AIA 211 Å difference images and generate x–t map as shown in Figure 4.12. In this case, we choose a broad straight slice to ensure that both bright and dark features remain within the slit for the entire duration of the analysis. In the right panel of Figure 4.12, we see bright and dark ridges. The bright ridge corresponds to jet material and is estimated to be propagating with a speed of 63 km s^{-1}. The dark emission is estimated to be propagating with a speed of 168 km s^{-1}. This could either be the hot component of jet or the heating caused by jet eruption, which is propagating outward. However, the low signal-to-noise ratio in AIA 94 Å prevented us from making x–t maps of AIA 94 Å.

We also analyse the transverse oscillations in the jet as it propagates. Since the jet propagates while it oscillates, we place 40 artificial slices along the jet propagation axis to capture the transverse oscillations. This is done by joining 40 equidistant points of one of the curves to their corresponding parallel points at the other curve. This produces 40 transverse slits at 40 equidistant positions along the jet axis, as shown in Figure 4.13.

We create x–t maps for individual slices and add them. The resulting x–t map is shown in Figure 4.14. Since the jet becomes fainter as it propagates outward, the jet intensity decreases with time in the x–t maps. We find that both high and low periodicities are co-existent. The high-frequency signal is only present in a region close to the footpoint of the jet, however. We fit two sinusoidal curves in

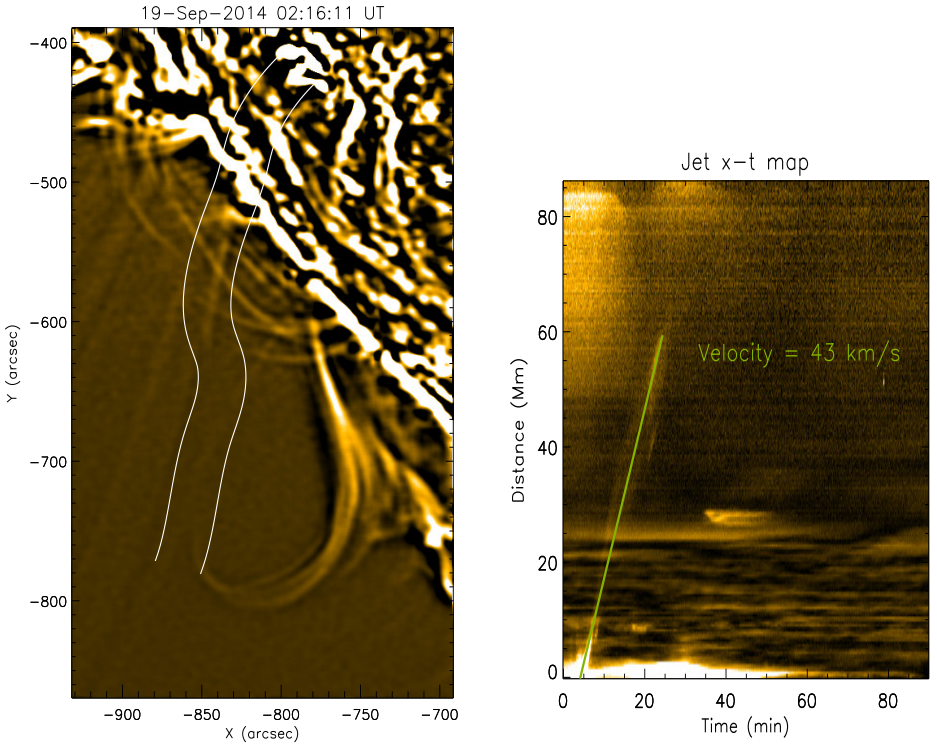

FIGURE 4.11: The left panel shows the region of jet propagation outlined by two parallel curves. The right panel represents the x–t map for the selected region (shown in the left panel). The fitted straight line is shown in green. The jet velocity is found to be ∼43±4 km s^{-1}. An animation is available online as movie 2.

Figure 4.14 shown as orange and green curves, and find a periodicity of 2 minutes and 24 minutes respectively. It is important to note that the time period of the jet oscillation (∼24 minutes) is nearly equal to the time period of the coronal loop oscillations (∼31 minutes).

4.5 MHD seismology

We assume the coronal loop to be a cylindrical magnetic flux tube of uniform magnetic field B_0, where the minor radius a, that is, the half-width of the coronal loop cross-section is, $\ll L$ (where L is the total length of the loop). This is called the thin-tube (TT) or long-wavelength approximation. Thus, $k_z a << 1$ (where

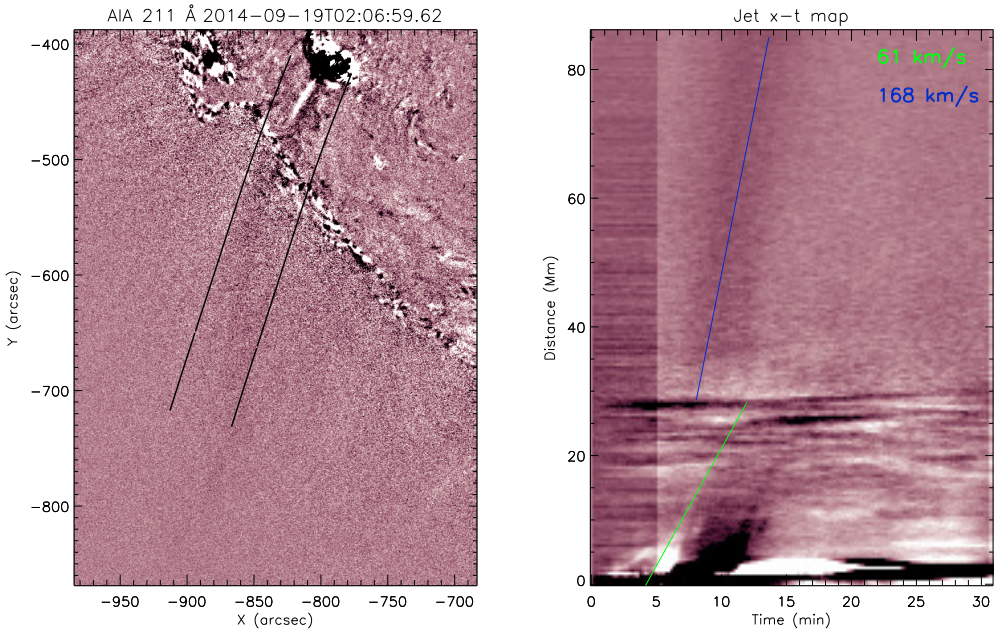

FIGURE 4.12: Left: SDO/AIA 211 Å difference image. The jet trajectory is outlined by two parallel lines. Right: x–t map for the selected region (shown in the left panel). Two features, a bright and a dark ridge, are fitted with green and blue lines, respectively.

$k_z = 2\pi/\lambda$ and $\lambda = 2L$ for the fundamental mode). In TT approximation, the phase speed V_{ph} is the same as the kink speed C_K (Nakariakov and Verwichte 2005) :

$$V_{ph} = C_K = \frac{2L}{P} \ , \tag{4.2}$$

where C_K is also defined as the density-averaged Alfvén speed (Edwin and Roberts 1983), *i.e.* :

$$C_K = \sqrt{\frac{\rho_0 C_{A0}^2 + \rho_e C_{Ae}^2}{\rho_0 + \rho_e}} \ , \tag{4.3}$$

where ρ_0 and ρ_e are the density of uniform plasma inside and outside the loop, respectively, and C_{A0} and C_{Ae} are the internal and external Alfvén speeds, which can be defined as

$$C_{A0} = B_0/\sqrt{\mu_0 \rho_0} \ , \tag{4.4}$$

$$C_{Ae} = B_e/\sqrt{\mu_0 \rho_e} \ , \tag{4.5}$$

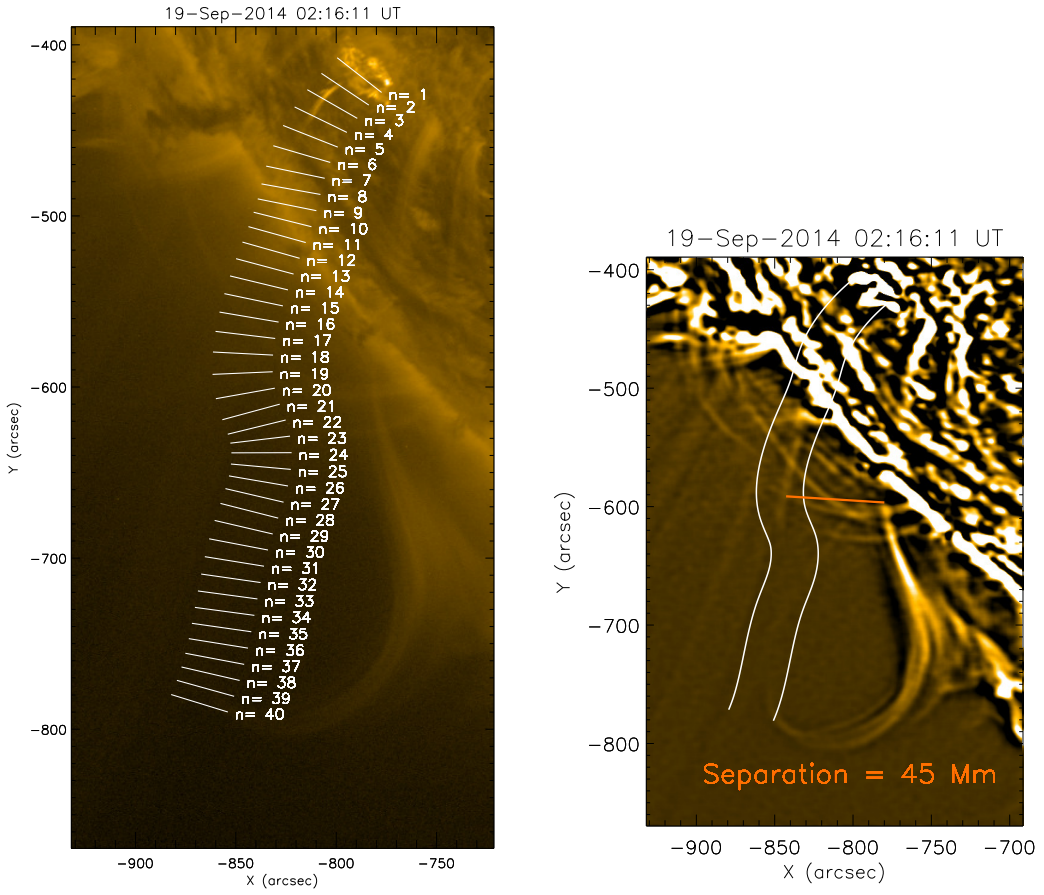

FIGURE 4.13: Left: The figure shows 40 transverse slits at 40 equidistant points along the jet propagation axis. Right: Figure showing the separation between the oscillating jet and the coronal loop.

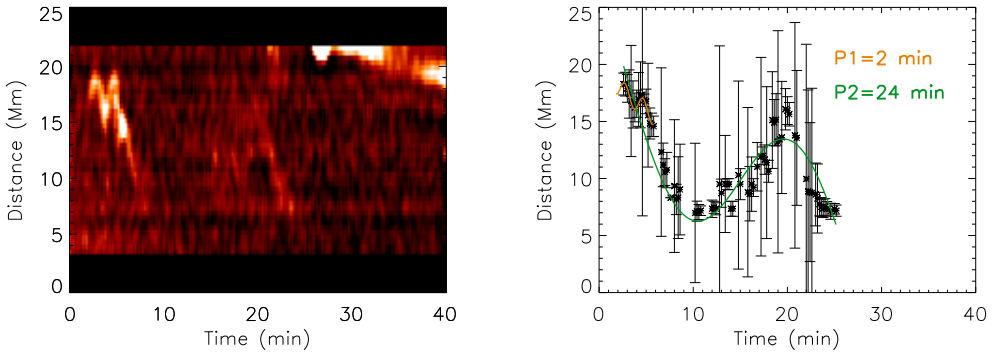

FIGURE 4.14: Left: x–t map obtained after adding all artificial slices as shown in Figure 4.13. Right: Orange and green curves represent the best-fit sinusoidal curves. Corresponding periods are mentioned in the figure.

where B_0 and B_e are the internal and external magnetic fields, respectively, for the coronal loop.

Substituting Equations (4.4) and (4.5) into Equation (4.3), and assuming that the internal and external magnetic fields of the loop are equal, we obtain

$$C_{A0} = \frac{C_K}{\sqrt{\frac{2}{1+\frac{\rho_e}{\rho_0}}}} \ , \tag{4.6}$$

Using Equation (4.2), we estimate the kink speed (C_K) to be ∼392±17 km s^{-1} (and ∼560±38 km s^{-1}, assuming coronal loop to be semicircle) and the internal Alfvén velocity ∼299±27 km s^{-1} (and ∼415±28 km s^{-1}, assuming the coronal loop to be a semicircle), assuming a density contrast $\left(\frac{\rho_e}{\rho_0}\right) = 0.1$. It is worth noting at this point that the density contrast depends on the EUV intensity ratio as $\left(\frac{\rho_e}{\rho_0}\right)^2 = \frac{I_e}{I_o}$, where I_e and I_o are EUV intensity of the background and inside the loop, respectively. However, it should be noted that this is a rough estimate since the column depths of loop and background are not same. We find that the intensity ratio along the loop changes from loop footpoint to the loop top. Furthermore, we also note that the intensity ratio at a given position along the coronal loop changes as it oscillates, presumably as a result of variations in the column depth of the loop along the line of sight by the wave (Cooper *et al.* 2003). We estimate the intensity ratio at several places along the loop and at different times. We find that the intensity ratio varies from 0.18 to 0.5. Thus the density contrast varies from 0.4 to 0.7. We use AIA 171 Å for the analysis because the loop is best visible in this wavelength. However, it is important to note that the intensity contrast of the loop also depends on its orientation thus the density contrast may still be a rough estimate. Table 4.1 shows the estimation of the Alfvén speed and the magnetic field strength for different values of the density contrast (*i.e.* 0.1, 0.4, and 0.7). We keep 0.1 for comparison since this is a typical value which is used in most studies. Using Equation (4.4) and taking $\mu_0 = 4\pi \times 10^{-7}$ H m^{-1} (in SI units), we can estimate the magnetic field inside the coronal loop (B_0), provided

TABLE 4.1: Estimation of Alfvén speed and magnetic field strength inside the coronal loop.

	Projected Length			Semicircular Model		
$\frac{\rho_e}{\rho_0}$	0.1	0.4	0.7	0.1	0.4	0.7
C_{A0} (km s^{-1})	299 ± 27	328 ± 14	361 ± 16	415 ± 28	469 ± 32	516 ± 35
B (G)	2.68±0.64	2.86±0.12	3.20±0.14	3.62±0.24	4.1±0.28	4.5±0.31

the internal density of the coronal loop is known.

4.5.1 Density estimate using DEM analysis

To calculate the internal density of the coronal loop, we use the differential emission measure (DEM) analysis technique developed by Aschwanden *et al.* (2013). Using this automated technique we obtain that the number density of the electrons (n_e) is $10^{8.56\pm0.17}$ cm^{-3} and the average temperature is $10^{5.79\pm0.21}$ K (see Figure 4.15).

4.5.2 Calculation of the magnetic field inside the coronal loop

Estimating the electron density using DEM and assuming H:He=10:1, we obtain the magnetic field strength inside the coronal loop for different values of density contrast using Equations (4.4) and (4.6) (see Table 4.1). The estimated value of the magnetic field inside the loop is lower than in active-region loops.

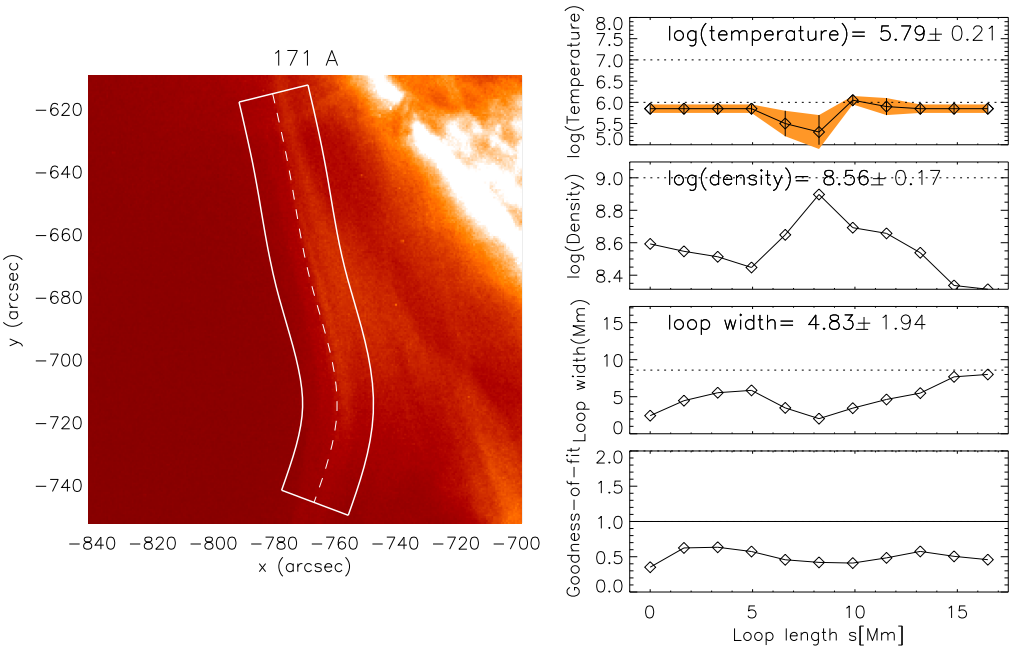

FIGURE 4.15: The left panel shows the location of the loop, enclosed in curves, that we selected for analysis. The best-fit values of the DEM peak temperature, the electron densities, loop widths, and the goodness-of-fit χ^2 for the 171 Å, Gaussian DEM fits, are shown in the right panel of the graph.

4.6 Energy estimates

To understand whether the jet can trigger the transverse oscillations in the coronal loop, we calculate the energy density of the jet and compare it with the energy density of the oscillating coronal loop. Although both transverse oscillations and linear motion contribute to the energy density of the jet, we estimate energy density of the jet due to only linear motion. Moreover, we estimate energy density using the bright feature of the jet. We do not consider the energy density of the hot jet component since it is very difficult to measure its density and thus its energy density. Therefore, it should be borne in mind that the energy density of the jet is an underestimate of the total energy density. It should be noted that comparison of total energy will be meaningful but since we do not have an estimate of the volume of plasma, we compare the energy densities of these two structures. The

energy density of the propagating jet due to its linear motion is defined as

$$E_{jet} = \frac{1}{2}\rho_{jet}v^2 \ , \tag{4.7}$$

where ρ_{jet} is the density of the jet. The typical value of the number density of the jet is reported to be between 10^9 cm^{-3} (Shimojo and Shibata 2000) to 10^{10} cm^{-3}, (Madjarska 2011; Moreno-Insertis and Galsgaard 2013).
We also estimate the number density of the jet using DEM at the instant when it is clearly observed. The density is estimated to be $10^{9.92}$ cm^{-3}. v is the velocity of the jet which is found to be $\sim$43$\pm$4 km s^{-1} (see Section 4.4). Using $n_{jet} = 10^{10}$ cm^{-3} and the jet velocity, we estimate the energy density to be $(19.6 \pm 3.6) \times 10^{-3}$ J m^{-3}.

The energy density of the oscillating loop is defined as (Goossens *et al.* 2013)

$$E_{monolithic} = \frac{1}{4}\rho_0\omega^2{A_0}^2 \ , \tag{4.8}$$

where ρ_0 is the internal density of the coronal loop. Using DEM we estimate the number density inside the loop to be $10^{8.56\pm0.17}$ cm^{-3}. ω is the angular frequency of the oscillating loop ($\omega = kC_K = \frac{\pi}{L}C_K$, where $k = \frac{2\pi}{\lambda}$ and $\lambda = 2L$ for the fundamental vibration mode). Thus, $\omega = (3.36 \pm 0.36) \times 10^{-3}$ s^{-1} (and $3.27\pm0.19\times10^{-3}s^{-1}$ assuming the loop to be a semicircle) using the parameters estimated in Section 4.5.2. A_0 is the displacement amplitude.

The displacement amplitude for n=4 slice is $\sim$4.50$\pm$1.72 Mm, which is the largest of all the slices (see Figure 4.4). We estimate that the energy density of the loop corresponding to this amplitude is $\sim (3.28 \pm 0.89) \times 10^{-5}$J m^{-3} ($\sim (3.26 \pm 0.23) \times 10^{-5}$J m^{-3} assuming the loop to be a semicircle). For n=7 slice, the displacement amplitude is $\sim 2.75 \pm 0.22$ Mm, which is the smallest of all the slices, the energy density is estimated to be $\sim (1.23\pm0.09)\times10^{-5}$ J m^{-3} ($\sim (1.22\pm0.1)\times10^{-5}$ J m^{-3} assuming the loop to be a semicircle). Therefore, the energy density of the oscillating loop is within the range from $(1.22 - 3.28) \times 10^{-5}$ J m^{-3}.

Since the coronal loop is not monolithic and consists of many fine loops, we estimate the energy density using a multistranded loop model. The energy density in the multistranded oscillating coronal loop is given by

$$E_{multistrand} = \frac{1}{2} f(\rho_0 + \rho_e)\omega^2 {A_0}^2 \ , \tag{4.9}$$

where ρ_e is the external density of the coronal loop. f is the filling factor, which is defined as the ratio of the sum of the volume of an individual flux tube ensemble together with the total volume containing flux tubes. Using Equations (4.8) and (4.9), we obtain

$$\frac{E_{multistrand}}{E_{monolithic}} = 2f(1 + \frac{\rho_e}{\rho_o}) \ . \tag{4.10}$$

We calculate the filling factor f, as defined above at several instances along the length of coronal loop. The mean and standard deviation is estimated. Therefore, f is found to be 0.17 ± 0.03. Substituting the value of f in Equation (4.10), we find that $E_{multistrand} = 0.434\ E_{monolithic}$ for the density constrast of 0.1. $E_{multistrand} = 0.476\ E_{monolithic}$ and $E_{multistrand} = 0.578\ E_{monolithic}$ assuming the density contrast to be 0.4 and 0.7, respectively. Therefore, we find that the energy density of the jet is much greater than the energy density of the coronal loop. The jet might be transferring a part of its energy to displace the loop. Hence, the jet can be inferred to be the cause of the transverse oscillations in the coronal loop.

4.7 Interaction between jet and loop

In Section 4.6, we found that the jet has enough energy to excite oscillations in the coronal loop. In running difference movies of AIA 211 Å (see movie 7) we find evidence of hot and cool components of a jet that hits the coronal loop. This could be a simple projection effect, but we do not know which trajectory the jet

follows: maybe it curves, hits the loops and some part of the jet plasma is seen as the inward-moving feature in STEREO/EUVI 195 Å.

Furthermore, a collective transverse oscillation in two flux tubes is also possible. The magnetic field of the jet spine constitutes a flux tube that includes flowing plasma and is subject to long-period (24 minutes) transverse oscillations. The coronal loop is another flux tube that originally is in equilibrium in the vicinity of the jet plasma column. The separation between the oscillating jet and the coronal loop is estimated to be ∼45 Mm, as shown in Figure 4.13 (right panel). Luna *et al.* (2008) studied the collective kink oscillations of two identical parallel magnetic flux tubes. They found that there are four oscillations mode in such a system in which two are in-phase oscillations. Later, Van Doorsselaere *et al.* (2008) reported that the kink oscillations of the system of two non-identical tubes is degenerate. They found that similarly to the kink oscillations of a single tube with circular cross-section, there is no preferable direction of the kink oscillation polarization, and the two long-period (and also short-period) oscillations merge with each other to form two oscillatory modes (one with a long period, and another with a short period).

Significant developments have also been made considering the various models demonstrating the damping of the kink oscillations in multiple magnetic flux-tubes (Luna *et al.* 2009, 2010; Ofman 2009; Terradas *et al.* 2008). The linear theory of the resonant damping of kink oscillations in two parallel magnetic tubes is also developed by Robertson and Ruderman (2011). It should be noted that the observed jet shows transverse kink oscillations of two periods : 24 minutes (long) and 2 minutes (short) (Figure 4.14). The loop in the vicinity also exhibits similar transverse oscillations, although only a long period (31 minutes) is detectable in the observational base line. Moreover, the long-period kink waves in both flux systems are almost out of phase. Moreover, we do not know that at which location and time the jet interacts with the loop. It may not be necessary that the visible

jet material has to strike the loop. Both the jet and coronal loop are magnetic flux tubes, thus the interaction between them may occur earlier than the observational signatures it produces. If the jet interacted with the loop and triggered oscillations before the bright visible material reached the same location, in that scenario, at the instant when bright material will appear adjacent to coronal loop both systems might go out of phase. Both flux tubes, *i.e.*, the upper magnetoplasma column of the jet and the part of the coronal loop in its vicinity (45 Mm apart), are non-identical flux tubes as their plasma and magnetic field properties are essentially not the same. It is worth noting at this point that this distance is projected in the plane of sky and therefore is an underestimate of the real distance which could be higher. Therefore, the model of Van Doorsselaere *et al.* (2008) might be at work in the present observational base-line where the transverse oscillations of the short period (2 minutes) and the long period (21 minutes) both are excited in the jet (Figure 4.14). The two modes with the longer period are most likely merged in one degenerate mode, and the same occurred with the two modes with the shorter period. Since the modes from each pair are polarized in the mutually orthogonal directions (Figure 4.14), the degenerate modes created by merging of two modes can be arbitrarily polarized. The long-period mode is only detected in the coronal loop tube, while the short period is not detected. The reason may be that plane-of-loop apex is in such an orientation that the arbitrarily set polarization direction of the short-period oscillations (which is seen in the jet body) is non-identifiable.

4.8 Conclusions

We reported large amplitude and long-period transverse oscillations in a coronal loop that have most likely been triggered by a nearby oscillating jet. We find that the jet appears as a bright feature in all AIA channels, but soon disappears from hot channels like 211 Å. A faint emission is also seen in AIA 211 Å, which

is considered a signature of heating. We estimate the length of the loop by two different methods. (i) Calculating the projected distance of the loop in the plane of sky, which can be considered as the lower limit of the loop length and (ii) estimating the loop length by assuming a semicircular geometry, which can be considered as the upper limit of the length of the loop. Based on this, we estimate the lower (upper) limit of the kink speed and the Alfvén speed to be $\sim$392$\pm$17 (560$\pm$38) km s^{-1} and $\sim$299$\pm$27 (516$\pm$35) km s^{-1}. We use the seismic inversion technique to estimate the magnetic field strength inside the coronal loop. We estimate the lower (upper) limit of the strength of the magnetic field inside coronal loop to be $\sim$2.68$\pm$0.64 (4.5$\pm$0.31) G, which is lower than a typical value of the magnetic field inside a coronal loop. The reason might be that it is not an active-region coronal loop. Finally, we estimate the energy density of loop. We find that the energy density varies from 1.22×10^{-5} J m^{-3} to 3.28×10^{-5} J m^{-3}, which is about two to three orders of magnitude lower than the energy density of the jet ($\sim(19.6\pm3.6)\times10^{-3}$ J m^{-3}). We therefore conclude that the energy stored in the jet is found to be enough to excite oscillations in the coronal loop. The present observations also support the model of the collective transverse oscillations of two non-identical magnetic flux tubes in which long- and short-period modes are excited with arbitrary polarization direction (Van Doorsselaere *et al.* 2008).

Chapter 5

First Imaging Observation of Standing Slow Wave in Coronal Fan loops[†]

5.1 Introduction

Magnetohydrodynamic (MHD) waves are ubiquitous in the solar corona. With the advent of modern space-based instruments, different types of wave modes have been observed in the past decade. Slow MHD modes (compressional waves) were first observed in the polar coronal holes using Ultraviolet Coronagraph Spectrometer (UVCS) by Ofman *et al.* (1997). Later, Deforest and Gurman (1998) and Ofman *et al.* (1999) reported propagating intensity disturbances (PDs) in polar plumes using Extreme-ultraviolet Imaging telescope (EIT) onboard Solar and

[†]Results of this work are published in Pant *et al.* (2017).

All the animations that are referred to in this chapter are available at `http://dx.doi.org/10.3847/2041-8213/aa880f`.

Heliospheric Observatory (SOHO). Recently, several authors have reported that small-scale jets and spicules at the transition region and chromosphere are associated with PDs seen in polar plumes and polar coronal holes (Pant *et al.* 2015; Jiao *et al.* 2015; Samanta *et al.* 2015; Bryans *et al.* 2016; Yuan *et al.* 2016). Reflections of propagating slow waves were also reported in hot and flaring coronal loops using Atmospheric Imaging assembly (AIA; Kumar *et al.* 2013, 2015) and X-ray telescope (XRT) (Mandal *et al.* 2016) observations. The authors have reported that these waves are triggered by the flares at the footpoint of the coronal loops. Recently, Fang *et al.* (2015) have modelled the reflective slow mode in flaring loops using 2.5D MHD simulations in synthetic 131 Å emission images.

Apart from propagating slow waves, flare-excited standing slow waves have also been observed in hot and flaring coronal loops. Oscillations in Doppler velocity, detected in Fe XIX, were reported in hot flaring coronal loops using SUMER/-SOHO and SXT/Yokoh (Wang *et al.* 2002). The time period of oscillations was found to be 14–18 minutes. These oscillations were interpreted as slow standing modes. Wang *et al.* (2003a,b) have performed statistical studies of slow standing modes in several hot coronal loops and post-flare loops, respectively. They have reported a $\pi/2$ phase shift between Doppler velocities and line intensities of Fe XIX and Fe XXI emission lines (formation T $>$ 6 MK) which is the signature of a standing slow mode (see also Wang 2011; Yuan *et al.* 2015).

The standing slow modes are believed to be triggered by an impulsive flare, which causes asymmetric heating at one footpoint of the coronal loop (Wang *et al.* 2005). However, Tsiklauri *et al.* (2004) performed a numerical study of the longitudinal oscillations and reported that the excitation of standing oscillations is independent of the location of the impulsive heating in the loop. Taroyan *et al.* (2005, 2007) have performed 1D hydrodynamic simulations of standing slow modes and showed that slow standing waves can be triggered by impulsive footpoint heating as well. Taroyan *et al.* (2007) and Taroyan and Bradshaw (2008) have constructed a 1D hydrodynamic loop model to study and distinguish between standing and

propagating slow oscillations in hot and cool coronal loops. They have reported that the phase of the intensity of the oscillation continuously changes with time due to heating and cooling of loops. Yuan *et al.* (2015) have performed forward modelling of standing slow modes in hot flaring coronal loops (T > 6 MK) and studied their imaging and spectroscopic signatures. The authors have reported that the amplitude of the oscillations along the loop should vary depending on the mode of the oscillations.

Slow standing waves are found to be strongly damped. Ofman and Wang (2002) used a 1D MHD model to study damped standing slow oscillations. The strong damping was attributed to large thermal conduction that depends on the temperature of the loops. Recently, Wang *et al.* (2015) observed standing slow modes in hot coronal loops using AIA 94 Å observations and reported that the thermal conduction, which is believed to damp the standing oscillations, is suppressed in hot coronal loops. Until today, standing slow modes have been observed exclusively in hot coronal loops. A very limited number of standing slow mode waves were detected by imaging observations. In this chapter, we report the evidence of standing slow waves in cool fan loops. The chapter is organised as follows. In Section 5.2, we describe the data processing used for this study. In Section 5.3, we describe the method of analysis, which is followed by a discussion and conclusions in Section 5.4

5.2 Observations

On 2012 March 7, a group of fan loops were observed near the active region AR 11428 (see Figure 5.1). Two X-class flares were detected consecutively at a distant active region, AR 11429 to the northwest of AR 11428. The approximate distance between AR 11428 and AR 11429 is about 455 Mm. The Geostationary Operational Environmental Satellite (GOES) X-ray emission (inset in Figure 5.1) exhibits the evolution of the flares. The X-ray flux at two channels peaked at 00:22 UT and 01:13 UT, respectively. The strength of two peaks corresponds to the fluxes of X5 and X1 classes, respectively. Both the X5 and X1 flares originated from AR 11429 and the associated energy pulses reach AR 11428 at 00:27 UT and 01:15 UT, respectively. The fan loops were initially driven to move transversely, and subsequently, the intensity perturbations along the loops became detectable. A three-hour data set (00:00 UT–03:00 UT) taken by the AIA on board the Solar Dynamics Observatory (SDO; Lemen *et al.* 2012b) was used for detailed analysis. The fan loops of interest are visible in both 171 and 193 Å, so we only use these two channels for study.

5.3 Results

5.3.1 Time evolution of intensity oscillations

To derive the properties of the oscillations, we placed three artificial slices, S1, S2, and S3, along the fan loops as shown in Figure 5.2, at the locations where the intensity oscillations were clearly seen. We chose broad artificial slices in order to capture the longitudinal oscillations despite that they get displaced in the transverse direction due to interaction with the blast wave. It should be

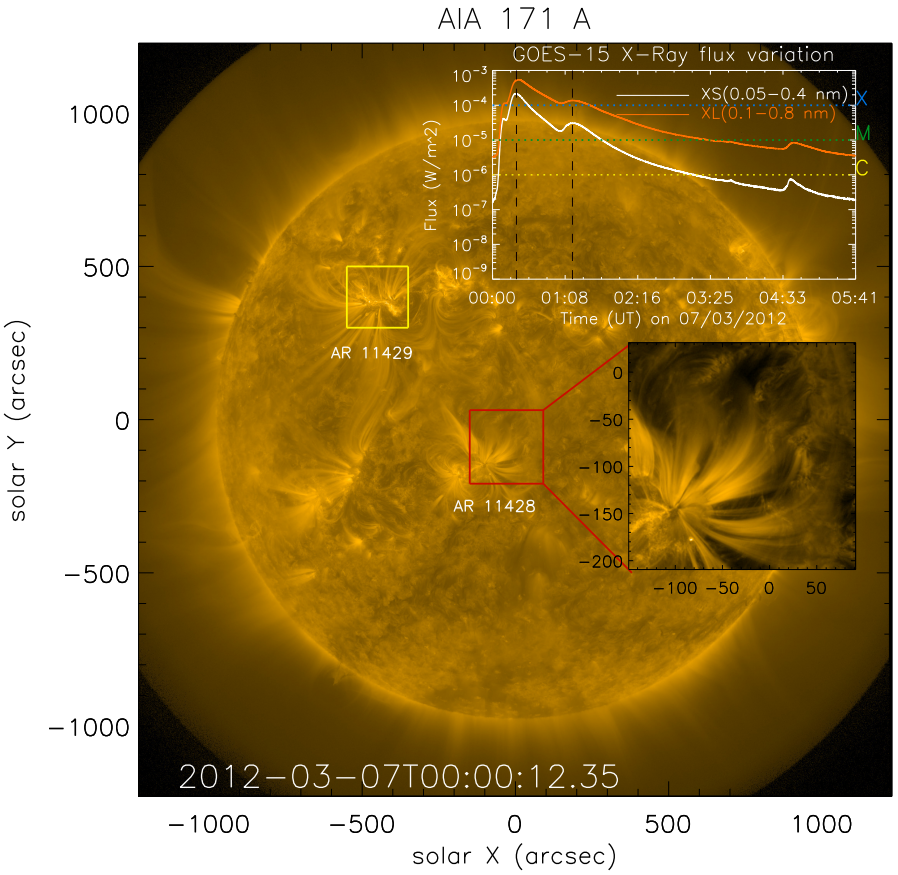

FIGURE 5.1: Full disk image of the Sun at AIA 171 Å. Red and yellow boxes represent the location of active regions AR 11428 and11429 respectively. Region of interest (ROI) that is used for further analysis is enclosed in the red box. GOES X-ray flux variation is overplotted in the figure. Curves in orange and white represent the flux corresponding to two passbands, *i.e,* 0.1–0.8 nm and 0.05–0.4 nm, respectively. Two vertical dashed lines in black represent the timings of the peak of the GOES X-ray flux relevant for this study.

worth noting at this point that only one footpoint, close to the active region, of fan loops was clearly visible in 171 and 193 Å. The length of the artificial slices correspond to the distances along the fan loop up to which clear signatures of intensity oscillations were observed. Therefore, the length of the artificial slices may not be equal to the length of the fan loops. We discuss the estimation of the length of the fan loop in Section 5.3.3. For each of the three artificial slices, we generated a time–distance map, which henceforth will be termed as an x–t map throughout this chapter. Figure 5.3 represents the x–t maps for slices S1, S2, and S3 for 171 and 193 Å in the left, middle, and right panels, respectively.

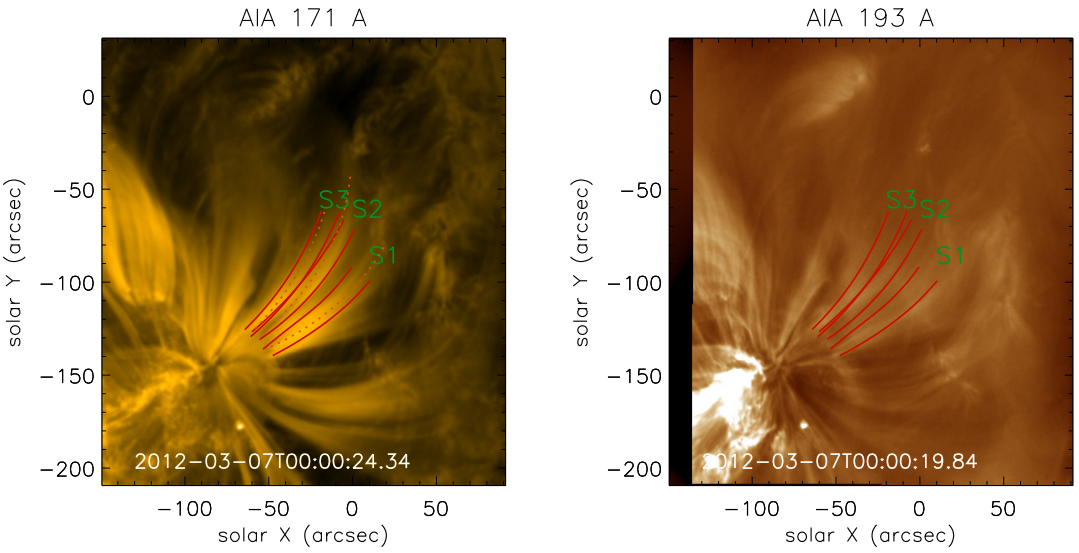

FIGURE 5.2: *Left*: AIA 171 Å image of the ROI shown in Figure 5.1. Three curved artificial broad slices, S1, S2 and S3 are overplotted in red which were used to generate the x-t maps shown in Figure 5.3. The dotted curves in orange represent the length of the fan loops. *Right*: same as left panel, but for AIA 193 Å. Animations corresponding to AIA 171 and 193 Å are available.

The signatures of intensity oscillations were clearer in AIA 171 Å as compared to AIA 193 Å, because fan loops appeared more diffuse in AIA 193 Å. A possible reason for this is discussed in Section 5.3.4. The red vertical lines in Figure 5.3 represent the instances when blast waves hit the fan loop system. We noticed that the second blast wave hit fan loops when the intensity oscillations driven by the first blast wave were still present.

Figure 5.3 shows that the intensity oscillations were out of phase at the two ends of the artificial slices as seen in the x–t maps. The out-of-phase signature was clearly seen in both AIA 171 and 193 Å. It is clear from the Figure 5.3 that one reflection point (or antinode) of the oscillations was present near the one footpoint that is clearly visible in the intensity images, while the other antinode was present at the other end of the artificial slice, which may or may not be close to the other footpoint. From the animations of Figure 5.2, it is evident that the shape and appearance of the fan loops was changed after the second blast wave hit the fan loop system. Therefore, intensity oscillations were not clearly seen in x–t maps

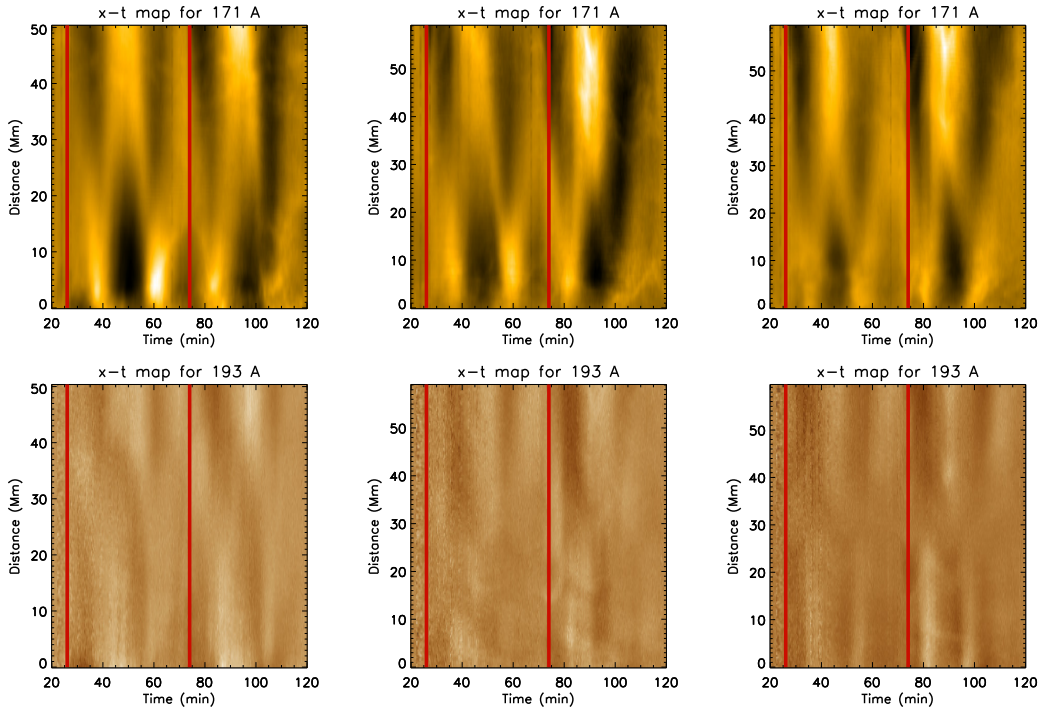

FIGURE 5.3: Time–distance (x–t) maps corresponding to slices S1, S2, and S3 as marked in Figure 5.2 are shown in the left, middle, and right panels, respectively. Two vertical red lines represent the time at which two blast waves impacted the fan loop system. The Y-axis represents the distance along the artificial slice.

after the second blast wave hit the fan loops.

Figure 5.4 shows the variation of intensity with time at different distances along the artificial slice S1. The Y-axis represents the relative intensity normalized to the local background. The two dashed vertical lines in red represent the instant of time when the blast wave hit fan loops. Since the blast wave hit the fan loops twice, we fitted the sinusoidal and damped sinusoidal curve separately at two different time intervals. The red curve represents the best-fit sinusoidal curve. We should point out that the damping of the oscillations were not seen clearly during the first period of observation, which may be due to the impact of the second blast wave. Thus, we did not fit a damped sinusoidal curve during the first time interval. However, we fitted a damped sinusoidal curve (shown in orange) in the second time interval and noticed the signature of damping at some locations along the fan loops (*e.g,* at 5 Mm). The intensity of oscillations became undetectable

after 120 minutes because the shape and appearance of the fan loop changed (see animations of Figure 5.2). The estimated average period of the oscillation, P, and average damping times, τ, at the location of three slices, S1, S2 and S3 in 171 and 193 Å are listed in Table 5.1. Since only one oscillation was observed during the second interval, there were large uncertainties in the damping time. The quality factor (ratio of damping time by time period) estimated at the location of three slices is also listed in Table 5.1. These oscillations are weakly damped as compared to those reported earlier in hot coronal loops. A possible reason for weak damping is outlined in Section 5.4.

5.3.2 Variation of amplitude of intensity oscillation

We noted that the relative amplitude (after normalising with background intensity) of the intensity oscillations along S1 in 171 Å first decreased and then increased while moving from one end at S1 (close to one footpoint) to other (may be close to another footpoint; see Figure 5.4). The variation can be seen clearly for both curves fitted at two separate time intervals shown in red and orange. Furthermore, the variation of the amplitude at different distances along S1, S2 and S3 in 171 and 193 Å is also shown in Figure 5.4. Systemic decrease and increase of the amplitude of oscillations, while moving from one end of the slice to another, was seen at the location of all slices. This signature clearly indicates the existence of an antinode near the footpoints of the fan loop.

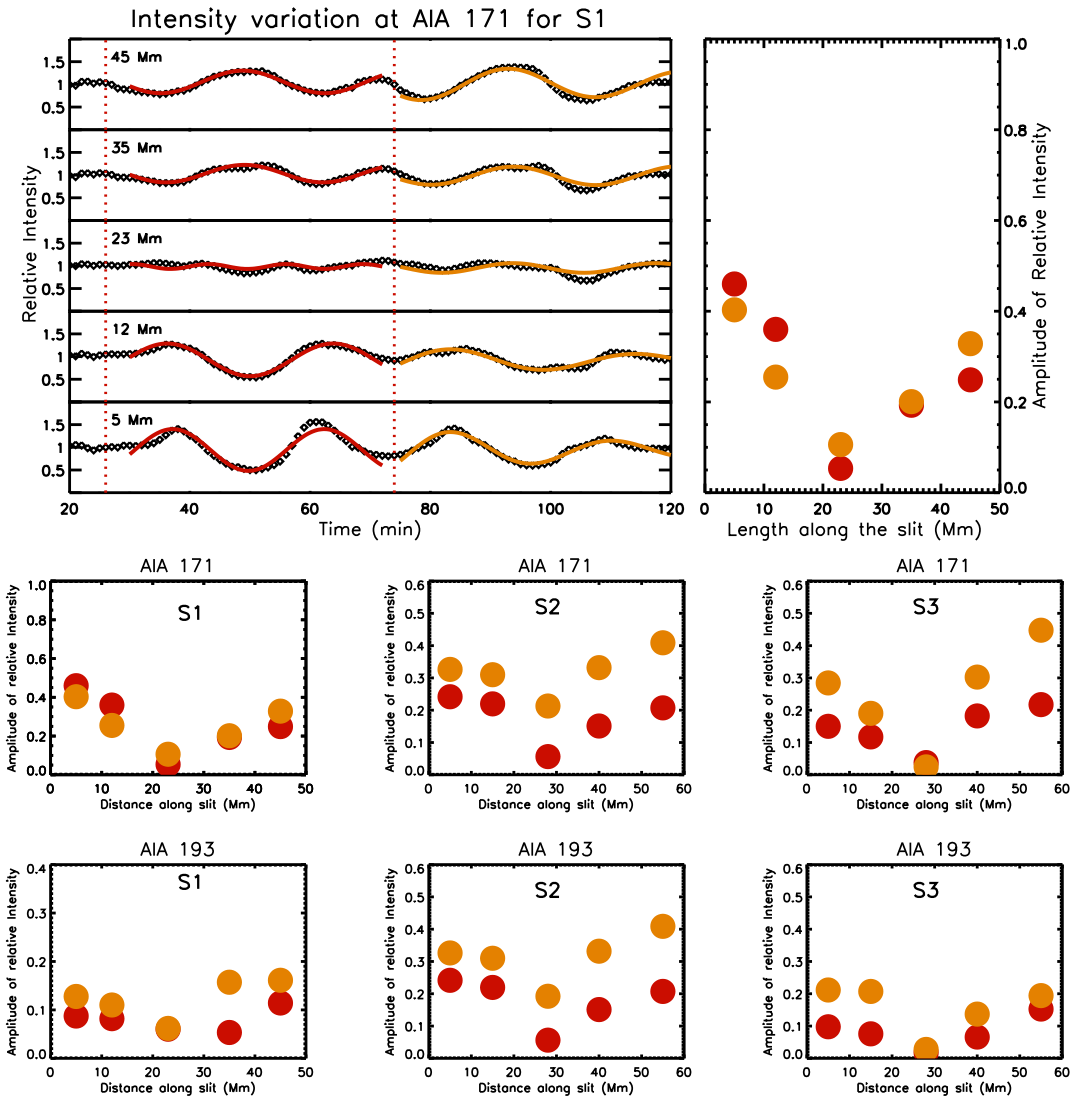

FIGURE 5.4: Top left: intensity variation after normalising to the background intensity, at different distances along S1. Two vertical dashed lines represent the instances when the blast wave hit the fan loops system. Middle and bottom: variation of the amplitude of intensity oscillations for S1, S2, and S3 in 171 and 193 Å. Top right: same as middle left panel.

5.3.3 Estimation of loop length and velocity of the oscillations

The footpoint of the fan loop that was away from the active region was distributed, and therefore not seen clearly in normal-intensity images of 171 or 193 Å. Thus,

it was not straightforward to measure the length of the fan loops. Moreover, the shape and appearance of fan loops also changed with time (see animations of Figure 5.2). To estimate the length, we chose the frames where the fan loops were best seen in normal-intensity images. We chose several points along the visible segment of the fan loops and interpolated a cubic spline between them. The length of the interpolated curve should be approximately equal to the projected length of the fan loops. The orange curves in Figure 5.2 are the fitted spline curves that represent the projected length of fan loops at the locations of three artificial slices. We found the length of the fan loops at the location of S1, S2, and S3 to be 62, 74, and 54 Mm, respectively (see Table 5.1). Note that the estimated length is the projected length in the plane of sky. Assuming the length of the fan loop is the same in 171 and 193 Å, we estimated the phase velocity of oscillations projected in the plane of sky in 171 (193) Å to be 75 (85), 83 (101), and 65 (91) km s^{-1} at the locations of S1, S2, and S3, respectively. The phase velocity of oscillations, v, are comparable to the speed of sound in 171 and 193 Å taking into account the projection effects.

5.3.4 Temperature and density of the fan loop

We estimated the temperature and density of the fan loop using the automated differential emission measure (DEM) technique as developed by Aschwanden *et al.* (2013). The temperature of the fan loops was found to be ∼0.7 MK which is much cooler than the hot loops as observed by hot SUMER lines (Wang *et al.* 2002) and in the AIA 94 Å channel (Wang *et al.* 2015). We also observed that the electron density decreased along the loop. Since the temperature of fan loops is low, they appear brighter in the 171 Å channel and diffuse in hotter channels like 193 Å. We should point out that a fan loop may consists of several finer strands and we have not considered that scenario here.

TABLE 5.1: Observational Parameters of Oscillations

	AIA 171 Å					AIA 193 Å				
Slice	P (minutes)	τ (minutes)	Q	l (Mm)	v (km s^{-1})	P (minutes)	τ (minutes)	Q	l (Mm)	v (km s^{-1})
S1	27.5±1.8	40±25	1.45	62	75	24.1±5.4	37±18	0.81	62	85
S2	29.6±3.8	53±25	1.79	74	83	24.4±4.6	20±10	1.53	74	101
S3	27.6±4.7	42±20	1.52	54	65	19.7±1.7	42±12	1.72	54	91

P represents the period of oscillations, τ represents the damping time, Q is the quality factor, defined as the ratio of damping time and period of oscillations, l is the projected length of the fan loop at the location of the slice and v is the velocity of the oscillations.

5.4 Discussion and Conclusions

We observe intensity oscillations in a non-flaring fan loop system as seen in AIA 171 and 193 Å images. The intensity variations were out of phase close to two footpoints of fan loops, and the amplitude of the intensity oscillations varied along fan loops at the location of artificial slices. The amplitude of intensity oscillations first decreased and then increased while moving from one footpoint to another along the fan loop. It should be noted that it is difficult to identify the differences between standing and propagating waves without spectroscopic signatures. Recently, Yuan *et al.* (2015) have performed forward modelling of standing slow magnetoacoustic waves in flaring loops. They have reported that the variation of amplitude along the coronal loops is one of the signatures of the standing slow magnetoacoustic waves (see Figure 8 in Yuan *et al.* 2015). Moreover, a small phase shift in the intensity variations with time at different distances along fan loop corresponding to the slice S1, as seen in Figure 5.4, can be due to the presence of standing slow oscillations (Taroyan *et al.* 2007; Taroyan and Bradshaw 2008). We estimated the time period of the oscillations to be ∼27 minutes and the damping time to be ∼45 minutes. We calculated the projected length of the fan loops and estimated that the velocity of oscillations are comparable to the velocity of sound in 171 and

193 Å. These signatures allow us to conclude that the observed oscillations are due to standing slow waves in coronal fan loops. The fan loops under study are associated with a sunspot. Yuan *et al.* (2011) reported the presence of long-period oscillations in the coronal diffused plasma near an active region. The oscillations observed in this study are different from those reported by Yuan *et al.* (2011) because the event under study was triggered by the energy impulse of flares, while Yuan *et al.* (2011) studied the persistent leakage of long-period oscillations from the underneath sunspot.

It is worth mentioning that only one footpoint of fan loops was clearly seen in AIA 171 and 193 Å images. At this stage we can only conjecture two possible scenarios by which the reflection of the wave from the other end can happen. Either the antinode of the oscillations is present at the other footpoint, which is distributed and therefore not seen clearly in normal-intensity images, or the antinode could be present at the region of sharp density contrast close to the other end of the fan loop. The region of sharp density change may have acted as a reflecting surface. These scenarios may be experimented on in future studies using computer simulations.

At most of the locations along the fan loops, oscillations are found to be undamped. The reason for the absence of damping at most of the locations is not clear to us; more observations of such events are required to reach conclusive views on the damping. However, at a few locations along the fan loop, we indeed noted weak damping. The oscillations at those locations are weakly damped as compared to those reported in Ofman and Wang (2002); Wang *et al.* (2002, 2003b, 2015), where the damping time was comparable to the time period of the oscillations in hot and flaring coronal loops (T $>$ 6 MK). One of the reasons for weak damping could be because the fan loops under study are not hot ($\sim$0.7 MK); thus, the thermal conduction may not be efficient enough. Since thermal conduction is one of the main mechanisms to damp slow waves, the oscillations were weakly damped in our study.

In summary, we found the signatures of standing slow magnetoacoustic waves in cool fan loops. In earlier studies, these oscillations were particularly observed in the hot coronal loops. To the best of our knowledge, this is the first report on the observational signatures of the existence of weakly damped standing oscillations in cool fan loops.

Chapter 6

Automated Detection of Coronal Mass Ejections in STEREO Heliospheric Imager data[†]

6.1 Introduction

According to the original definition, coronal mass ejection (CMEs) are an observable changes in coronal structure, which occur on time scales from a few minutes to several hours and involve the appearance (Hundhausen *et al.* 1984) and outward propagation (Schwenn 1996) of new, discrete and bright white-light features in the coronagraph field of view. CMEs result from the episodic expulsion of plasma and magnetic field from the solar atmosphere into the heliosphere with speeds, which are typically 400 km s^{-1}, but which can range from 100–2500 km s^{-1} (Yashiro *et al.* 2004; Manoharan and Mujiber Rahman 2011). CMEs are considered the

[†]Results of this work are published in Pant *et al.* (2016b).

All the animations that are referred to in this chapter are available at `http://dx.doi.org/10.3847/1538-4357/833/1/80`.

most energetic events in the solar system. Furthermore, they are very important in terms of space weather, being the drivers of the largest geomagnetic storms detected on Earth. Since 1996, we have been able to monitor CMEs routinely from the L1 vantage point using the Large Angle Spectrometric Coronagraph (LASCO) (Brueckner *et al.* 1995) on the Solar and Heliospheric Observatory (SOHO) spacecraft. Moreover, since late 2006, we have also been able to monitor CMEs from a location off the Sun-Earth line using the COR1 and COR2 coronagraphs, which form part of the Sun–Earth Connection Coronal and Heliospheric Investigation (SECCHI) (Howard *et al.* 2008) imaging package on the twin-spacecraft Solar Terrestrial Relations Observatory (STEREO) mission. The SECCHI Heliospheric Imager (HI) instruments on STEREO effectively extend the coronagraph observing methodology out to larger distances from the Sun by providing wide-angle white-light imaging of the heliosphere out to 1 AU and beyond (Eyles *et al.* 2009; Harrison *et al.* 2009). The HI instrument on each STEREO spacecraft comprises two cameras, HI-1 and HI-2. The angular fields of views (FOVs) of HI-1 and HI-2 are 20° and 70°, with the FOVs being centered, in nominal operations, at around 14° and 54° elongation, respectively (Socker *et al.* 2000). The extensive HI FOV allows us to observe CMEs propagating over vast distances of interplanetary space (Eyles *et al.* 2007; Davis *et al.* 2009; Harrison *et al.* 2008, 2009). The concept of wide-angle heliospheric imaging was first demonstrated by the Solar Mass Ejection Imager (SMEI) on board the Earth-orbiting *Coriolis* spacecraft (Eyles *et al.* 2003). The terminology of interplanetary CMEs (ICMEs) is often applied to the interplanetary counterparts of CMEs (see, Gopalswamy *et al.* 2000; Riley *et al.* 2006; Zurbuchen and Richardson 2006). However, due to the success of *Coriolis*/SMEI and STEREO/HI in filling the vast observational gap between coronagraph imagery and in situ measurements, some authors are now suggesting that the CME terminology should be applied to both phenomena (Webb and Howard 2012; Bisi *et al.* 2013).

Since the launch of STEREO, CMEs have been identified through visual inspection of HI images and the resultant event catalogs have been made public (Barnard

et al. 2014, 2015; Harrison 2016). However, such visual identification of CMEs is biased by human subjectivity and hence CME detection may or may not be consistent over an extended period of time (Wang and Colaninno 2014). It is worth mentioning that each CME in the Solar Stormwatch CME catalog Barnard *et al.* (2014) is identified manually by multiple independent operators in order to reduce the subjectivity of the detection. The properties of a given CME are derived by averaging the independent detections. Nevertheless, automated detection offers the capability of providing more objective CME detection. One such software package, Computer Aided CME Tracking (CACTus) was developed to detect CMEs in LASCO/C2 and C3 coronagraph images (Robbrecht and Berghmans 2004) and subsequently applied to COR2 coronagraph imagers from STEREO. CACTus applies the original definition of a CME; "a CME is a new, discrete, bright, white-light feature in the coronagraph FOV with a radially outward velocity" (Robbrecht and Berghmans 2004). CME detection using CACTus is more objective and faster compared with the visual identification, because CMEs are detected, and characterised according to a strict set of precisely defined constraints. The catalogs produced using CACTus (available online[1]) are similar to manually compiled catalogs in terms of the parameters that they contain. Robbrecht *et al.* (2009) have compared the CME parameters derived by CACTus with those obtained by manual detection of CMEs in LASCO/C2 and C3 images. Apart from CACTus, there are several other catalogs of CMEs, which have been identified automatically in coronagraph data. The Coronal Image Processing (CORIMP) automated detection algorithm uses normalized radial gradient filtering and deconvolution to separate quiescent structures (background corona) and dynamic structures (features such as CMEs, which propagate radially outward) (Morgan *et al.* 2012; Byrne *et al.* 2012). CORIMP has been used to detect CMEs automatically in LASCO and COR2 images. Another such algorithm, The Automatic Recognition of Transient Events and Marseille Inventory from Synoptic maps (ARTEMIS), was developed

[1] `http://sidc.oma.be/cactus`

by Boursier *et al.* (2009). ARTEMIS detects CMEs automatically in LASCO synoptic maps using image filtering and segmentation techniques. Furthermore, the Solar Eruptive Events Detection System (SEEDS) also detects CMEs in polar transformed running difference images from LASCO and COR2 (Olmedo *et al.* 2008). SEEDS isolates the leading edges of CMEs by intensity thresholding; by tracking CMEs in sequential images, their speed and acceleration are calculated. Byrne (2015) compared the CORIMP catalogs with catalogs generated using other automated (*i.e,* CACTus and SEEDS) and manual detection methods (*i.e* the CDAW catalog). The authors demonstrated the robustness of CORIMP in deriving the kinematics of the automatically detected CMEs. The automated detection of CMEs in the heliosphere is, however, not an easy task, mainly due to their low brightness compared to that of the other contributions to the white-light signal (principally the F-coronal and stellar backgrounds). Despite this, there have been previous attempts to automatically identify CMEs in heliospheric images. The Automated Interplanetary Coronal Mass Ejection Detection (AICMED) tool was developed by Tappin *et al.* (2012) to detect CMEs in SMEI data, in particular. Like CACTus, AICMED works on the principle of the Hough transform, which detects straight ridges. AICMED uses the Hough transform to detect curved ridges in time-elongation maps (commonly called J-maps) by splitting each curved ridge into several straight ridges (this curvature, as will be discussed later, is a geometric artifact associated with imaging out to large elongations). However, due to a number of features in the SMEI data (such as rings generated by hot pixels, scattered light from the moon, cometary tails, high-altitude aurora and particle hits during crossings of the South Atlantic Anomaly (SAA) and auroral zones), there were many false detections. Recently, Barnard *et al.* (2015) reported the differences in velocities estimated using automated and manual tracking of ridges in time-elongation maps created from STEREO/HI-1 and HI-2 images (see also, Savani *et al.* 2009), although the authors did not perform a completely automatic detection of CMEs in the HI imagery.

We have adapted the CACTus software package to automatically detect CMEs in

STEREO/HI-1 data. In this chapter, we first describe the methodology, which we have used (Section 6.2). Subsequently, in Sections 6.3 and 6.4, we compare the automatically derived parameters for a selection of CMEs with analogous entries in a manual catalogs for a selection of CMEs: namely the time of appearance (t_0), central position angle (CPA) of propagation, position angle (PA) width (da) and the projected speed (v).

6.2 Method of Detection

In this section, we describe the method of automated detection of CMEs in HI-1 data from STEREO-A, which is an adaptation of the original CACTus methodology, as discussed in Robbrecht and Berghmans (2004), but with some modifications in order to make it work with the HI images. CME detection by CACTus is based on the principle of the Hough transform (see, Jahne 1997), which can be used to detect straight lines in noisy data. The brightness of CMEs in heliospheric images is generally lower relative to other contributions to the signal (such as F-coronal and stellar backgrounds) than in coronagraph images, leading to an inferior signal-to-noise ratio. Since the automated detection of CMEs depends critically on their clarity, we need to carefully process the images before implementing the Hough transform to the time–height maps.

6.2.1 Preprocessing of HI Images

- *Data acquisition*: The 1 day background-subtracted level 2 HI-1 science images (array size, 1024 × 1024) in units of DN s^{-1} per CCD pixel are downloaded via the UK Solar System Data Center (UKSSDC) website[2] (note

[2] `http://www.ukssdc.rl.ac.uk/solar/stereo/data.html`

that pixels on the CCD detector are binned 2 × 2 onboard to generate the science images; our subsequent use of the term pixel refers to a pixel in a science image). These images have a nominal cadence of 40 minutes. For illustration throughout Section 6.2, we analyse HI-1 images from the period extending from the beginning of 02 April 2010 to the end of 04 April 2010, encompassing about 72 hours. However, in Section 6.3, when comparing with the results of manual cataloging, we include five additional days in our analysis. The background, which is subtracted from each HI-1 image, is the average of the lowest quartile of the data in each pixel within the FOV over a 1 day period centered on the image of interest[3] (Tappin *et al.* 2016). By subtracting a daily background, quasistatic components of the signal, principally the F-corona and also the less variable elements of the K-corona (e.g., streamers) are removed. Such a 1 day background-subtracted level 2 HI-1 image from STEREO-A is shown in the left-hand panel of Figure 6.1. The processing, which has been applied to the images, is described on the UKSSDC website[4].

- *Removal of stars and planets*: It is evident from this image that the white-light signal due to the presence of bright stars and planets in the FOV can exceed the CME signal (the leading edge of the CME is marked with a yellow arrow). The stars and planets are not removed by the background-subtraction procedure as they move through the FOV at a relatively fast rate. To reduce the effects of the stars and the planets we use a sigma filter, which works by first computing the mean and the standard deviation of the intensity of the neighbouring pixels excluding the pixel on which it is centered. If the intensity of the central pixel is greater than a chosen threshold (mean + 4 × standard deviation), its value is replaced by the mean value of its neighbouring pixels. This process is iterated over all of the pixels in an image, recursively up to 20 times or until no further change is

[3] `http://www.ukssdc.rl.ac.uk/solar/stereo/documentation/HI_processing_L2_data.html`

[4] `http://www.ukssdc.rl.ac.uk/solar/stereo/documentation/HI_processing.html`

observed. By examining a few test cases, we determined that using a sigma filtering with a width of 50 pixels works well at reducing the effects of planets and stars.

- *Removal of bright streaks associated with planets and bright stars*: Unlike for coronagraphs with their smaller FOVs, in which only a few planets and bright stars tend to be present at one time, more planets and bright stars are present in the somewhat larger HI-1 FOV. Planets and bright stars are associated with bright vertically extended streaks, which result from vertical blooming of the signal in saturated pixels. It is crucial to remove these bright vertical streaks prior to CME detection. It should be noted that the *secchi_prep.pro* routine (which is applied to the HI data as part of the processing performed at the UKSSDC) attempts to replace the bright vertically extended streaks with NaN values (NaN streak). However, we find that this procedure is often not always totally effective. An incompletely removed bright streak may still be brighter than a CME in the difference images, which are used for CME detection by CACTus (see Section 6.2.2) and, therefore, may affect the CME detection. Hence, CACTus performs additional processing of the HI-1 data, which is not present in earlier versions of the software, in order to remove these residual bright streaks. This process involves the use of dilation. Dilation is an image processing technique, which "grows" or "widens" an object. The extent of the widening is based on the shape of the kernel (Gonzalez and Woods 2002). We choose a 1D kernel with a horizontal width of 6 pixels for dilation. This width of kernel is found to work well at covering any residual bright vertical streaks associated with a planet or bright star. Upon its application, the original NaN streak, which is implemented in the UKSSDC processing, becomes wider, as a result of which any residual bright streak is completely replaced by NaNs. This process results in the highly effective replacement of the residual bright streaks in the HI-1 images. Subsequently, we use convolution based on a 1D kernel of 100 pixels in width to replace the NaN streak with values of the

neighbouring (horizontal) pixels (note that the NaN streak extends over the entire vertical range of the image). Through this procedure, we isolate the position of the dilated NaN streak and replace it with the intensity obtained through convolution. This fills the affected pixels with the values of the surrounding pixels without smoothing the entire image.

The processed image after the application of the above procedures is shown in the right-hand panel of Figure 6.1. The CME is now brighter relative to the stars and planets, which are suppressed and the residual bright streak (with its associated NaN streak) is now filled with neighbouring intensity values.

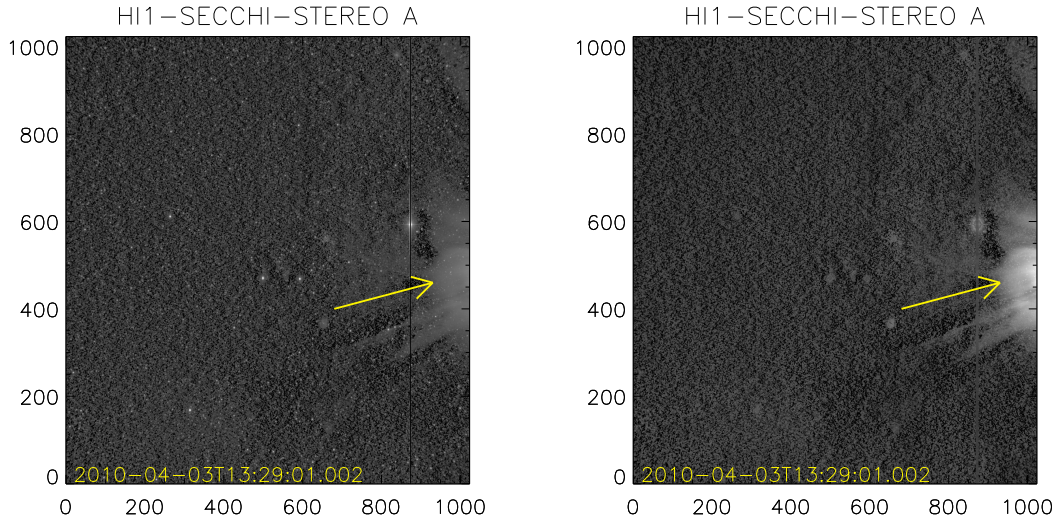

FIGURE 6.1: Left: level 2 STEREO-A HI-1 image after 1 day background subtraction and the initial removal of bright streaks (most clearly that resulting from the presence of Mercury in the FOV). Right: As left, but with further processing to reduce the effects of bright planets and stars (as discussed in the text). The yellow arrow indicates the leading edge of a CME (at a PA of 102°) observed on 03 April 2010.

6.2.2 Polar Transformation

The next step towards the detection of CMEs in STEREO/HI imagery is the conversion of the helioprojective Cartesian (HPC) coordinates provided as one of the standard coordinate system of the HI images, into polar $(\theta - r)$ coordinates, where θ is the PA, measured counterclockwise from solar north, and r is the distance from the Sun-center projected onto the plane of sky (POS), as seen from the spacecraft.

- In order to do this, we first convert the HPC coordinates of the HI images to helioprojective-radial (HPR) coordinates (see Thompson 2006) using routines, which are available in the SolarSoft package. It should be noted that the accurate pointing calibration of the HI imagery is achieved in the UKSSDC preprocessing through comparison of the star field within each image with a star catalog (Brown *et al.* 2009).

- The conversion to HPR, assigns each pixel in the HI image with two values, the PA (θ) and the elongation (ϵ), the angle between its line of sight (LOS) and the spacecraft-Sun line. Knowing the elongation of each pixel in the image, we can calculate its projected distance from the Sun-centre on the POS, using the expression

$$r = d\ \tan(\epsilon), \tag{6.1}$$

  where d is the distance of the observing spacecraft from the Sun.

- The polar $(\theta - r)$ representation of the image presented in the right-hand panel of Figure 6.1 is shown in the left-hand panel of Figure 6.2, where the x-axis represents PA (θ) and the y-axis represents the projected distance in the POS derived using Equation 6.1. The data are binned such that one height bin corresponds to 100,000 km (roughly $1/7^{th}$ of solar radius). Since CMEs

are large-scale features, this binning does not lose any structural information. Furthermore, binning reduces noise and computation time.

- To remove quasistatic features, which vary on a time-scale shorter than the 1 day subtracted background, and longer than the 40 minutes image cadence of HI-1, running difference $\theta-r$ images are generated automatically in a manner analogous to what is done in the conventional version of CACTus (Robbrecht and Berghmans 2004). In particular, this removes much of the shorter time-scale variation of the streamer belt. The right-hand panel of Figure 6.2 shows only the positive values of the difference image (corresponding to an increase in brightness, hence density, relative to the previous image).

6.2.2.1 Geometric models and fitting methods

Since the advent of wide-angle imaging of the solar wind, by *Coriolis*/SMEI and STEREO/HI, a number of geometries have been derived, which enable the elongation angle of a CME (or other solar wind structure) to be converted to a radial distance from the Sun-center, namely Point-P (PP; Howard *et al.* 2006), Fixed-ϕ (FP; Kahler and Webb 2007; Rouillard *et al.* 2008; Sheeley *et al.* 2008a), Harmonic Mean (HM; Lugaz *et al.* 2009), and Self-Similar Expansion (SSE; Davies *et al.* 2012). The FP, HM, and SSE conversion methods require knowledge, or assumption, of the 3D propagation direction of a solar wind transient (such as from its source location on the Sun). As we do not know the propagation direction of the CME *a priori*, it is easiest to assume that it propagates at an angle of 90° from the Sun-spacecraft line (*i.e* in the POS). The POS approximation (as described by Equation 6.1) is, in fact, a special case of the FP conversion methodology. The PP approximation works on the principle that the maximum brightness contribution along any LOS comes from the point closest to the Sun (*i.e,* the Thomson sphere), as discussed by, for example, Vourlidas and Howard (2006) and Howard and DeForest (2012). Howard and DeForest (2012) and Inhester (2015) have shown that,

in fact, Thomson scattering maximises over a wide range of angles around the Thomson sphere (the so-called Thomson plateau). We discount the use of PP, mainly because it traces out a non-radially propagating point on a CME front. Here, as discussed in Section 6.2.2, we adopt the POS approximation for deriving radial distance from elongation, which is consistent with the original CACTus ethos.

It is worth making the point here that it is actually possible to estimate the 3D propagation angle (and radial speed) of a solar wind feature, such as a CME, without having *a priori* knowledge of its source region, provided that it can be tracked over sufficient elongation extent. This can be done by analysing the curvature of its associated ridge in the J-map. Such curvature is present even if the feature is propagating at a constant speed in a fixed direction (see, for example, Figure 2 of Davies *et al.* (2012), where the authors plot simulated time-elongation profiles curves for FP, HM, and SSE geometries). By assuming a fixed geometry, the time-elongation profile of the ridge can be analysed to provide an estimate of the 3D propagation direction and radial speed. The current version of CACTus can only detect straight lines. Hence, we cannot estimate the 3D propagation angle in this way. Möstl *et al.* (2014) have reported that CMEs can decelerate out to 1 AU. Thus, in addition to the geometric artifact discussed above, any deceleration (or indeed acceleration) of a CME during its propagation will modify the curvature due to aforementioned effect. However, it should be noted that, even if some curvature is present, CACTus can still detect a ridge if it is sufficiently bright (such as the ridge detected at 20 hours at 15 $R_{\odot}$ in Figure 6.3). However, any velocity estimate may not be accurate.

We do not perform CME detection in HI-2 imagery, not least because of the inherent curvature in the signature of a CME propagating over a large range of elongations (Davies *et al.* 2012). As noted above, such curvature could adversely affect CME detection, when using the Hough transform implemented in CACTus,

as the Hough transform only detects straight lines. However, in the case of observations over a limited elongation extent (less than some 15°), the track of a CME propagating radially outwards at a constant velocity would be virtually straight. In practice, there would still be a some slight curvature over the elongation range covered by HI-1 but not enough to affect the performance of the algorithm, particularly since CMEs are mainly detected from the inner edge of the HI-1 FOV, an elongation of 4° out to 15°; the latter equated to a POS distance of 57 $R_{\odot}$. The slightly curved ridge in the left-hand panel of Figure 6.3 (detected in HI-1 FOV at 20 hours at 15 $R_{\odot}$) is successfully detected by Hough transform (shown in the right-hand panel of Figure 6.3) because it is bright. However, the speed estimate in this and similar cases may not be accurate.

Difference $\theta - r$ images (similar to the one that is shown in the right-hand panel of Figure 6.2) are stacked over time to produce a [θ,r,t] data cube, where θ is the PA, r is the radial distance and t is the time in hours from the start of the interval under analysis (up to 72 hours in this case).

6.2.3 Application of the Hough Transform

- For each value of the PA, θ, in the resultant [θ,r,t] data cube, we have what is effectively a time–height ([t,r]) map. The left-hand panel of Figure 6.3 shows the time-height map at $\theta = 102°$, for the interval covering the propagation of the CME shown in Figures 6.1 and 6.2 through the FOV of HI-1 on STEREO-A. This PA corresponds to the the yellow arrows in Figures 6.1 and 6.2 . The x-axis represents the time in hours from 00:00 UT on 02 April 2010 and the y-axis represents the POS distance from the Sun-center.

- Inclined ridges with a positive slope represent features traveling away from the Sun, such as the leading edge of the CME shown in Figures 6.1 and 6.2 (the track of this CME front is indicated by a yellow arrow in Figure 6.3). Faint ridges with negative slope correspond to the residual star signal. Prior

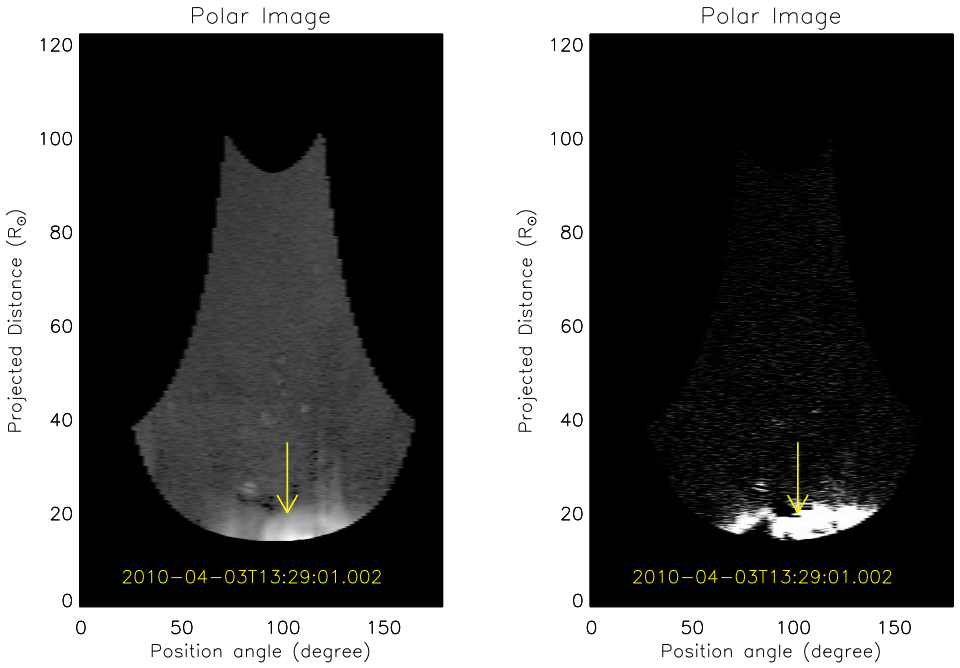

FIGURE 6.2: Left: polar transformation of the image presented in the right hand-panel of Figure 6.1. Right: difference and thresholded version of the left-hand image. The yellow arrows represent the leading edge of the CME co-spatial with the arrow shown in Figure 6.1.

to superior conjunction (since which the STEREO-A spacecraft has been rotated by 180°), the motion of STEREO-A was such that the apparent drift of the star field across HI images was sunward (*i.e* in the opposite direction to CMEs). One should be aware that there could be multiple CMEs propagating along a particular PA over any extended time range (which is why we mark the ridge corresponding to the CME of interest here with a yellow arrow).

- The Hough transform is defined as the mapping from image space (in this case a time–height map) to parameter space (or accumulator space) (see, Jahne 1997; Robbrecht and Berghmans 2004). An inclined ridge is uniquely characterized by two parameters, its slope (m) and intercept (c), provided the slope is not infinite. Since CMEs propagate antisunward with finite velocities, the inclined ridges related thereto have positive finite slope. One ridge maps to a single point in accumulator space (see Figure 2 in Robbrecht

and Berghmans 2004). The weight given to the point in accumulator space is determined by the number of points lying along the ridge in the time–height map. Brighter ridges in the time–height map tend to be given larger weights in accumulator space than fainter ridges, as they can be usually be tracked out further in radial distance.

- As noted above, CACTus uses the Hough transform to isolate (as straight lines) the significant ridges in time–height maps associated with the passage of CMEs. We filter out those points in accumulator space with a low weighting by applying a weight threshold, W_{thresh}, which is given by,

$$W_{thresh} = W_{mean} + f \times W_{sd} \tag{6.2}$$

where, W_{mean} and W_{sd} are the mean and standard deviation of the weights of all points in accumulator space and f is an arbitrary factor. CACTus uses an empirically based value of $f = 4$ in the analysis of the STEREO/HI-1 data, based on analysing a sample of CMEs.

- Points in accumulator space with weights, which exceed W_{thresh}, are taken to be the points, which correspond to the tracks of CMEs in time–height maps. The time–height map presented in the right-hand panel of Figure 6.3 reproduces that shown in the left-hand panel, but with significant ridges (corresponding to those points in accumulator space, which exceed W_{thresh}) overplotted in green. We plot the green curves over the full height range. The coordinates of the detected points in accumulator space, *i.e* m and c of each detected ridge in the time–height map, provide an estimate of the POS velocity (v) and time of first appearance of each detected CME (t_0), respectively. t_0 does not represent the time that the CME first appears in the HI-1 FOV but, instead, corresponds to the back-projected time at which the CME would be at the Sun-centre (*i.e.,* r=0). This is because the data cube input into CACTus extends from r=0. To estimate the time at which the CME enters the HI-1 FOV, a correction to t_0 is required; no

such correction to the velocity is required. The correction depends on the velocity of a ridge and the distance to the inner edge of the HI-1 FOV. Unlike coronagraph images, where the inner edge of the FOV is independent of θ (because the occulter is circular), the POS distance of the inner edge of the HI-1 FOV depends on θ (see Figure 6.2). For the time–height map presented in Figure 6.3, this distance is 15 $R_{\odot}$. The θ dependent correction of t_0, which is implemented in the current version of CACTus, was not present in earlier versions. As discussed above, a ridge in time–height map corresponds to the propagation of a CME along a particular PA (θ). We perform the Hough transform on time-height maps at every PA within the HI-1 FOV. Since CMEs are extended in θ, a single CME will correspond to a cluster of points in the resultant [θ,v,t_0] data cube.

- CACTus subsequently performs integration over v in order to obtain a [θ,t_0] map. We use a morphological closing technique to fill the gaps between the points of a cluster in such a map. This technique performs dilation of an image (as described above) followed by the contraction, using a kernel of a given size (see, Gonzalez and Woods 2002). This process fills gaps between the points in a cluster in the [θ,t_0] map, which are smaller than the size of the kernel.

- Unlike the version of CACTus implemented on coronagraph images, which uses a 1D kernel with a width of 5 bins in the θ direction, a 2D kernel is used for detecting CMEs in HI-1 data. This kernel has a width of 8 bins in θ and 5 bins in t_0. This means that CACTus bridges the gaps between the points in accumulator space, which are less than 16° in θ and 200 minutes in t_0. These values are empirically chosen (through examination of a number of CMEs observed by HI-1) such that they connect different parts of the same CME together without (too often) combining different CMEs. Such morphological closing is required because, for example, a single CME often comprises more than one distinct feature (such as a leading edge and prominence material)

and, moreover, the brightness of even a single feature may be nonuniform in θ.

- The left panel of Figure 6.4 shows a $[\theta,t_0]$ map, which we will henceforth refer to as a CME map, which spans the same interval as presented in Figure 6.3 (*i.e.,* 02 to 04 April 2010). The x-axis represents PA and y-axis, time. The CME map illustrated in the right hand panel of Figure 6.4 presents the location, as a function of both PA and time, of the maximum POS velocity for each of the five CMEs detected by CACTus during the time interval covered by the time–height maps presented in Figure 6.3. The magnitude of the velocity is colour coded according to the colour bar. The white contours overplotted on the right-hand panel of Figure 6.4 illustrate the identified boundary of each cluster. Each cluster, of course, represents a separate CME detected by CACTus. Cluster 4 in the left-hand panel of Figure 6.4 corresponds to the CME under particular consideration here, images of which are shown in Figures 6.1 and 6.2.

It is also important to note that, for various reasons, there are occasional data gaps in the HI-1 telemetry stream. This not only leads to missing images, but also occasional incomplete images (so-called "missing blocks"). One advantage of the Hough transform is that it can detect ridges even in the presence of data gaps, provided the ridge is sufficiently bright and the data gap is sufficiently short (so that the weight of the point in Hough space corresponding to the ridge still exceeds W_{thresh}). Since we apply morphological closing in θ and time, data gaps will not adversely affect the results, unless they are too long or too frequent. If there are too many data gaps, CACTus might not detect any ridges or may detect multiple ridges. While this could be resolved by resampling prior to implementing the Hough transform, there are too few data gaps in the HI-1 imagery for this to be necessary.

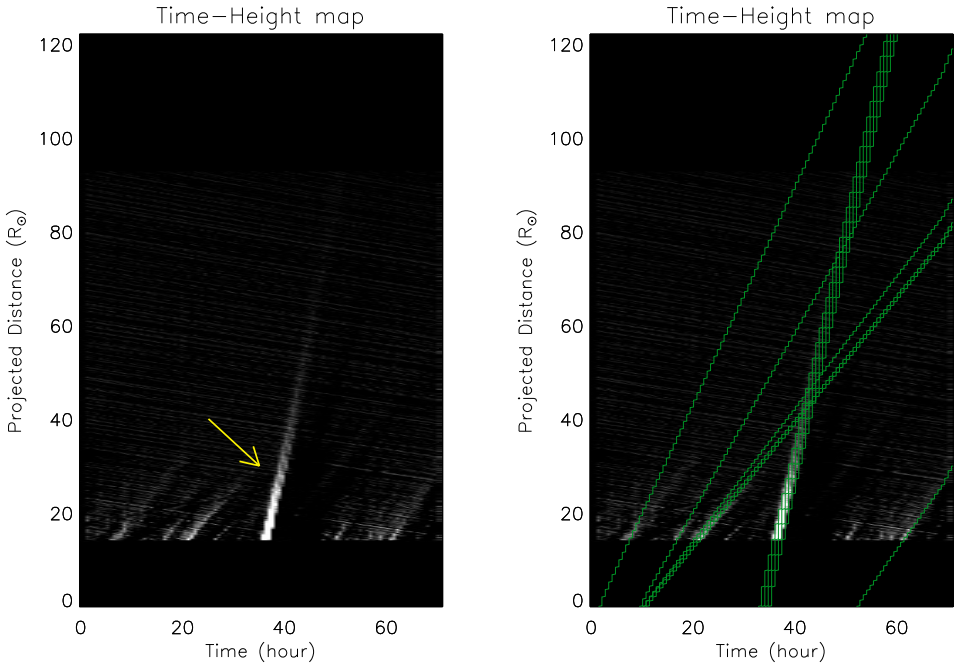

FIGURE 6.3: Left: time–height map at 102° PA, generated from HI-1 images from STEREO-A, covering the interval that extends from 02 to 04 April 2010. The yellow arrow indicates the inclined ridge corresponding to the leading edge of the particular CME of interest. Right: as for the left, but overplotted with green curves, which represent the significant ridges detected through the application of the Hough transform.

6.2.4 Determination of CME position angle (PA) width, time of appearance and velocity

- *Estimation of PA width*: Once the so-called CME map has been created, the PA width of a CME is estimated by calculating the extent of the corresponding cluster in the CME map in the θ direction. It is important to note that for each CME the PA width provided by CACTus is the maximum width of that CME throughout its propagation through the HI-1 FOV. The CPA of propagation of a CME is calculated as the midpoint of its associated cluster in θ. Figure 6.5 shows difference images for two of the CMEs (CMEs that correspond to clusters 4 and 5 in Figure 6.4), which are detected by the application of CACTus to HI-1 imagery from STEREO-A during the time interval extending from 02 to 04 April 2010 (see animated Figures 6.7 and

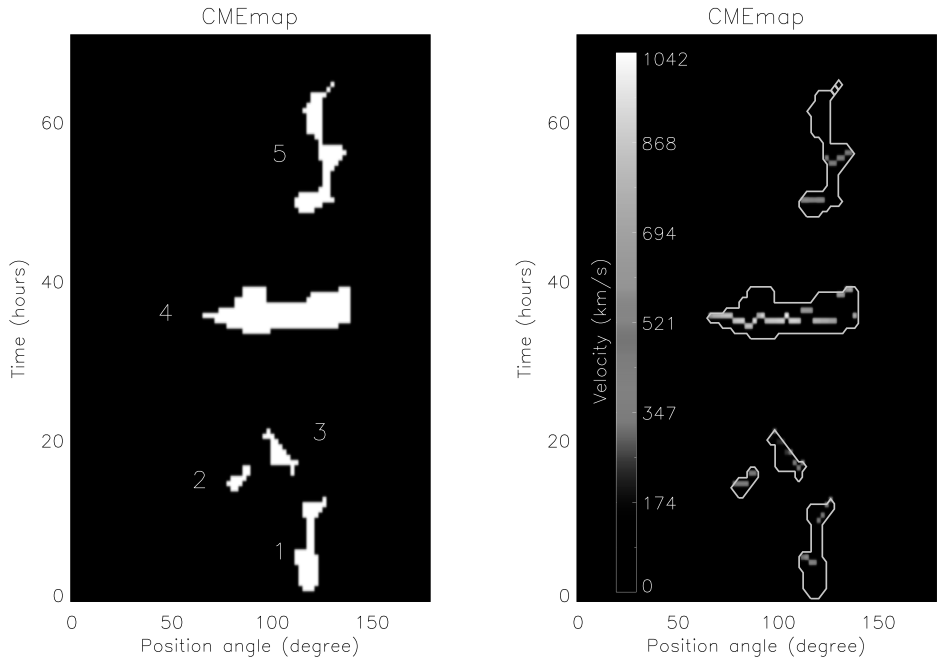

FIGURE 6.4: Left: CME map showing five clusters of points representing five different CMEs detected during the time interval extending from 02 to 04 April 2010. The clusters are numbered according to their time of first appearance. Right: CME map showing for each cluster (i.e, for each CME), the maximum velocity (color coded) at each PA over the entire PA extent of the CME. White contours represent the identified boundaries of the clusters.

6.8 available online). In each case, the PA width yielded by the method is delimited by white lines.

- *Estimation of time of appearance*: To estimate the time of appearance of a specific CME in the HI-1 FOV, a local background intensity and standard deviation for the corresponding cluster in the CME map is first estimated using the $[\theta, r, t]$ data cube. For each cluster in a CME map, a local background intensity is estimated by fitting a straight line to the intensity, which is summed over the PA width and radial distance extent of the $[\theta, r, t]$ data cube over a time range, which extends from 30 images before the lower boundary of a cluster to 30 images after the upper boundary of the same cluster. The value of 30 is chosen empirically. The time of appearance of a

CME is defined as being the time beyond/after the lower boundary of a cluster at which the intensity first exceeds the background value by 2σ, where σ is the standard deviation of the intensity. We do not simply use the lower boundary to determine the time of appearance as CMEs can generate waves or shocks, which can be manifest as regions of faintly enhanced brightness prior to the appearance of the CME itself. Moreover, small blobs are sometimes observed to propagate radially outward ahead of a CME (Robbrecht *et al.* 2009). Such brightenings ahead of CMEs may (or indeed may not) be detected by the Hough transform. If such features are identified in accumulator space, they may subsequently be amalgamated with the main cluster after the application of the morphological closing technique. Therefore, the lower boundary itself may not represent the true time of CME appearance. If any such feature or unstructured flow (for example, streamer blobs) prior to CME appearance is bright enough to exceed the 2σ threshold then it will affect the estimated time of arrival (potentially making it earlier than what would be deduced from visual inspection).

- *Estimation of velocity*: Each bin in a CME map that falls within a CME cluster is associated with a velocity, v. For each cluster of points in a CME map, and thus for each CME, we identify the maximum velocity at each PA within the identified CME PA span (right-hand panel of Figure 6.4). The left-hand and right-hand panels of Figure 6.6 show the maximum velocity as a function of PA for the CMEs, which correspond to clusters 4 and 5, respectively, in Figure 6.4 (images of which are presented in Figure 6.5). Overplotted on each panel is a box-and-whisker key depicting the range of maximum velocities over the entire PA extent of the corresponding CME. The upper and lower boundaries of the box itself represent the upper and lower quartiles of the distribution of maximum velocities; the median value is marked by horizontal line inside the box. The whiskers encompass the highest and the lowest value of the maximum velocity.

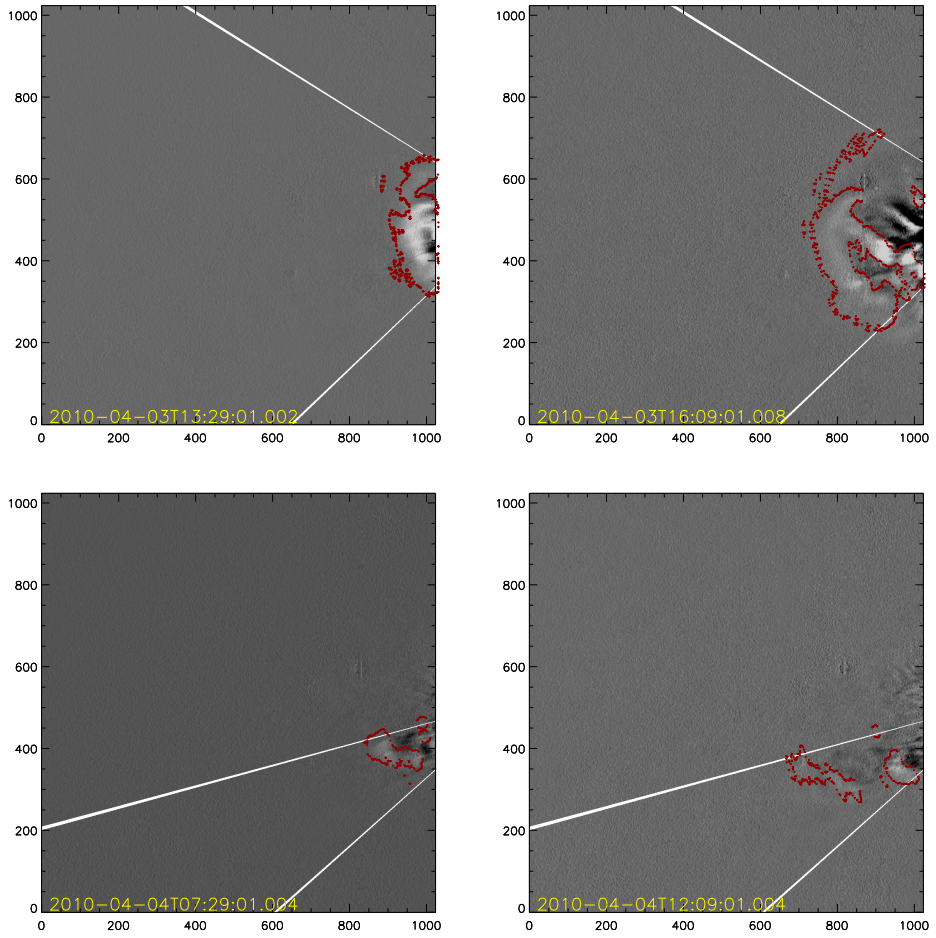

FIGURE 6.5: Top: difference images of the CME corresponding to cluster 4 in the left-hand panel of Figure. 6.4 (No. 4 in Table 6.1). White lines delimit the northernmost and southernmost PA extents of the CME. Bottom: same as left-hand panel, but for cluster 5 (No. 5 in Table 6.1). Points overplotted in red represent the perimeter of the radially outward moving features identified by application of the Hough transform.

Estimated parameters of all five CMEs, which were detected by CACTus in HI-1 images from STEREO-A/HI-1 images during the time period extending from 02 to 04 April 2010 (including the two CMEs shown in Figure 6.5) are listed in Table 6.1.

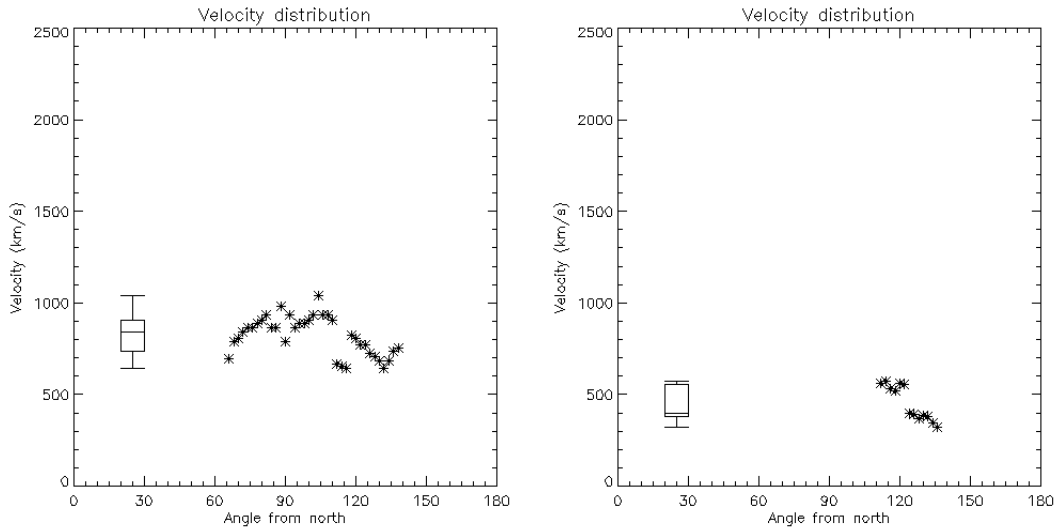

FIGURE 6.6: Left: maximum velocity as a function of PA (measured counter-clockwise from solar north) for the CME detected as cluster 4 in the left-hand panel of Figure 6.4. Right: same as for the left, but for cluster 5. The box-and-whisker keys indicate the median and quartiles of the velocity distribution, as well as the minimum and maximum velocity values (see text for details).

6.3 Comparison with manual catalog

We have applied CACTus to eight different days of STEREO-A/HI-1 images (04 April 2010, 03 April 2010, 02 April 2010, 12 December 2008, 26 April 2008, 04 February 2008, 22 October 2007, and 19 April 2007) and have compared the results with those of manual CME cataloging endeavors, in particular those performed as part of the EU FP7 Heliospheric Cataloging Analysis and Techniques Service (HELCATS) project[5]. The manual catalog compiled as part of HELCATS work package 2 contains observational CME parameters (in particular, time of first observation and northern and southernmost PA extents) obtained through visual inspection of the STEREO/HI-1 images. This catalog is available online[6]. Indeed, the application of CACTus to the STEREO/HI-1 imagery documented here is also performed under the auspices of the HELCATS project. The HELCATS manual

[5] `http://www.helcats-fp7.eu`
[6] `http://www.helcats-fp7.eu/catalogues/wp2_cat.html`

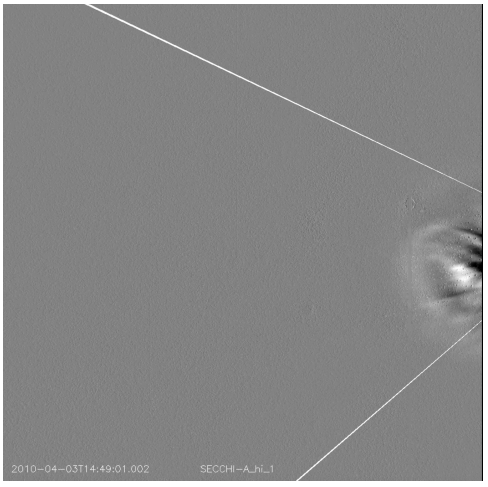

FIGURE 6.7: Movie corresponding to this animated Figure shows the CME moving outward antisunward. The angular width of CME is delimited by white lines.
(An animation of this figure is available.)

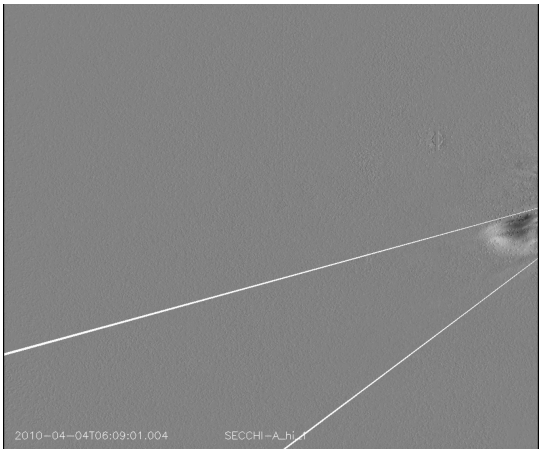

FIGURE 6.8: Movie corresponding to this animated Figure shows a narrow CME moving outward. The angular width of the CME is delimited by white lines.
(An animation of this figure is available.)

catalog is described, and preliminary analysis undertaken, by Harrison (2016). Moreover, we compare the CACTus POS speed estimates with those contained within the augmented (work package 3) version of the HELCATS manual CME catalog[7], which also includes estimates of 3D radial speeds calculated along, or at least near, the CPA of each CME. The 3D speeds in this augmented catalog are derived through the analysis of the time-elongation profiles of the CMEs manually

[7] `http://www.helcats-fp7.eu/catalogues/wp3_cat.html`

tracked in time-elongation maps (J-maps) generated from combined HI-1 and HI-2 imagery, using three techniques : Fixed-ϕ Fitting (FPF; Rouillard *et al.* 2008), Self-Similar Expansion Fitting (SSEF) with an assumed angular half width of 30° (Davies *et al.* 2012) and Harmonic Mean Fitting (HMF; Lugaz *et al.* 2009). The FP, HM and SSE geometries that underlie these fitting techniques assume different values for the cross-sectional width of a CME. FP assumes a half width of 0°, *i.e,* CME is a point source, whereas HM assumes a half width of 90°, *i.e,* a circle tied to Sun-center. The SSE geometry is more general, with a half width that can be anywhere between 0 to 90°. 30° is chosen for use in the HELCATS manual catalogs to account for the fact that the average angular span of CME is around 60°. We reiterate here that the POS approximation used by CACTus is a special case of the FP approximation, assuming CME propagation to be at 90 ° from the Sun-spacecraft line.

6.3.1 Comparison of number of events detected

During the 3 day period extending from the beginning of 02 April 2012 to the end of 04 April 2010, CACTus detected five CMEs (see, Figure. 6.4 and Tables 6.1 and 6.2). Since we incorporated that three day period into a single CACTus analysis, we get only a single CME map (shown in Figure. 6.4), which contains all events detected during that period. The other 5 days were analysed individually. Table. 6.2 compares the number of CMEs detected by CACTus with the number detected manually as a part of the HELCATS project. We find that CACTus detected more events than were listed in the manual catalog during the 8 days analysed (11 as opposed to 6). Over-estimation of the number of CMEs appears to be a common feature of CACTus (see Robbrecht *et al.* 2009). Having examined the CMEs automatically identified in the HI-1 data, we find that, in some cases, CACTus identifies multiple separate events, which, on closer investigation, are part of a single CME. *For example,* one event detected by CACTus on 26 April 2008

was found to actually be the flank of a separately detected CME. In that case, both the apex and the flank of the CME were bright, while the region between them was faint, hence their detection by CACTus as two separate events. The CME identified by CACTus on 04 April 2010 (Figure 6.5 (bottom panel)) is not listed in the HELCATS manual CME catalog. This is probably because this CME is narrower than the 20° PA width threshold imposed in the HELCATS manual cataloging. Similarly, the three events detected by CACTus on 02 April 2010 (CMEs 1, 2, and 3 in Figure 6.4), all are narrow unstructured features propagating radially outward (these are still identified as CMEs by CACTus according to the definition implemented therein) and are, therefore, not listed in the HELCATS manual catalog. In this work, we have set a threshold of 10° in PA width for a feature detected by CACTus to qualify as a CME; application of CACTus to coronagraph images generally uses 5°.

In summary, CACTus detected all CMEs present in the manual catalog, although one of them was erroneously identified by CACTus as two separate events. Moreover, use of a 10° (rather than 20°) PA width threshold resulted, over these 8 days, in the identification by CACTus of four additional, narrow, CMEs. It could be argued that such narrow CMEs, which (presumably they are small blobs of plasma) usually follow a larger CME, ought not to be categorised as a separate CME, but as a part of the preceding CME. In manual cataloging, such association is at the discretion of the operators. CACTus applies a more objective definition; any feature (with brightness exceeding W_{thresh}), which appears more than 200 minutes after the appearance of a CME, is considered as a separate CME. Although this is the objective application of what is still a subjective threshold, it means that CME detection will remain consistent over a long period of time, provided that there are no significant changes in instrument performance (see, Tappin *et al.* 2016).

6.3.2 Comparison of angular width

We also note that CACTus estimates consistently lower PA widths for the CMEs detected during the days under study than those presented in the HELCATS manual catalog (see, Table. 6.3). We suggest that a possible reason for this is that CMEs expand as they propagate outward. Moreover, the flanks of a CME are often fainter than its leading edge. Consequently, the ridge corresponding to the flank of a CME in a time–height map at a given PA may not be sufficiently extended or bright to result in its detection by CACTus (*i.e.* its weight may not exceed W_{thresh}). Another possible reason for the discrepancy in manually and automatically deduced PA widths could be related to the fact that for fast CMEs in particular, the CME is often surrounded by a shock that tends to be fainter than the CME itself. We believe that it is more likely that a manual cataloger would be influenced by the presence of even faint shocks when estimating the CME width. Depending upon the brightness of the shock, it may (or may not) be detected by CACTus. It is debatable whether a shock or any structures adjacent to the CME, which are deflected due to the presence of a shock, should (or should not) be included when estimating the width of a CME. However, we believe that the CACTus results would only be affected by the presence of the brightest shocks (*i.e* those with the longest tracks in a time–height map). It should be pointed out that the discrepancy in the PA width estimation is also seen when comparing the width of CMEs detected by CACTus in coronagraph data with those detected manually (Robbrecht *et al.* 2009). Thus we believe that the estimation of the PA width of CMEs in HI-1 data is affected by: (a) possible non-radial motion of CMEs, (b) the tendency of CME flanks to be faint and hence their ridges in time–height maps to be of limited extent and (c) the presence of faint shocks around CME flanks. Potentially, the PA widths estimated by CACTus could be made more consistent with the values in the manual catalog by lowering the intensity threshold, but doing so would also increase the number of false detections.

6.3.3 Comparison of time of appearance in the HI-1 FOV

We find that the times of first appearance (t_0) of the CMEs in the HI FOV, as estimated by CACTus and in the HELCATS manual catalog, are in fairly good agreement (see Table. 6.3), with the exception of the event on 19 April 2007. For that event, CACTus yields a time of entry into the HI-1 FOV, which is two hours earlier than the value quoted in the manual catalog. Having examined the images, we believe CACTus to be correct; the CME is already well inside the HI-1 FOV at the time of first appearance quoted in the HELCATS catalog. The reason for this discrepancy is not clear. Nevertheless, it confirms the rather subjective nature of manual cataloging. In general, it is thought that such time differences are due to (a) narrow blobs preceding a CME (Robbrecht *et al.* 2009) or (b) the inclusion of the shock ahead of a CME. This is discussed in greater detail in Section 6.4.

6.3.4 Velocity comparison

We have compared the POS velocity from CACTus with the best-fit 3D velocity derived using FPF (v_{FP}), SSEF (v_{SSE}) with an assumed angular half width of 30°, and HMF (v_{HM}). The speeds are quoted in Table 6.3. ϕ_{SSE}, also listed in Table 6.3, refers to the best-fit angle between the Sun-observer line (in this case STEREO-A) and the propagation direction of the CME returned by the SSEF technique (ϕ_{FP} and ϕ_{HM} are also quoted in HELCATS catalog, and for the CMEs considered here are similar in value to ϕ_{SSE}). Since SSE assumes a more generalized geometry, which reduces to FP and HM geometries under certain limits, we have quoted only ϕ_{SSE} for the CMEs considered in Table 6.3. In particular, we compare the POS velocities from CACTus with those derived using the FPF technique, because the POS geometry is a special case of the FP geometry.

Note that ϕ_{SSE}, is a reasonable proxy for the longitudinal separation between the CMEs and the spacecraft. We find that the POS speed from CACTus and v_{SSE} match reasonably well, except for the CME on 22 October 2007. We note that ϕ_{SSE} for this event is 174°, meaning it propagated more or less directly away from the spacecraft. Therefore, its projected speed in the POS would be a gross underestimate of its 3D radial speed. The POS approximation underestimates the 3D propagation velocity of any CME, which is propagating in a direction well away from the limb (*eg,* a halo CME). For all other events, we find that ϕ_{SSE} is close to 90° (i.e, the CMEs are near-limb events) and so it is not surprising that the POS speed is more consistent with the 3D speed derived using the FPF, HMF, and SSEF techniques. We also find that, for these near-limb events, the velocities derived using FPF, HMF, and SSEF (which are based on three different underpinning geometries) are in fairly good agreement. Remember, for a limb event, the FP geometry is equivalent to the POS approximation. It is worth repeating here that, with the current implementation of CACTus we do not use any *a priori* information regarding a CME's propagation angle and we cannot estimate the propagation direction in the same way as FPF, SSEF, and HMF techniques as we cannot detect any curvature of the ridges in a time–height map. However, the POS approximation is a good approximation for near-limb events.

6.4 Online automated catalog of SECCHI/HI-1 generated by CACTus

In the sections above, we initially selected eight different days (a three day run, and five individual days) to demonstrate the performance of the revised CACTus algorithm. Using this version of CACTus, we have also generated a full CME catalog, extending from 2007 to 2014, which is available at `http://www.sidc.be/cactus/`

TABLE 6.1: Extract of the CACTus CME catalog for 02–04 April 2010

No.	t_0	CPA	da	NoPA	SuPA	v	dv	minv	maxv
1	02 Apr 2010 05:29	116	12	110	122	459	73	316	498
2	02 Apr 2010 14:09	83	10	78	88	412	25	384	454
3	02 Apr 2010 18:09	104	16	96	112	319	65	229	397
4	03 Apr 2010 12:09	102	72	66	138	823	108	571	1041
5	04 Apr 2010 00:49	124	24	112	136	397	86	350	571

No represents the cluster number (CME number), t_0 is the time of appearance of the CME in the HI-1 FOV, CPA is the central position angle (PA) of the CME (degrees), da is its PA width (degrees), NoPA is its northernmost PA extent (degrees), SuPA is its southernmost PA extent (degrees), v is the median of the maximum value of POS velocity at each PA of the CME (km s^{-1}), dv is the (1 σ) variation of the velocity over the entire PA extent of the CME, minv is lowest value of the maximum velocity and maxv is highest value of the maximum velocity.

TABLE 6.2: Comparison of the number of events

Date	Events Detected by CACTus	Events Detected in Manual catalog
04 Apr 2010	1	0
03 Apr 2010	1	1
02 Apr 2010	3	0
12 Dec 2008	1	1
26 Apr 2008	2	1
04 Feb 2008	1	1
22 Oct 2007	1	1
19 Apr 2007	1	1

`hi` and `http://www.helcats-fp7.eu/catalogues/wp2_cactus.html`. The methodology employed to generate the full catalog (i.e, the thresholds in intensity, etc) is identical to what has been described above, except that the analysis is performed on intervals of one month duration, which overlap by one day in order to accommodate CMEs, which span the month boundary. A limit of one month is imposed for computational reasons. It is important to note that the length of time interval, which we incorporate into a single CACTus analysis run, will affect the detection and/or returned parameters of a CME, since the intensity threshold in

TABLE 6.3: Comparison of CACTus vs. Manual Detection

CACTus				Manual						
t_0	CPA	da	v	t_0	CPA	da	v_{SSE}	ϕ_{SSE}	v_{FP}	v_{HM}
03 Apr 2010 12:09	102	72	843	03 Apr 2010 12:09	102	105	927	77	889	962
12 Dec 2008 15:29	77	70	469	12 Dec 2008 15:29	77	95	426	69	419	431
26 Apr 2008 18:09	82	72	595	26 Apr 2008 18:49	85	110	649	95	620	679
04 Feb 2008 14:09	83	66	448	04 Feb 2008 14:09	77	115	511	53	506	515
22 Oct 2007 14:49	84	68	225	22 Oct 2007 14:49	77	85	691	174	499	748
19 Apr 2007 11:30	90	72	376	19 Apr 2007 13:30	90	100	392	61	389	393

v_{SSE} is the speed in km s^{-1} and ϕ_{SSE} is the spacecraft-Sun-CME angle in degrees derived using SSEF (Davies *et al.* 2012). If ϕ_{SSE} is close to 90° then the CME originated from near the limb. If ϕ_{SSE} is close to 0° or 180° then CME is a front or backsided halo, respectively, as seen from the STEREO-A spacecraft. v_{FP} and v_{HM} are the speed in km s^{-1} derived using FPF and HMF, respectively.

accumulator space (W_{thresh}) depends on W_{mean} and W_{sd}, both of which depend on the duration of the analysed interval. We choose 15 different "good" and "fair" quality CMEs from the HELCATS manual catalog, from different times between 2007 and 2013 and with a range of values of ϕ_{SSE} (see Table 6.4). Table 6.4 also includes the events listed in Table 6.3 (shown in boldface).

- *Comparison with CMEs discussed in Section 6.3*: To demonstrate the effect of the length of the analysed interval, we compare the results for the six CMEs listed in Table 6.3 with their entries in the online CACTus catalog. The dates and times of these CMEs are highlighted in boldface in Table 6.4. We note that there are, obviously, some differences that arise when an interval of one month is incorporated in a single analysis.
  - Of the six CMEs listed in Table 6.3, the times of appearance of four match well with their counterparts listed in Table 6.4 (in boldface). For the other two CMEs, there is a difference of two frames (corresponding to 80 minutes). As discussed above, this may be attributed to the

different thresholds resulting from the analysis of different lengths of data.

– Out of the six CMEs listed in Table 6.3, the PA widths of the CMEs detected on 03 April 2010 and 19 April 2007 match well with those listed in Table 6.4. For the CMEs detected on 04 February 2008 and 22 October 2007, the PA width quoted in Table 6.4 is less than the PA width quoted in Table 6.3. On closer inspection, we find that, when using a longer analysis interval, each of these CMEs was identified as two separate (narrower) CMEs. Reanalysis results in the CME on 04 February 2008 being identified as two separate CME, because the leading edge of the CME is poorly defined. We suggest that, in this case, the slight change in the intensity threshold due to the longer analysis interval results in the points in accumulator space not being joined up under the application of the morphological closing technique. Hence, the algorithm detects two narrower CMEs instead of a single wider one. Finally, for the CMEs detected on 12 December 2008 and 26 April 2008, the PA widths of the CMEs in Table 6.4 are greater than their counterparts in Table 6.3. This can also be explained in terms of there being a different threshold due to increased length of the analysed data set, which results in the inclusion of additional material (possibly the CME flanks or adjacent structures). For these two CMEs, the PA widths quoted in the online CACTus catalog are actually much more consistent with those in the manual catalog.

– Different lengths of analysis intervals will clearly also result in different CME velocities. CACTus computes the maximum velocity in each PA bin within a CME. The velocity listed in the online CACTus catalog is the median of all these maximum velocities. The median is likely to change if the PA width of the CME changes. Moreover, a different threshold is likely to give rise to a different estimate of the maximum velocity at a given PA (see Section 6.2.4). It is likely that both of

these effects would contribute to differences in the CME velocities if the length of the analysis interval is modified significantly. However, we find that the differences in the velocities of the common CMEs in Table 6.3 and Table 6.4 are within one standard deviation (dv, quoted in Table 6.1).

It is difficult to ascertain whether it is better to analyse individual days (or short intervals) or longer periods of data (such as a month). However, it is important to employ a consistent methodology. Therefore, for in the generation of the online catalog, we incorporate one month of data into each CACTus run from 2007 to 2014.

- *Comparison with manual catalog*: Here, we compare the online CACTus catalog with the manual catalog. We compare every event listed in both manual and automated catalogs on the selected days. A detailed comparison between the manual and the automated catalogs will be presented in future studies.

  – The times of CME appearance in the two catalogs differ at most by three frames (2 hours). In Section 6.3.3, we have compared the manual and automatically derived parameters of the CME, which entered the FOV of HI-1 on STEREO-A on 19 April 2007. The times at which the CME on 26 April 2008 was first detected by CACTus is two hours earlier than its manual catalog entry. We suggest that this discrepancy is due to the outflow of associated material prior to the CME itself (see animated Figure 6.9 available online). Sometimes the leading edge of a CME is faint or not well defined, for example the CME on 26 February 2011, which makes it difficult to estimate accurately its time of first appearance in the FOV (see animated Figure 6.10 available online). For some CMEs, the times of appearance match very well in both the automated and manual catalogs. Such events tend to have bright, clear leading edges (for example the CME on 27 February 2013) and/or are

preceded by outflows, which are faint enough not to be detected by CACTus (see animated Figure 6.7 available online). In general, we suggest that CACTus tends to detect CMEs either at the same time or slightly earlier than is estimated by manual operators.

- In general, CACTus tends to produce a lower estimate of the PA width than that included in the manual catalog for the same event. As noted previously, this can be due to the misdetection by CACTus of a single CME as two narrower events or can be due to the fact that CMEs flanks can be faint and can sometimes move non-radially.
- Velocities estimated by CACTus tend to match well with v_{FP} in the HELCATS manual catalog for limb/near-limb CMEs (those with ϕ_{SSE} close to 90°).
- For the days considered in Table 6.4, we find that CACTus detects a total of 18 events. The manual catalog includes only 15 events, meaning that CACTus detects 3 events, which are not listed in the manual catalog. One of these additional events (on 27 February 2013) is due to CACTus identifying, as a separate CME, pre-CME outflows. Another is due to the erroneous splitting of a single CME into two (22 October 2007). Finally, one narrow CME is also identified, which is not listed in the manual catalog as it is narrower than the PA width threshold of 20° imposed in the generation of that catalog.

- *Corotating Interaction Regions (CIRs):* CIRs are the regions of high-density plasma, which form at the interface between the fast and the slow solar wind by compression (Gosling and Pizzo 1999). Rouillard *et al.* (2008) and Sheeley *et al.* (2008a,b) first demonstrated white-light imaging of CIRs in the heliosphere using STEREO/HI. However, the authors suggested that HI was actually observing pre-existing streamer blobs, which had become entrained at the stream interface. Compression of the blobs at the stream interface means that they can be clearly tracked out to 1 AU and beyond.

Although it is thought that this entrainment happens beyond the HI-1 FOV (see Plotnikov *et al.* 2016), we have examined the CACTus output to see if it has detected any of the CIR-associated blobs presented in the literature. We find that CACTus detects some, but not all, of these features. For example, CACTus detects two of the six CIR-associated blobs, which were tracked by Rouillard *et al.* (2010) between 09 September 2007 and 12 September 2007, but none of the six CIR-associated blobs tracked by those authors between 17 and 20 September 2007. Similarly, Tappin and Howard (2009) detected the tracks of several CIR-associated blobs between 14 and 17 November 2011, only one of which was detected by CACTus. The CIR-entrained blobs detected by CACTus have PA widths, which are less than 20°. Therefore, a PA threshold of 20° would likely exclude many such blobs. However, it may also remove some features, which are associated with CMEs. The detection of CIR-associated blobs using CACTus will be the subject of a future study.

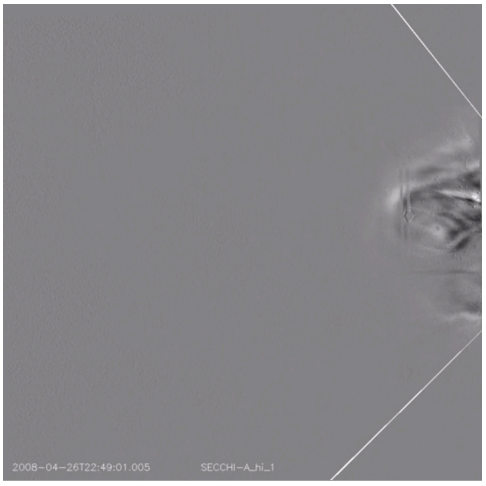

FIGURE 6.9: Movie corresponding to this animated Figure shows the CME moving outward. Pre-CME outflows are clearly seen, which affect the estimation of the time of appearance in HI-1 FOV.
(An animation of this figure is available.)

FIGURE 6.10: Movie corresponding to this animated Figure shows a CME with faint leading edge moving outward. The faint and unstructured leading edge makes the estimation of time of appearance of a CME in HI-1 FOV difficult. (An animation of this figure is available.)

6.5 Summary and Discussion

We have applied, with success, the CACTus algorithm, to automatically detect CMEs in images from the HI-1 camera on board STEREO-A. We performed the analysis on 1 day background-subtracted level 2 data. We have experimented with different background-subtraction methodologies and find it makes little difference because, ultimately, we use polar transformed running difference images for detection using the Hough transform. In summary, the different background-subtraction techniques do not significantly affect the performance of CACTus especially for bright CMEs.

We have also applied this algorithm to HI-1 images from STEREO-B but with less success. The HI-1 camera on STEREO-B suffers from pointing anomalies due, it is now thought, to a small amount of mechanical instability in the attachment of the camera to the HI instrument structure (Brown *et al.* 2009; Davis *et al.* 2012;

TABLE 6.4: Comparison of Online CACTus Catalog with Manually Generated Catalog

CACTus Online				Manual							
t_0	CPA	da	v	t_0	CPA	da	v_{SSE}	ϕ_{SSE}	v_{FP}	v_{HM}	type
13 May 2013 20:09	87	94	745	13 May 2013 20:09	87	135	738	81	705	769	good
27 Feb 2013 15:29	83	82	411	Extra event identified by CACTus.							
27 Feb 2013 10:09	96	88	520	27 Feb 2013 10:09	95	130	597	35	577	612	fair
02 Jul 2012 21:29	115	42	502	02 Jul 2012 20:49	100	100	434	75	426	441	good
06 Feb 2012 02:49	67	46	414	06 Feb 2012 02:49	63	65	410	95	399	420	fair
01 Jun 2011 22:09	88	60	505	01 Jun 2011 22:49	92	85	774	139	667	931	good
26 Feb 2011 04:09	82	64	352	26 Feb 2011 05:29	72	85	389	48	383	392	fair
03 Jun 2010 11:29	88	64	307	03 Jun 2010 12:09	90	120	333	100	320	347	good
03 Apr 2010 12:09	102	72	823	03 Apr 2010 12:09	102	105	927	77	889	962	good
31 Jul 2009 12:49	82	36	334	31 Jul 2009 13:29	40	40	331	70	326	334	fair
09 Jan 2009 07:29	92	48	330	09 Jan 2009 08:49	88	65	522	26	480	570	good
12 Dec 2008 14:09	77	78	475	12 Dec 2008 15:29	77	95	426	69	419	431	good
26 Apr 2008 16:49	91	98	553	26 Apr 2008 18:49	85	110	649	95	620	679	good
04 Feb 2008 14:09	96	40	437	04 Feb 2008 14:09	77	115	511	53	506	515	good
04 Feb 2008 03:29	75	30	505	Not listed in catalog							
22 Oct 2007 19:29	74	24	224	Single event is detected as two different events by CACTus							
22 Oct 2007 14:49	92	20	218	22 Oct 2007 14:49	77	85	691	174	499	748	fair
19 Apr 2007 11:30	91	70	371	19 Apr 2007 13:30	90	100	392	61	389	393	good

Tappin *et al.* 2016). Given the large gradients inherent in the F-corona, which has a much larger white-light signal than that of CMEs, such pointing jitter can result in the presence of a residual F-coronal signal in the STEREO-B HI-1 imagery. This residual signal detrimentally impacts the automatic detection, in particular, of CMEs by CACTus. Hence, more advanced techniques are required to detect CMEs reliably in HI-1 images from STEREO-B. Here, we primarily present the technical details of the detection algorithm, which we implemented within CACTus. Of the eight days initially studied here, three days (02 to 04 April 2010) were analysed as a single run and the remaining five days were analysed individually. Incorporating these five individually analysed days (see Table 6.3) into monthly runs (see Table 6.4) makes little difference to the CACTus results. Any differences are due to the different thresholds, which result from the incorporation of one month data. We also compare a few additional events taken at random from the online CACTus catalog (these encompass both "good" and "fair" CMEs as

defined by the HELCATS manual catalogers). We compared the automatically and manually derived CME properties (see Table 6.4).

We find that, at least over the limited number of days presented in this chapter, CACTus detects more events in HI-1 images than are detected by the manual cataloging. This is due to several factors, which are inherent in the method (the selection of the intensity threshold value and kernel size for morphological closing). In this study, some of the events detected by CACTus are excluded by human operators due to different thresholds in the PA width extent. Manual-cataloging endeavours need to apply a relatively large PA width threshold, which is not necessary with an automated detection routine such as CACTus, simply due to the arduous nature of the manual-cataloging process. It is worth noting that even when we apply objective definitions, there are instrumental factors, which come into play even in automatic CME detection. For example, the apparent brightness of a CME in white-light imagery is dependent to some degree on its location relative to the Thomson sphere. Also, the application of a PA width threshold in order to identify a CME is not entirely consistent as PA width is a projection of a CME's true width onto the POS. Conversely, there are some benefits to a manual as opposed to an entirely algorithmic approach. For example, what is clearly a single CME in the HI imagery on 22 October 2007 (and in the manual catalog) is detected as multiple (two separate) events by CACTus due to the large variation in the brightness over the CME front. In fact, angularly extended faint CME fronts (as characterised in the manual catalog) commonly appear as several narrower CMEs in the CACTus catalog. This tendency for CACTus to overestimate the number of CMEs is also seen in the LASCO and COR2 implementations of CACTus, so it is an intrinsic problem of the method (Robbrecht *et al.* 2009).

We also note that CACTus sometimes computes the time of appearance of a CME to be earlier than it is in the manual catalog. This can be explained by the presence of pre-CME outflows or the lack of well defined and bright leading edge. We feel

that the differences in estimation of the time of first appearance of a CME do not necessarily mean that an automated algorithm is superior to the discretion of manual operators. Rather, it indicates the lack of a proper definition of the time of appearance of a CME.

We find that the PA width of a given CME estimated by CACTus tends to be lower than is listed in the manual catalog. This effect can be exacerbated by the presence of a faint shock around the CME, which is often taken into account by manual catalogers but excluded most of the time by CACTus. This discrepancy in CME width was also present in the earlier version of CACTus (see Robbrecht *et al.* 2009). The difference in width measurement is also due to the lack of a proper definition of the width of a CME. Cremades and Bothmer (2004) reported a difference of a few degrees to more than a hundred degrees when comparing manual catalogs with their measurements. It is still subjective whether or not shocks should be included when estimating the width of a CME. CACTus implements a somewhat more objective criteria for this but, still, the shocks around the flanks of CMEs may or may not be included. The time of CME appearance from CACTus is, on average, earlier than that quoted in the manual catalog. A comprehensive comparison with the manual catalog is underway and will be presented in a future paper.

Currently, CACTus yields only the velocity projected onto the POS as seen from the observing spacecraft. This should be borne in mind when using the speeds derived by CACTus for specific research purposes. Options for retrieving the 3D speed from CACTus may be sought in the future, for example through the inclusion of a more realistic estimate of the propagation direction (such as from GCS or the CAT tools). However, this may pose potential problems, in particular for its real-time implementation. It may also be that CACTus could be optimised to extract the curved ridges in time-elongation maps from heliospheric imaging observations, which extend out to large elongation; these tracks contain information regarding the 3D propagation direction within their curvature.

One distinct advantage of automated detection is that it is not affected by the vagaries of human subjectivity and, hence, the detection of CMEs will be more consistent. As noted above, one disadvantage of this is that it generally results in the detection of many more events than are listed in the manually compiled catalog. However, the number of detected events depends critically on the threshold value of brightness implemented in the program. Optimisation of this value of this threshold for HI imagery will be evaluated in the future versions of CACTus for HI.

To summarise, in this chapter we have described the basic detection algorithm for detecting CMEs in heliospheric imager data using CACTus for the first time. This is of great importance for heliospheric physics. To the best of our knowledge, this is the first report on the successful fully automated detection of CMEs in data from the STEREO heliospheric imager HI-1.

Chapter 7

Kinematics of Fast and Slow Coronal Mass Ejections in solar cycles 23 and 24[†]

7.1 Introduction

Coronal mass ejections (CMEs) consist of plasma and magnetic field that are expelled from the solar atmosphere into the heliosphere at speeds which can range from 100 – 3000 km s^{-1} (Yashiro *et al.* 2004; Gopalswamy *et al.* 2004; Gopalswamy 2010; Manoharan and Mujiber Rahman 2011). They appear as bright, white-light features moving outward in the coronagraph field of view (FOV) (Hundhausen *et al.* 1984; Schwenn 1996). Early observations of CMEs date back to 1970s (Hansen *et al.* 1971). However, Tousey (1973) first observed CMEs in the coronagraph images (see recent review by Gopalswamy 2016, on the history of CMEs). Since the launch of the Large Angle and Spectrometric Corornagraph (LASCO)

[†]Results of this work are under review in Journal of Geophysical Research.

(Brueckner *et al.* 1995) on the Solar and Heliospheric Observatory (SOHO) and Sun Earth Connection Coronal and Heliospheric Investigation (SECCHI) (Howard *et al.* 2008) on the Solar Terrestrial Relation Observatory (STEREO), CMEs have been routinely monitored. Webb and Howard (1994) first reported that the rate of the occurrence of CMEs is correlated with sunspot numbers, type II radio bursts and H-α flares. Significantly large number of CMEs have been reported in solar cycle 24 as compared to solar cycle 23. This effect has been attributed to weak polar field in solar cycle 24 (Luhmann *et al.* 2011; Petrie 2013). However, Wang and Colaninno (2014) reported that the increase in the rate of CMEs in solar cycle 24 is due to the change in the cadence of LASCO images. Thus, they suggested that polar fields may not have significant effect on the CME rate. Gopalswamy *et al.* (2015b) have reported more halo CMEs in solar cycle 24 than solar cycle 23 using the coordinated data analysis workshops (CDAW) catalog. The authors have suggested that the decrease in the total pressure in heliosphere (see Gopalswamy *et al.* 2014) is responsible for higher rate of halo CMEs in solar cycle 24. They also showed that the cadence change has no influence on the higher abundance of halo CMEs in cycle 24. Recently, Petrie (2015) reported that the number of CMEs per sunspot for CMEs, whose widths are greater than 30°, in solar cycle 24 is greater than the number of CME per sunspot in solar cycle 23. In addition to the variation with solar cycle, the width distribution of CMEs follows a power law (Yashiro *et al.* 2006; Robbrecht *et al.* 2009; D'Huys *et al.* 2014).

Motivated by the recent observation that the cycle-to-cycle variation of slow and fast CMEs seem to be width dependent (see Table 1 in Gopalswamy *et al.* 2015a), we investigate the properties of fast and slow CMEs separately and compare them between cycles 23 and 24. The investigation provides important clues to the understanding of the sources of the slow and fast CMEs. We believe that slow and fast CMEs may originate from different sources. We describe the data selection and analysis in Section 7.2. We present the results in Section 7.3 followed by a summary and discussion in Section 7.4.

7.2 Data selection

We use the CDAW and computer aided CME tracking (CACTus) catalogs for the analysis presented in this study. The CDAW catalog lists the properties of CMEs detected manually (Yashiro *et al.* 2004; Gopalswamy *et al.* 2009) in SOHO/LASCO images. CACTus (Robbrecht and Berghmans 2004) generates CME catalog by detecting CMEs automatically in coronagraph images[1]. The solar-cycle variation of CMEs is analyzed with reference to the SIDC monthly average sunspot number.

7.2.1 Selection of fast and slow CMEs

For the analysis, we first remove the "very poor" CMEs from the CDAW catalog. Wang and Colaninno (2014) reported that the detection of "very poor" CMEs is based on the discretion of manual operators, we discard such CMEs in order to remove any bias from our analysis. In the CACTus catalog, we used only "CMEs" detected in coronagraph images and discarded "flows" detected by CACTus because "flows" are considered as the marginal detections (Robbrecht and Berghmans 2004). Note that CACTus does not classify CMEs as "poor" or "very poor" like those listed in CDAW catalog. Furthermore, we impose a lower threshold of 30° on CME width to remove narrow CMEs from CACTus and CDAW catalogs. A threshold of 30° was chosen because the manual detection of CMEs with width <30° is highly subjective (Gopalswamy *et al.* 2010; Yashiro *et al.* 2008). It should be noted that imposing a threshold will remove some of the good events but that will not affect the results presented in this chapter. In addition to a lower threshold, we also impose an upper threshold of 180° on the width because such CMEs mostly suffer from projection effects and thus the width estimation is affected. It is worth noting that CMEs with a width between 40° and 180° also suffer from

[1] `http://sidc.oma.be/cactus`

projection effects. In order to remove projection effects, we also use limb CMEs for the analysis. The selection criteria for limb CMEs is reported in Gopalswamy *et al.* (2014). Moreover, we segregate CMEs as slow and fast based on their speeds. CMEs are usually classified as slow and fast relative to the speed of the solar wind. The slow solar wind typically has speeds less than 400 km s^{-1}, while the fast solar wind has speeds greater 400 km s^{-1} (see, Schwenn 2006). Therefore, 400 km s^{-1} can be taken as the average solar wind speed for a long-term statistical study. We classify CMEs with speeds less than 300 km s^{-1} as slow CMEs and those with speeds greater than 500 km s^{-1} as fast CMEs. CMEs with speeds between 300 km s^{-1} to 500 km s^{-1} are not considered for the analysis because such CMEs cannot be strictly categorised as either slow or fast CMEs because of the uncertainties in the speed measurements. Table 7.1 lists the number of fast and slow CMEs in the CDAW and CACTus catalogs.

7.3 Data analysis and results

Having segregated CMEs in fast and slow, we investigate the width distribution and variation of fast and slow CMEs with solar cycles 23 and 24 using CDAW and CACTus catalogs.

7.3.1 Width distribution

CACTus defines the width of a CME as the maximum angle subtended by the CME at the center of the Sun throughout its propagation (Robbrecht and Berghmans 2004). In the CDAW catalog, the width of a CME is defined as the maximum angle subtended by a CME on the center of the Sun when the CME enters the C3 field of

view (FOV) where the width appears to approach a constant value (Gopalswamy 2004). Figure 7.1 (a) shows the histograms of the width distribution of fast (black line) and slow (blue line) CMEs using CDAW catalog after excluding the "very poor" CMEs. Figure 7.1 (b), shows the width distributions in log scale. Black and blue lines represent the best-fit power laws obtained for fast and slow CMEs, respectively using least square fitting method. The power laws have the form

$$N(W) = CW^{\alpha}, \tag{7.1}$$

where N is the number of CMEs with width W, α is the power law exponent, and C is a constant. We estimate α as -1.3 and -3.8 for fast and slow CMEs respectively. We note that while the fast CMEs follow a power law, the slow CMEs are more log-normally distributed. The curve in red represents the best-fit log-normal curve using least square fitting. To fit a straight line to the width distribution of slow CMEs, we use the width greater than 70° (*i.e,* the tail of the width distribution). Similarly, we estimate the α for slow and fast CMEs as -1.6 and -4.8 using CACTus catalog (see Figure 7.2).

The graphical fitting (GF) of the data points used above is not the best method to estimate the power law, especially when the number of data points is small (D'Huys *et al.* 2016). Therefore, we also use maximum likelihood estimate (MLE) fitting method to derive power law exponent. We perform MLE fitting in two different ways. First, we set the minimum width value, W_m as 30° for fast CMEs and 70° for slow CMEs and estimate the power law index. Second, we derive the minimum width value, W_d for both fast and slow CMEs by minimising the Kolmogorov-Smirnov (KS) distance (see Clauset *et al.* 2007) and estimate the power law index. The second method tells us that beyond W_d, the data points best follow the power law. Table 7.1 lists the power indices estimated using two methods described above for fast and slow CMEs using CDAW and CACTus catalogs.

We also removed the CMEs labelled as "poor" in the CDAW catalog to study

TABLE 7.1: Power law indices of width distribution of fast and slow CMEs obtained using two different methods

Catalog	Total CMEs	Fast CMEs							Slow CMEs						
		Total	GF		MLE				Total	GF		MLE			
			W_m	α	W_m	α_m	W_d	α_d		W_m	α	W_m	α_m	W_d	α_d
CDAW†	19046	3031	30	-1.3	30	-1.13	66	-1.48	4925	70	-3.8	30	-1.8	89	-4.36
CDAW‡	11329	2680	30	-1.1	30	-1.01	66	-1.37	2357	70	-3.7	30	-1.53	80	-3.74
Limb CMEs	531	266	30	-0.4	30	-1	68	-1	169	70	-3.8	30	-1.8	68	-4.16
CACTus	18949	2045	30	-1.6	30	-1.48	70	-2	1956	70	-4.8	30	-2.34	88	-5.71

† CMEs excluding "very poor" CMEs. ‡ CMEs excluding "poor" and "very poor" CMEs. W_m is the minimum width threshold used to fit datasets. α is the power index estimated using graphical fitting (GF) method. α_m is the derived power index using the Maximum likelihood Estimate (MLE) by giving a minimum width threshold, specified by W_m. W_d is the derived minimum width by minimising the Kolmogorov-Smirnov (KS) distance. α_d is the derived power index by applying MLE using minimum width threshold as W_d. Limb CMEs are extracted from the CDAW catalog according to the criteria in Gopalswamy *et al.* (2014).

their effects on the width distribution. It is worth noting that after removing "very poor" and "poor" CMEs from our analysis, we believe that we have removed any bias introduced by manual operators and the effects of large number of poor (faint) CMEs in solar cycle 24 (discussed in Section 7.3.2), respectively. We find that removal of both "poor" and "very poor" CMEs has little effect on the width distribution and power law indices (see Figures 7.1 (c) and (d) and Table 7.1). The speeds listed in the CDAW and CACTus catalogs are the projected speeds in the plane of sky. Therefore, applying a speed threshold uniformly to all CMEs introduces projection effects. In order to remove projection effects, we also estimate the power law for fast and slow limb CMEs in solar cycles 23 and 24. First, we plot CMEs with all velocities whose widths fall between 30–180° (top panel of Figure 7.3). We estimate the power index of limb CMEs as -1.3 and -1.19 using the GF and MLE methods for the minimum width threshold of 30°. Next, we segregate limb CMEs in to fast and slow CMEs and estimate the power indices using the GF (bottom panel of Figure 7.3) and MLE methods (see Table 7.1). We

find that the power indices for fast and slow limb CMEs are different from each other; they are different from the power index of non-limb fast and slow CMEs. One of the reasons for this discrepancy is the small number of slow and fast limb CMEs. From Table 7.1, we note that the fast and slow limb CMEs are 10–20 times less than fast and slow CMEs when non-limb events are also considered. To evaluate the goodness of fit, we estimate the KS distance, which is defined as the maximum distance between the empirical distribution function of the sample and cumulative distribution function of the assumed expression. The KS distances for fast limb CMEs and all fast CMEs are 0.08 and 0.01, respectively. Smaller the KS distance, better is the fit. The critical values of KS distances with 99% of confidence limit for fast limb CMEs and all fast CMEs are 0.12 and 0.04, respectively. Note, the power indices corresponding to the limb CMEs differ from that of non-limb cases. We want to emphasize that the slow CME power law is steeper than that of the fast CMEs in both cases, although the values may differ. However, the limb CME values may be closer to reality because of minimal projection effects. It should be noted that the results are consistent with the speed–width relation as reported in Gopalswamy *et al.* (2014); where authors have reported that wider CMEs tend to propagate faster than narrow CMEs.

7.3.2 Variation of CMEs with solar cycle

Figure 7.4 (a) shows the 12 months smoothed monthly sunspot numbers (SSN) and the occurrence rates of slow and fast CMEs over solar cycles 23 and 24 after excluding "very poor" CMEs from CDAW catalog. We find that the fast CME rates are better correlated with SSN than the slow CME rates. We note that occurrence rate of fast CMEs varies with sunspots, being less in solar cycle 24 than solar cycle 23. However, slow CMEs follow an opposite trend. Even though there are less sunspots in solar cycle 24 than solar cycle 23, there are more slow

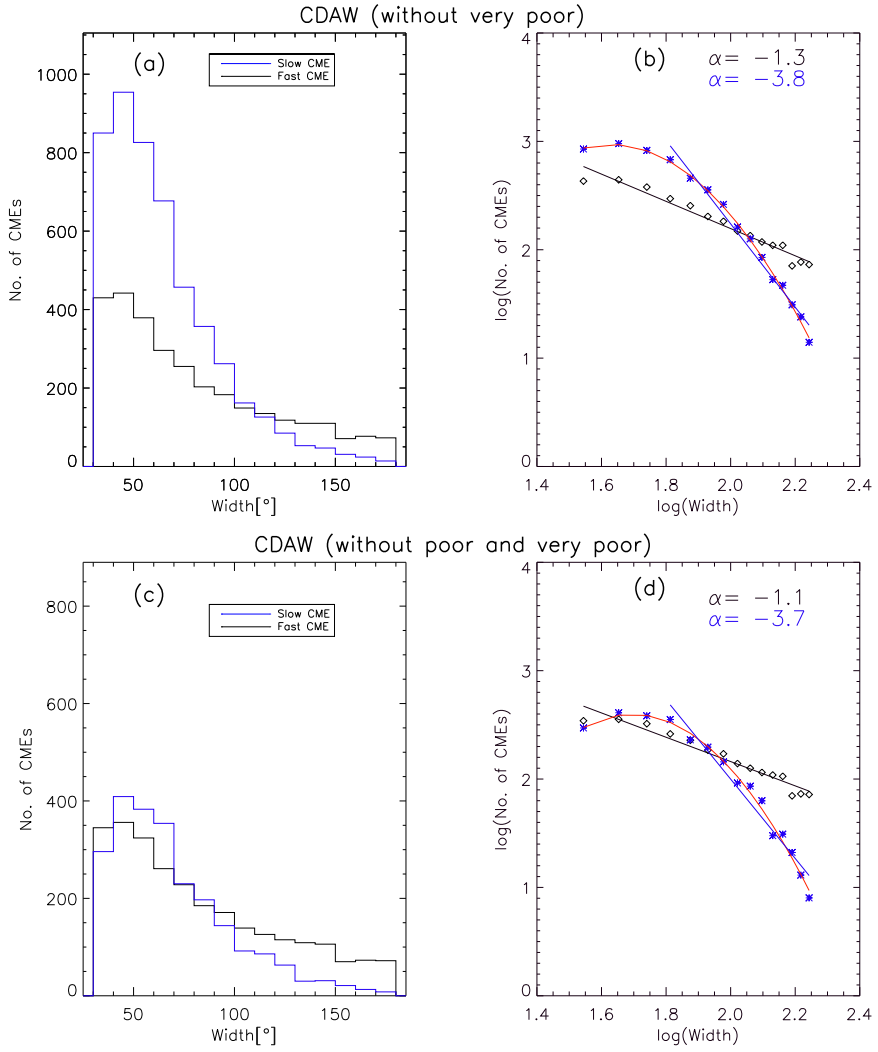

FIGURE 7.1: *Top*: (a): Width distribution and, (b): log distribution of width for Slow and fast CMEs using CDAW catalog after excluding "very poor" CMEs. The best fit straight line to the data points of fast CMEs is overplotted in black. The best fit straight line to the data points (except first three points) of slow CMEs is overplotted in blue. Curve in red represents the best fit log-normally distributed curve. (c) and (d) using CDAW catalog after excluding "poor" and "very poor" CMEs.

CMEs in solar cycle 24. Moreover, the occurrence rate of fast CMEs show a clear double peak behaviour in solar cycles 23 and 24, while the slow CMEs show double peak behaviour only in solar cycle 24. Furthermore, the second peak of cycle 24 has less fast CMEs and more slow CMEs as compared to the first peak. Another fact worth noting from Figure 7.3 is that there is a time lag between the occurrence rate of monthly SSN and fast CMEs in solar cycle 23 (note the time of double peak

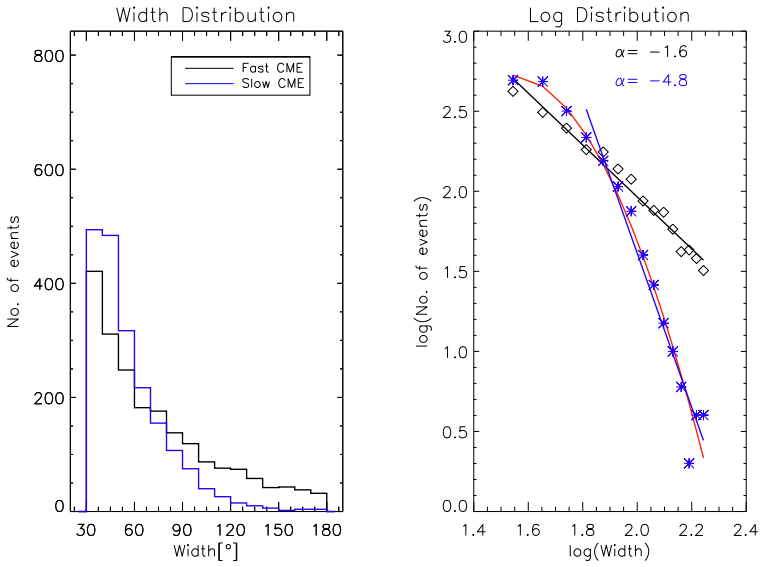

FIGURE 7.2: Width distribution of slow and fast CMEs using CACTus catalog.

in fast CMEs and SSN) but not in solar cycle 24.

Figure 7.3 (b) shows the variation of the occurrence rates of slow and fast CMEs with solar cycle after excluding both "poor" and "very poor" CMEs. Occurrence rates both slow and fast CMEs are now correlated with SSN. We find that there are more slow CMEs in the beginning of a solar cycle. It should be noted that these are not the faint and narrow CMEs but wide and bright CMEs. As the cycle progresses towards solar maximum, the occurrence rate of fast CMEs increases. Towards the end of the solar cycle, again the occurrence rates of slow CMEs become higher than those of fast CMEs. This effect is consistent in both cycles.

Next, we study the variation of "poor" CMEs with solar cycle. Only the "poor" CMEs with width greater than 30° and less than 180° and speeds less than 300 km s^{-1} and greater than 500 km s^{-1} have affected the variation of the occurrences of fast and slow CMEs shown in Figure 7.4 (a). Figure 7.5 shows the variation of the occurrences of fast and slow "poor" CMEs with solar cycle. First, we observe that the "poor" CMEs consist of more slow CMEs than fast CMEs. Next, we find that the rate of fast and "poor" CMEs vary with solar cycle and are not enhanced in solar cycle 24, while the rate of slow and "poor" CMEs are higher in solar cycle 24 than in cycle 23. We note that the occurrence rates of slow and "poor" CMEs

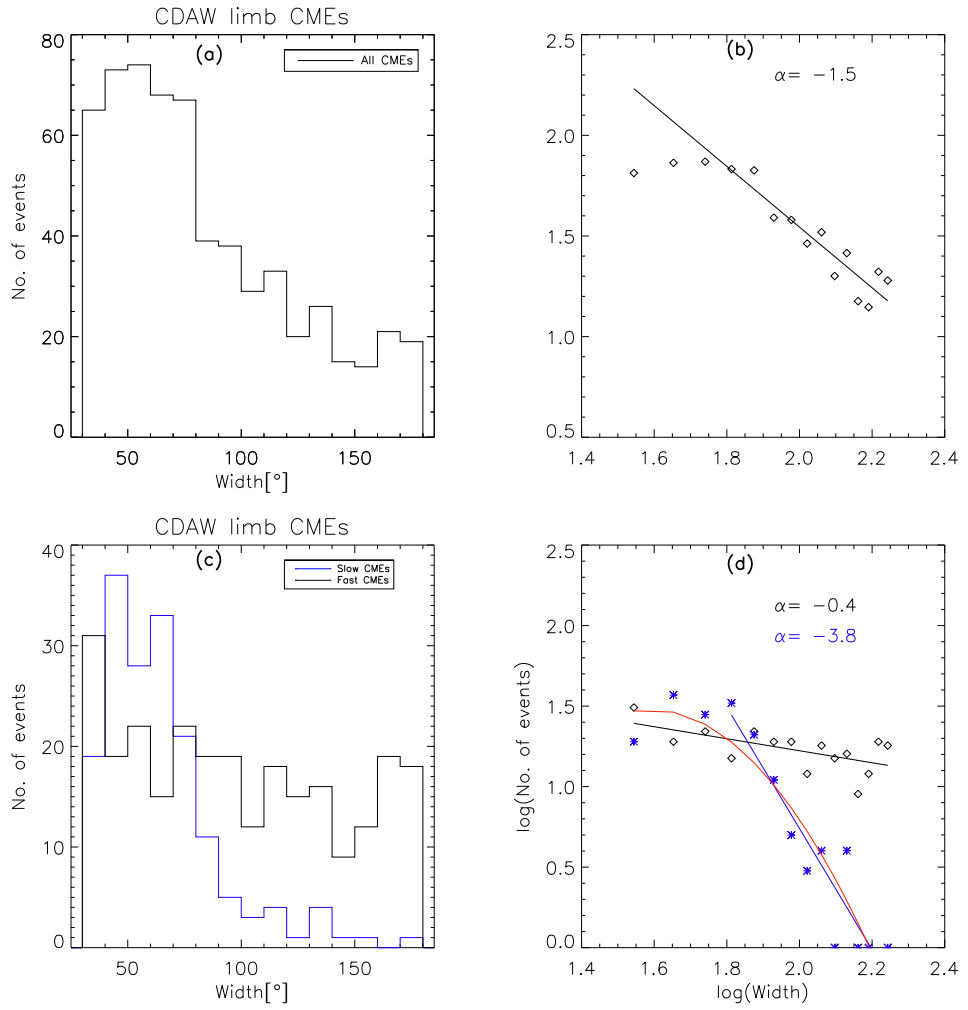

FIGURE 7.3: Width distribution for limb CMEs extracted from CDAW catalog. Top: Width distribution without velocity thresholding. Bottom: Width distribution of slow and fast CMEs.

show double peak in solar cycle 24. We believe that unlike "very poor" CMEs whose rate suddenly increases in during the solar cycle 23 minima (see, Wang and Colaninno 2014), the rate of "poor" CMEs does not change suddenly. Rather the change is gradual and it also follows SSN with the exception that in solar cycle 24 the rate has increased substantially. One should remember that a CME is listed as "poor" based on its intensity in the coronagraph difference images. Should there be any human subjectivity, it should influence the rates of both fast and slow "poor" CMEs. Since there is no substantial increase in the rates of fast and "poor" CMEs in solar cycle 24, we believe that "poor" CMEs are not affected by

subjectivity of human operators. Since a CME is termed as "poor" independent of its velocity thus we expect that slow CMEs also should not be affected by human subjectivity. Thus we believe that the occurrence rates of slow and "poor" CMEs have increased substantially in solar cycle 24 and the increase in the rate of occurrences is not due to human subjectivity.

We also use CACTus catalog to study the variation of the occurrence rate of CMEs with solar cycle because the detection of CMEs by CACTus is more objective. Figure 7.6 (a) shows the occurrence rates of slow and fast CMEs over solar cycles 23 and 24 and 12 months smoothed SSN. Using CACTus catalog, we note the rate of slow CMEs in cycle 24 is greater than cycle 23 similar to that seen using CDAW catalog after removing "very poor" CMEs (see Figure 7.4 (a)). Since the detection by the CACTus catalog is more objective, it allowed us to propose that the rate of slow and wide CMEs have indeed increased in solar cycle 24. Recently it has been suggested that the detection by automated catalogs can be affected by the change in the cadence of the LASCO after 2010. The cadence of LASCO post 2010 has almost doubled. To quantify the effect of change in LASCO cadence on the rate of the occurrences of the CMEs, we run CACTus on the LASCO images taken after 2010, discarding every alternate image. This effort is made in order to make the cadence of LASCO post 2010 equal to the cadence before 2010. Though, after resampling the LASCO cadence, total number of CMEs per month detected by CACTus has reduced but the change of cadence has very little effect on the occurrence rates slow and fast CMEs. It could be because we have already removed narrow CMEs (width $< 30^{\circ}$) from the CACTus catalog. Figure 7.6 (b) shows the occurrence rate of slow and fast CMEs using resampled CACTus catalog. The work is still under progress thus we have created catalog up to December, 2013 only. It is clearly seen from Figure 7.6 (b) that the increase in cadence has little effect on the occurrence rates of fast and slow CMEs.

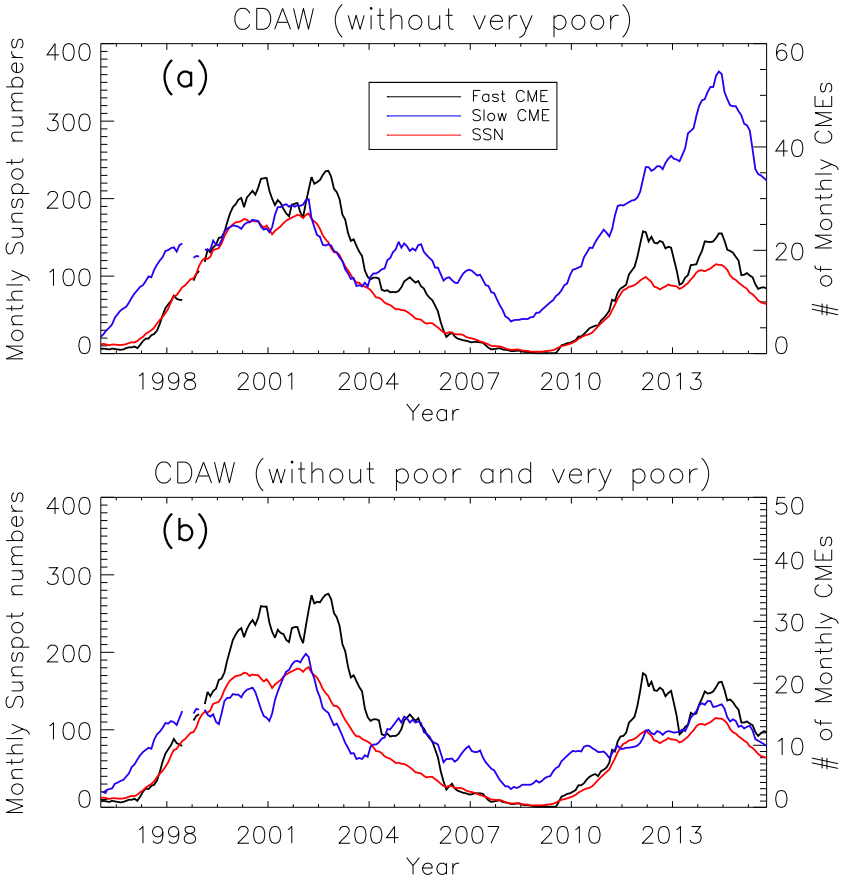

FIGURE 7.4: (a) Variation of SSN and occurrence rates of monthly CMEs smoothed over 12 months using CDAW (without "very poor" CMEs) catalog. (b) Same as (a) but excluding "poor" and "very poor" CMEs

7.4 Summary and Discussion

In this chapter, we studied the properties of slow ($\leq$ 300 km s^{-1}) and fast CMEs ($\geq$ 500 km s^{-1}) in solar cycle 23 and 24 using CDAW and CACTus catalogs. The key finding are listed below.

1. Fast and slow CMEs follow different power laws in width distribution. This effect is persistent even when "poor" and "very poor" CMEs are removed from CDAW catalog (which is done in an attempt to remove the human subjectivity and effects of the large number of "poor" events in cycle 24,

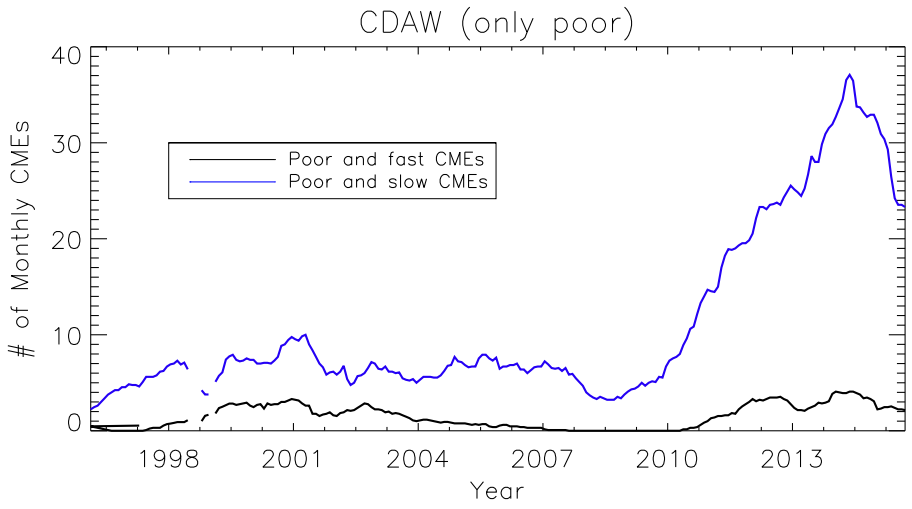

FIGURE 7.5: Variation of the occurrences of fast and slow "poor" CMEs extracted from CDAW catalog smoothed over 12 months.

respectively). The slow CMEs are distributed more log-normally than the fast CMEs. Using MLE, we find that the width of slow and fast CMEs follow a power law when their widths are beyond 88° and 66° respectively. While the power index of fast CMEs is comparable to that of the flare energy distribution (Crosby *et al.* 1993); the power index of slow CMEs is too steep to be explained in terms of flare energy distributions. We find a similar behaviour using both manual (CDAW) and automated (CACTus) catalogs. Thus, we think that it is not due to difference in the measurements made in different catalogs.

2. We find different power indices for fast and slow limb CMEs. However, the absolute value of power indices are not same as compared to limb and non-limb CMEs which may be due to poor statistics, as demonstrated by KS test. Since both fast and slow limb and non-limb CMEs follow different power laws in width distribution, we believe that slow and fast CMEs may have different energy sources and generation mechanisms. We conjecture that the fast CMEs are probably associated with active prominences while slow CMEs are associated with quiescent prominences.

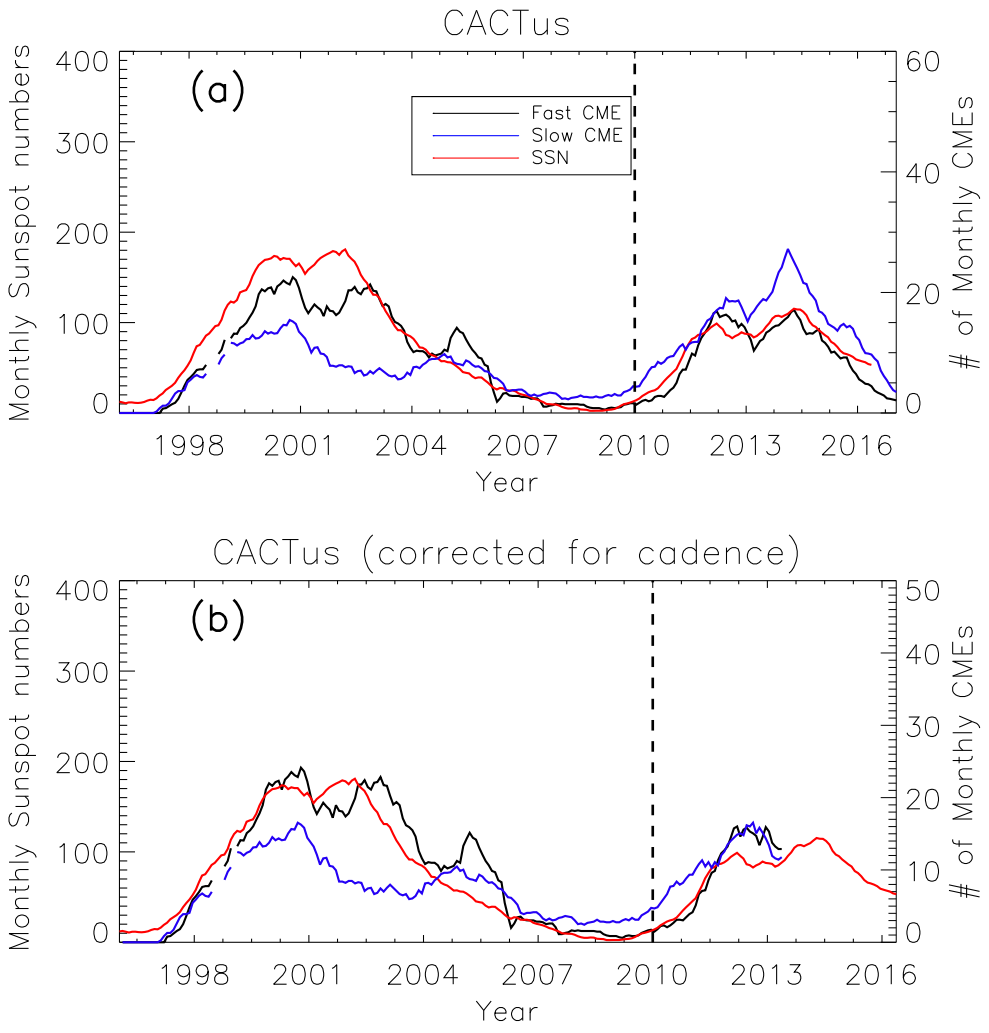

FIGURE 7.6: Variation of the occurrences of fast and slow CMEs extracted from CACTus catalog smoothed over 12 months. Vertical dashed line represents the time beyond which LASCO cadence was increased.

3. The occurrence rates of fast CMEs are better correlated with SSN than those of the slow CMEs using CDAW catalog when "poor" events are not excluded and using CACTus catalog, which suggests that fast CMEs are closely associated with sunspots than slow CMEs. We also find that the occurrence rate of fast CMEs show double peak in both solar cycles as demonstrated by using both catalogs. The occurrence rate of slow CMEs show double peak behaviour only in solar cycle 24. Thus we believe that the slow CMEs were not largely associated with sunspots in solar cycle 23 but they are associated with sunspots in solar cycle 24. We find that the rate of occurrences of both

slow and fast CMEs become less in solar cycle 24 when "poor" events are excluded. During the start and towards the end of a solar cycle, rate of slow CMEs is higher while during the maxima, rate of fast CMEs is higher.

4. The number of slow and "poor" CMEs has increased in the current solar cycle compared to that in cycle 23. Using manual and automated catalogs, Wang and Colaninno (2014) have reported that total number of CMEs are less in solar cycle 24 than in solar cycle 23 and reported that weak polar fields have little role to play in increasing the number of CMEs. In this study, using manual catalog, we find that it is the occurrence rate of slow and "poor" CMEs that has increased, while the occurrence rate of slow and bright CMEs and fast CMEs has decreased in cycle 24. Using CACTus catalog, we find that the rate of slow CMEs have increased in solar cycle 24. CACTus does not classify a CME as "poor" or "very poor" like CDAW catalog. Thus it may be possible that the "poor" and slow CMEs as segregated from CDAW catalog are included in CACTus catalog. This leads us to believe that the weak polar and heliospheric field affects only the occurrences of slow CMEs. They have little or no effect on the occurrences of fast CMEs.

Chapter 8

Conclusions

Properties of small and large scale transients in different layers of the solar atmosphere were studied in this thesis. The dynamics and interaction of small-scale transients with magnetic structures present in the solar atmosphere were examined. Long-term variation of large-scale transients and their possible effects on space weather were explored. In this chapter, I will summarise the main results of the studies presented in this thesis. I will also outline the recent developments in the field and possible future prospects.

8.1 Main Findings and Future Prospects

- *Nature of PDs and their sources*: We presented an observational evidence of the association of small-scale transients such as TR jets (jet-like features) with slow waves (PDs) propagating along a plume. An on-disk plume was studied using the data obtained from IRIS, AIA and HMI. The asymmetric spectral line profiles, enhanced line widths and large Doppler velocities were observed at the locations co-temporal and co-spatial with the underlying

magnetic flux change. This led us to believe that the brightenings seen in IRIS spectra are most likely due to outflows. Furthermore, several jet-like features (TR jets) in the IRIS SJIs were noted. One–to–one correspondence between jet-like features and PDs were found at several instances which allowed us to propose that the jet-like features in transition region might be producing propagating slow waves seen in the corona. We found that the velocity distribution of the jet-like features peaked at 10 km s^{-1}, which is the typical sound speed in the chromosphere. Our results support the interpretations of Wang *et al.* (2013). These authors reported that tiny upflows at the footpoints of a loop excite PDs along the loop. Following our study, several other authors have also reported the association of PDs seen in corona and jets in the chromosphere and transition region. Jiao *et al.* (2015) and Samanta *et al.* (2015) studied the sources of quasi-periodic PDs. Samanta *et al.* (2015) proposed that both spicules and PDs are generated by a common process such as magnetic reconnection. Recently, Bryans *et al.* (2016) reported that both shock waves and flows are associated with the footpoints of PDs.

Our study combined with recent studies have greatly improved our understanding of the sources of PDs. However, the studies mentioned above were confined to polar and on-disk plumes. Thus, further statistical studies on closed loops and fan loops are needed to confirm that both wave and flows are the sources of the PDs seen in different coronal structures. Moreover, it is not clearly understood that whether shock waves and flows at the footpoints of PDs generate waves or they are generated by a common process. Subsequent studies with better temporal and spatial resolution are needed to confirm or reject the above scenarios.

- *Transient as a driver of kink oscillations*: Recently, it was reported that most of the kink oscillations are associated with low coronal eruptions such as CMEs, magnetic flux rope, and a system of magnetic loops (Zimovets and Nakariakov 2015a). The kink oscillations in coronal loops excited by a

coronal jet were not reported in the earlier studies. We examined the role of a small-scale coronal transient such as coronal jet in exciting transverse waves in a coronal loop by combining the observations taken from AIA/SDO and EUVI/STEREO. The jet under study consisted of hot and cool components. The jet interacted with the loop and excited large amplitude and long period transverse oscillations. The magnetic field strength estimated was less than a typical value of magnetic field inside a coronal loop because the coronal loop was not an active region coronal loop. The kinetic energy of the jet was found to be high enough to excite the transverse oscillations in the coronal loop. Our study has demonstrated that a transient such as coronal jet can excite oscillations in a coronal loop. However, this is one individual study of the excitation of kink oscillations in the coronal loops by a nearby jet and excitation mechanism of the kink oscillations are still not very well understood. Thus exploring the excitation mechanism holds a promising future. There could be many more small-scale transients responsible for the kink oscillations but they are not yet discovered due to observational limitations. For example, the role of the coronal rain blobs in exciting the kink oscillations in active region loops is still not well understood. Recently, there have been several reports of decayless kink oscillations. A continuous driver is needed to sustain such oscillations. The excitation mechanisms of such oscillations are also not well understood. More detailed studies with high spatial and temporal resolutions can reveal new transient structures that may excite kink oscillations in the solar corona.

- *Standing oscillations in cool fan loops*: Standing oscillations have been exclusively reported in hot and flaring coronal loops. They are believed to be excited by flares happening at the footpoint of a coronal loop. We studied the interaction between a large-scale coronal transient such as blast wave and nearby coronal fan loops and found that the blast waves excited slow standing waves in these loops. We reported a different excitation and reflection mechanism of the standing slow waves in cool fan loops ($T < 1$ MK).

We proposed that the antinode of the oscillations was either present at the footpoint away from the active region or at the location of the sharp density gradient. We found signatures of weak damping of the standing waves at few locations along the fan loops. We suggested that the weak damping of the oscillations might be most likely due to the inefficient thermal conduction. It is yet to be explored whether standing waves excited by blast waves are also found in other coronal structures with diverging magnetic field topology such as coronal plumes.

- *Monitoring CMEs in the heliosphere*: CMEs cause geomagnetic storms, thus they affect the space weather. Therefore, CMEs should be monitored in real time in coronagraph images. Monitoring halo CMEs helps in predicting their arrival times on the Earth. Though, there exist several automatic methods to detect CMEs in coronagraph images, none exits for detecting CMEs in the heliospheric images. We designed an automated algorithm to monitor the CMEs in the heliosphere using data from HI-1/STEREO. The algorithm is based on the CACTus package, conventionally applied to the coronagraph images. The algorithm works on the principle of Hough transform that detects straight ridges in an image. We demonstrated that the algorithm successfully detects the CMEs in the heliosphere. The advantage of the algorithm is that it is faster, more objective and successfully detects CMEs in HI-1 images. One disadvantage is that it estimates the speeds of the CMEs projected in the plane-of-sky. It does not calculate the true speed of the propagation of a CME. We did not implement this algorithm in HI-2 because the ridges in the time-elongation maps created using HI-2 data are curved due to large elongations. In future, we are planning to improve the speed estimation by using generalised Hough transform to detect arbitrary shapes in an image. Generalised Hough transform can detect curved ridges in time-elongation maps which will enable us to estimate the true speed of a CME and detect CMEs in HI-2 imagery.

- *Kinematics of slow and fast CMEs*: The rate of the occurrences of CMEs is well correlated with solar cycles. It was reported using CDAW catalog that solar cycle 24 is producing more CMEs than solar cycle 23 despite fewer sunspot numbers in solar cycle 24. The properties of fast and slow CMEs have not been studied separately in greater detail. Motivated by the recent studies on the variation of occurrence rates of CMEs in last two solar cycles, we studied the kinematics of slow and fast CMEs separately in solar cycle 23 and 24. The major result from this study was that slow and fast CMEs have different width distribution. It is well established that width distribution of CMEs follows a power law. We found that fast and slow CMEs have different power indices. Slow CMEs have much steeper distribution than the fast CMEs. This allowed us to conjecture that fast and slow CMEs have different energy sources. Our findings support the results of St. Cyr *et al.* (1999). These authors reported that on average slow CMEs were associated with the solitary prominences and fast CMEs were associated with the active regions. In future, the sources of the slow and fast CMEs can be probed in the atmosphere of the Sun using full-disk observations.

  Using CDAW and CACTus catalogs, we noted that the occurrence rate of fast CMEs are well correlated with sunspot numbers and hence the occurrence rate of fast CMEs are less in solar cycle 24 as compared to solar cycle 23. While the occurrence rate of slow and poor CMEs are more in solar cycle 24 as compared to solar cycle 23. We conjectured that increase in the rate of occurrences of slow and poor CMEs is due to the weak heliospheric field in solar cycle 24. Our study suggested that a weaker solar cycle can be associated with more slow and wide CMEs as compared to other strong cycles. Such CMEs may also become halo because of weak heliospheric field associated with weaker cycles and they may disturb the Earth's magnetosphere. It is still not properly understood that why the occurrence rate of slow CMEs are more in solar cycle 24. Some indication of the effect of polar fields on the occurrence rate of CMEs was given by Petrie (2013, 2015). It

can be further explored in future using MHD modelling techniques which may improve our understanding about the occurrences and geo-effectiveness of slow and poor CMEs.

With the advent of space-based instruments in the past decade, our understanding of the properties of transients in solar atmosphere has greatly improved. The upcoming space-based facilities such as Solar Probe Plus, ADITYA, PROBA3 etc will further advance our knowledge about the interaction of the transients with different coronal structures and their effects on the space weather.

Bibliography

Anfinogentov, S. A., Nakariakov, V. M. and Nisticò, G., 2015, "Decayless low-amplitude kink oscillations: a common phenomenon in the solar corona?", *Astron. Astrophys.*, **583**, A136. [DOI], [ADS], [arXiv:1509.05519 [astro-ph.SR]]

Aschwanden, M. J., 2006, "Coronal magnetohydrodynamic waves and oscillations: observations and quests", *Philosophical Transactions of the Royal Society of London Series A*, **364**, 417–432. [DOI], [ADS]

Aschwanden, M. J. and Schrijver, C. J., 2011, "Coronal Loop Oscillations Observed with Atmospheric Imaging AssemblyKink Mode with Cross-sectional and Density Oscillations", *Astrophys. J.*, **736**, 102. [DOI], [ADS], [arXiv:1105.2191 [astro-ph.SR]]

Aschwanden, M. J., Fletcher, L., Schrijver, C. J. and Alexander, D., 1999, "Coronal Loop Oscillations Observed with the Transition Region and Coronal Explorer", *Astrophys. J.*, **520**, 880–894. [DOI], [ADS]

Aschwanden, M. J., de Pontieu, B., Schrijver, C. J. and Title, A. M., 2002, "Transverse Oscillations in Coronal Loops Observed with TRACE II. Measurements of Geometric and Physical Parameters", *Solar Phys.*, **206**, 99–132. [DOI], [ADS]

Aschwanden, M. J., Boerner, P., Schrijver, C. J. and Malanushenko, A., 2013, "Automated Temperature and Emission Measure Analysis of Coronal Loops and Active Regions Observed with the Atmospheric Imaging Assembly on the Solar Dynamics Observatory (SDO/AIA)", *Solar Phys.*, **283**, 5–30. [DOI], [ADS]

Banerjee, D., O'Shea, E. and Doyle, J. G., 2000, "Long-Period Oscillations in Polar Plumes as Observed by cds on Soho", *Solar Phys.*, **196**, 63–78. [ADS]

Banerjee, D., O'Shea, E., Doyle, J. G. and Goossens, M., 2001, "Long period oscillations in the inter-plume regions of the Sun", *Astron. Astrophys.*, **377**, 691–700. [DOI], [ADS]

Banerjee, D., Teriaca, L., Gupta, G. R., Imada, S., Stenborg, G. and Solanki, S. K., 2009, "Propagating waves in polar coronal holes as seen by SUMER & EIS", *Astron. Astrophys.*, **499**, L29–L32. [DOI], [ADS], [arXiv:0905.1013 [astro-ph.SR]]

Barnard, L., Scott, C., Owens, M., Lockwood, M., Tucker-Hood, K., Thomas, S., Crothers, S., Davies, J. A., Harrison, R., Lintott, C., Simpson, R., O'Donnell, J., Smith, A. M., Waterson, N., Bamford, S., Romeo, F., Kukula, M., Owens, B., Savani, N., Wilkinson, J., Baeten, E., Poeffel, L. and Harder, B., 2014, "The Solar Stormwatch CME catalogue: Results from the first space weather citizen science project", *Space Weather*, **12**, 657–674. [DOI], [ADS]

Barnard, L., Scott, C. J., Owens, M., Lockwood, M., Crothers, S. R., Davies, J. A. and Harrison, R. A., 2015, "Differences between the CME fronts tracked by an expert, an automated algorithm, and the Solar Stormwatch project", *Space Weather*, **13**, 709–725. [DOI], [ADS]

Beckers, J. M., 1968, "Solar Spicules (Invited Review Paper)", *Solar Phys.*, **3**, 367–433. [DOI], [ADS]

Berghmans, D., Clette, F., Robbrecht, E. and McKenzie, D., 1999, "Multi-Imager Study of Transients and Propagating Disturbances in Active Region Loops (SOHO JOP80 Campaign)", in *Magnetic Fields and Solar Processes*, (Eds.) Wilson, A., et al., ESA Special Publication, 448, [ADS]

Bisi, M. M., Harrison, R. A., Lugaz, N., van Driel-Gesztelyi, L. and Mandrini, C. H., 2013, "Observations and Modelling of the Inner Heliosphere: Preface and Tribute to the Late Dr. Andy Breen", *Solar Phys.*, **285**, 1–7. [DOI], [ADS]

Bohlin, J. D., Vogel, S. N., Purcell, J. D., Sheeley, Jr., N. R., Tousey, R. and Vanhoosier, M. E., 1975, "A newly observed solar feature - Macrospicules in He II 304 A", *Astrophys. J. Lett.*, **197**, L133–L135. [DOI], [ADS]

Bougeret, J. L., Goetz, K., Kaiser, M. L., Bale, S. D., Kellogg, P. J., Maksimovic, M., Monge, N., Monson, S. J., Astier, P. L., Davy, S., Dekkali, M., Hinze, J. J., Manning, R. E., Aguilar-Rodriguez, E., Bonnin, X., Briand, C., Cairns, I. H., Cattell, C. A., Cecconi, B., Eastwood, J., Ergun, R. E., Fainberg, J., Hoang, S., Huttunen, K. E. J., Krucker, S., Lecacheux, A., MacDowall, R. J., Macher, W., Mangeney, A., Meetre, C. A., Moussas, X., Nguyen, Q. N., Oswald, T. H., Pulupa, M., Reiner, M. J., Robinson, P. A., Rucker, H., Salem, C., Santolik, O., Silvis, J. M., Ullrich, R., Zarka, P. and Zouganelis, I., 2008, "S/WAVES: The Radio and Plasma Wave Investigation on the STEREO Mission", *Space Sci. Rev.*, **136**, 487–528. [DOI], [ADS]

Boursier, Y., Lamy, P., Llebaria, A., Goudail, F. and Robelus, S., 2009, "The ARTEMIS Catalog of LASCO Coronal Mass Ejections. Automatic Recognition of Transient Events and Marseille Inventory from Synoptic maps", *Solar Phys.*, **257**, 125–147. [DOI], [ADS]

Brown, D. S., Bewsher, D. and Eyles, C. J., 2009, "Calibrating the Pointing and Optical Parameters of the STEREO Heliospheric Imagers", *Solar Phys.*, **254**, 185–225. [DOI], [ADS]

Brueckner, G. E. and Bartoe, J.-D. F., 1983, "Observations of high-energy jets in the corona above the quiet sun, the heating of the corona, and the acceleration of the solar wind", *Astrophys. J.*, **272**, 329–348. [DOI], [ADS]

Brueckner, G. E., Howard, R. A., Koomen, M. J., Korendyke, C. M., Michels, D. J., Moses, J. D., Socker, D. G., Dere, K. P., Lamy, P. L., Llebaria, A., Bout, M. V., Schwenn, R., Simnett, G. M., Bedford, D. K. and Eyles, C. J., 1995, "The Large Angle Spectroscopic Coronagraph (LASCO)", *Solar Phys.*, **162**, 357–402. [DOI], [ADS]

Bryans, P., McIntosh, S. W., De Moortel, I. and De Pontieu, B., 2016, "On the Connection between Propagating Solar Coronal Disturbances and Chromospheric Footpoints", *Astrophys. J. Lett.*, **829**, L18. [DOI], [ADS]

Byrne, J. P., 2015, "Investigating the kinematics of coronal mass ejections with the automated CORIMP catalog", *Journal of Space Weather and Space Climate*, **5**(27), A19. [DOI], [ADS], [arXiv:1506.04046 [astro-ph.SR]]

Byrne, J. P., Morgan, H., Habbal, S. R. and Gallagher, P. T., 2012, "Automatic Detection and Tracking of Coronal Mass Ejections. II. Multiscale Filtering of Coronagraph Images", *Astrophys. J.*, **752**, 145. [DOI], [ADS], [arXiv:1207.6125 [astro-ph.SR]]

Carrington, R. C., 1859, "Description of a Singular Appearance seen in the Sun on September 1, 1859", *Mon. Not. Roy. Astron. Soc.*, **20**, 13–15. [DOI], [ADS]

Chandrashekhar, K., Bemporad, A., Banerjee, D., Gupta, G. R. and Teriaca, L., 2014, "Characteristics of polar coronal hole jets", *Astron. Astrophys.*, **561**, A104. [DOI], [ADS], [arXiv:1310.8106 [astro-ph.SR]]

Clauset, A., Rohilla Shalizi, C. and Newman, M. E. J., 2007, "Power-law distributions in empirical data", *ArXiv e-prints*. [ADS], [arXiv:0706.1062 [physics.data-an]]

Cooper, F. C., Nakariakov, V. M. and Tsiklauri, D., 2003, "Line-of-sight effects on observability of kink and sausage modes in coronal structures with imaging telescopes", *Astron. Astrophys.*, **397**, 765–770. [DOI], [ADS], [astro-ph/0207167]

Cremades, H. and Bothmer, V., 2004, "On the three-dimensional configuration of coronal mass ejections", *Astron. Astrophys.*, **422**, 307–322. [DOI], [ADS]

Crosby, N. B., Aschwanden, M. J. and Dennis, B. R., 1993, "Frequency distributions and correlations of solar X-ray flare parameters", *Solar Phys.*, **143**, 275–299. [DOI], [ADS]

Culhane, L., Harra, L. K., Baker, D., van Driel-Gesztelyi, L., Sun, J., Doschek, G. A., Brooks, D. H., Lundquist, L. L., Kamio, S., Young, P. R. and Hansteen,

V. H., 2007, "Hinode EUV Study of Jets in the Sun's South Polar Corona", *Pub. Astron. Soc. Japan*, **59**, S751–S756. [DOI], [ADS]

Davies, J. A., Harrison, R. A., Perry, C. H., Möstl, C., Lugaz, N., Rollett, T., Davis, C. J., Crothers, S. R., Temmer, M., Eyles, C. J. and Savani, N. P., 2012, "A Self-similar Expansion Model for Use in Solar Wind Transient Propagation Studies", *Astrophys. J.*, **750**, 23. [DOI], [ADS]

Davis, C. J., Davies, J. A., Lockwood, M., Rouillard, A. P., Eyles, C. J. and Harrison, R. A., 2009, "Stereoscopic imaging of an Earth-impacting solar coronal mass ejection: A major milestone for the STEREO mission", *Geophys. Res. Lett.*, **36**, L08102. [DOI], [ADS]

Davis, C. J., Davies, J. A., St Cyr, O. C., Campbell-Brown, M., Skelt, A., Kaiser, M., Meyer-Vernet, N., Crothers, S., Lintott, C., Smith, A., Bamford, S. and Baeten, E. M. L., 2012, "The distribution of interplanetary dust between 0.96 and 1.04 au as inferred from impacts on the STEREO spacecraft observed by the heliospheric imagers", *Mon. Not. Roy. Astron. Soc.*, **420**, 1355–1366. [DOI], [ADS], [arXiv:1111.4389 [astro-ph.EP]]

De Moortel, I., Antolin, P. and Van Doorsselaere, T., 2015, "Observational Signatures of Waves and Flows in the Solar Corona", *Solar Phys.*, **290**, 399–421. [DOI], [ADS]

De Pontieu, B., McIntosh, S. W., Hansteen, V. H. and Schrijver, C. J., 2009, "Observing the Roots of Solar Coronal Heating–in the Chromosphere", *Astrophys. J. Lett.*, **701**, L1–L6. [DOI], [ADS], [arXiv:0906.5434 [astro-ph.SR]]

De Pontieu, B., Title, A. M., Lemen, J. R., Kushner, G. D., Akin, D. J., Allard, B., Berger, T., Boerner, P., Cheung, M., Chou, C., Drake, J. F., Duncan, D. W., Freeland, S., Heyman, G. F., Hoffman, C., Hurlburt, N. E., Lindgren, R. W., Mathur, D., Rehse, R., Sabolish, D., Seguin, R., Schrijver, C. J., Tarbell, T. D., Wülser, J.-P., Wolfson, C. J., Yanari, C., Mudge, J., Nguyen-Phuc, N., Timmons, R., van Bezooijen, R., Weingrod, I., Brookner, R., Butcher, G.,

Dougherty, B., Eder, J., Knagenhjelm, V., Larsen, S., Mansir, D., Phan, L., Boyle, P., Cheimets, P. N., DeLuca, E. E., Golub, L., Gates, R., Hertz, E., McKillop, S., Park, S., Perry, T., Podgorski, W. A., Reeves, K., Saar, S., Testa, P., Tian, H., Weber, M., Dunn, C., Eccles, S., Jaeggli, S. A., Kankelborg, C. C., Mashburn, K., Pust, N., Springer, L., Carvalho, R., Kleint, L., Marmie, J., Mazmanian, E., Pereira, T. M. D., Sawyer, S., Strong, J., Worden, S. P., Carlsson, M., Hansteen, V. H., Leenaarts, J., Wiesmann, M., Aloise, J., Chu, K.-C., Bush, R. I., Scherrer, P. H., Brekke, P., Martinez-Sykora, J., Lites, B. W., McIntosh, S. W., Uitenbroek, H., Okamoto, T. J., Gummin, M. A., Auker, G., Jerram, P., Pool, P. and Waltham, N., 2014, "The Interface Region Imaging Spectrograph (IRIS)", *Solar Phys.*, **289**, 2733–2779. [DOI], [ADS], [arXiv:1401.2491 [astro-ph.SR]]

Deforest, C. E. and Gurman, J. B., 1998, "Observation of Quasi-periodic Compressive Waves in Solar Polar Plumes", *Astrophys. J. Lett.*, **501**, L217. [DOI], [ADS]

Deforest, C. E., Hoeksema, J. T., Gurman, J. B., Thompson, B. J., Plunkett, S. P., Howard, R., Harrison, R. C. and Hassler, D. M., 1997, "Polar Plume Anatomy: Results of a Coordinated Observation", *Solar Phys.*, **175**, 393–410. [DOI], [ADS]

DeForest, C. E., Lamy, P. L. and Llebaria, A., 2001, "Solar Polar Plume Lifetime and Coronal Hole Expansion: Determination from Long-Term Observations", *Astrophys. J.*, **560**, 490–498. [DOI], [ADS]

D'Huys, E., Seaton, D. B., Poedts, S. and Berghmans, D., 2014, "Observational Characteristics of Coronal Mass Ejections without Low-coronal Signatures", *Astrophys. J.*, **795**, 49. [DOI], [ADS], [arXiv:1409.1422 [astro-ph.SR]]

D'Huys, E., Berghmans, D., Seaton, D. B. and Poedts, S., 2016, "The Effect of Limited Sample Sizes on the Accuracy of the Estimated Scaling Parameter for Power-Law-Distributed Solar Data", *Solar Phys.*, **291**, 1561–1576. [DOI], [ADS], [arXiv:1605.06972 [astro-ph.SR]]

Dolla, L. R. and Zhukov, A. N., 2011, "On the Nature of the Spectral Line Broadening in Solar Coronal Dimmings", *Astrophys. J.*, **730**, 113. [DOI], [ADS], [arXiv:1102.4745 [astro-ph.SR]]

Driesman, A., Hynes, S. and Cancro, G., 2008, "The STEREO Observatory", *Space Sci. Rev.*, **136**, 17–44. [DOI], [ADS]

Edwin, P. M. and Roberts, B., 1983, "Wave propagation in a magnetic cylinder", *Solar Phys.*, **88**, 179–191. [DOI], [ADS]

Eyles, C., Davis, C., Harrison, R., Waltham, N., Halain, J.-P., Mazy, E., Defise, J.-M., Howard, R., Moses, D., Newmark, J. and Plunkett, S., 2007, "In-orbit verification, calibration, and performance of the Heliospheric Imager on the STEREO mission", in *Society of Photo-Optical Instrumentation Engineers (SPIE) Conference Series*, Society of Photo-Optical Instrumentation Engineers (SPIE) Conference Series, 6689, [DOI], [ADS]

Eyles, C. J., Simnett, G. M., Cooke, M. P., Jackson, B. V., Buffington, A., Hick, P. P., Waltham, N. R., King, J. M., Anderson, P. A. and Holladay, P. E., 2003, "The Solar Mass Ejection Imager (Smei)", *Solar Phys.*, **217**, 319–347. [DOI], [ADS]

Eyles, C. J., Harrison, R. A., Davis, C. J., Waltham, N. R., Shaughnessy, B. M., Mapson-Menard, H. C. A., Bewsher, D., Crothers, S. R., Davies, J. A., Simnett, G. M., Howard, R. A., Moses, J. D., Newmark, J. S., Socker, D. G., Halain, J.-P., Defise, J.-M., Mazy, E. and Rochus, P., 2009, "The Heliospheric Imagers Onboard the STEREO Mission", *Solar Phys.*, **254**, 387–445. [DOI], [ADS]

Fang, X., Yuan, D., Van Doorsselaere, T., Keppens, R. and Xia, C., 2015, "Modeling of Reflective Propagating Slow-mode Wave in a Flaring Loop", *Astrophys. J.*, **813**, 33. [DOI], [ADS], [arXiv:1509.04536 [astro-ph.SR]]

Feng, L., Inhester, B., de Patoul, J., Wiegelmann, T. and Gan, W. Q., 2012, "Particle kinetic analysis of a polar jet from SECCHI COR data", *Astron. Astrophys.*, **538**, A34. [DOI], [ADS], [arXiv:1112.2255 [astro-ph.SR]]

Fisher, R. and Guhathakurta, M., 1995, "Physical Properties of Polar Coronal Rays and Holes as Observed with the SPARTAN 201-01 Coronagraph", *Astrophys. J. Lett.*, **447**, L139. [DOI], [ADS]

Gallagher, P. T., Phillips, K. J. H., Harra-Murnion, L. K., Baudin, F. and Keenan, F. P., 1999, "Transient events in the EUV transition region and chromosphere", *Astron. Astrophys.*, **348**, 251–260. [ADS]

Galvin, A. B., Kistler, L. M., Popecki, M. A., Farrugia, C. J., Simunac, K. D. C., Ellis, L., Möbius, E., Lee, M. A., Boehm, M., Carroll, J., Crawshaw, A., Conti, M., Demaine, P., Ellis, S., Gaidos, J. A., Googins, J., Granoff, M., Gustafson, A., Heirtzler, D., King, B., Knauss, U., Levasseur, J., Longworth, S., Singer, K., Turco, S., Vachon, P., Vosbury, M., Widholm, M., Blush, L. M., Karrer, R., Bochsler, P., Daoudi, H., Etter, A., Fischer, J., Jost, J., Opitz, A., Sigrist, M., Wurz, P., Klecker, B., Ertl, M., Seidenschwang, E., Wimmer-Schweingruber, R. F., Koeten, M., Thompson, B. and Steinfeld, D., 2008, "The Plasma and Suprathermal Ion Composition (PLASTIC) Investigation on the STEREO Observatories", *Space Sci. Rev.*, **136**, 437–486. [DOI], [ADS]

Gary, G. A., 1989, "Linear force-free magnetic fields for solar extrapolation and interpretation", *Astrophys. J. Suppl.*, **69**, 323–348. [DOI], [ADS]

Gonzalez, R. C. and Woods, R. E., 2002, *Digital image processing*. [ADS]

Goossens, M., Andries, J. and Aschwanden, M. J., 2002, "Coronal loop oscillations. An interpretation in terms of resonant absorption of quasi-mode kink oscillations", *Astron. Astrophys.*, **394**, L39–L42. [DOI], [ADS]

Goossens, M., Van Doorsselaere, T., Soler, R. and Verth, G., 2013, "Energy Content and Propagation in Transverse Solar Atmospheric Waves", *Astrophys. J.*, **768**, 191. [DOI], [ADS]

Gopalswamy, N., 2004, "A Global Picture of CMEs in the Inner Heliosphere", in *The Sun and the Heliosphere as an Integrated System*, (Eds.) Poletto, G., Suess, S. T., Astrophysics and Space Science Library, 317, [DOI], [ADS]

Gopalswamy, N., 2010, "Corona Mass Ejections: a Summary of Recent Results", in *20th National Solar Physics Meeting*, (Ed.) Dorotovic, I., [ADS]

Gopalswamy, N., 2016, "History and development of coronal mass ejections as a key player in solar terrestrial relationship", *Geoscience Letters*, **3**, 8. [DOI], [ADS], [arXiv:1602.03665 [astro-ph.SR]]

Gopalswamy, N., Lara, A., Lepping, R. P., Kaiser, M. L., Berdichevsky, D. and St. Cyr, O. C., 2000, "Interplanetary acceleration of coronal mass ejections", *Geophys. Res. Lett.*, **27**, 145–148. [DOI], [ADS]

Gopalswamy, N., Yashiro, S., Vourlidas, A., Lara, A., Stenborg, G., Kaiser, M. L. and Howard, R. A., 2004, "Coronal Mass Ejections When the Sun Went Wild", in *American Astronomical Society Meeting Abstracts #204*, Bulletin of the American Astronomical Society, 36, [ADS]

Gopalswamy, N., Yashiro, S., Michalek, G., Stenborg, G., Vourlidas, A., Freeland, S. and Howard, R., 2009, "The SOHO/LASCO CME Catalog", *Earth Moon and Planets*, **104**, 295–313. [DOI], [ADS]

Gopalswamy, N., Akiyama, S., Yashiro, S. and Mäkelä, P., 2010, "Coronal Mass Ejections from Sunspot and Non-Sunspot Regions", *Astrophysics and Space Science Proceedings*, **19**, 289–307. [DOI], [ADS], [arXiv:0903.1087 [astro-ph.SR]]

Gopalswamy, N., Akiyama, S., Yashiro, S., Xie, H., Mäkelä, P. and Michalek, G., 2014, "Anomalous expansion of coronal mass ejections during solar cycle 24 and its space weather implications", *Geophys. Res. Lett.*, **41**, 2673–2680. [DOI], [ADS], [arXiv:1404.0252 [astro-ph.SR]]

Gopalswamy, N., Tsurutani, B. and Yan, Y., 2015a, "Short-term variability of the Sun-Earth system: an overview of progress made during the CAWSES-II period", *Progress in Earth and Planetary Science*, **2**, 13. [DOI], [ADS], [arXiv:1504.06332 [astro-ph.SR]]

Gopalswamy, N., Xie, H., Akiyama, S., Mäkelä, P., Yashiro, S. and Michalek, G., 2015b, "The Peculiar Behavior of Halo Coronal Mass Ejections in Solar Cycle 24", *Astrophys. J. Lett.*, **804**, L23. [DOI], [ADS], [arXiv:1504.01797 [astro-ph.SR]]

Gosling, J. T. and Pizzo, V. J., 1999, "Formation and Evolution of Corotating Interaction Regions and their Three Dimensional Structure", *Space Sci. Rev.*, **89**, 21–52. [DOI], [ADS]

Grappin, R., Wang, Y.-M. and Pantellini, F., 2011, "Two-temperature Models for Polar Plumes: Cooling by Means of Strong Base Heating", *Astrophys. J.*, **727**, 30. [DOI], [ADS]

Gupta, G. R., O'Shea, E., Banerjee, D., Popescu, M. and Doyle, J. G., 2009, "On the statistical detection of propagating waves in polar coronal holes", *Astron. Astrophys.*, **493**, 251–257. [DOI], [ADS]

Hansen, R. T., Garcia, C. J., Grognard, R. J.-M. and Sheridan, K. V., 1971, "A coronal disturbance observed simultaneously with a white-light corona-meter and the 80 MHz Culgoora radioheliograph", *Proceedings of the Astronomical Society of Australia*, **2**, 57. [ADS]

Harrison, R. A, 2016, "", *in preperation*

Harrison, R. A., Davis, C. J., Eyles, C. J., Bewsher, D., Crothers, S. R., Davies, J. A., Howard, R. A., Moses, D. J., Socker, D. G., Newmark, J. S., Halain, J.-P., Defise, J.-M., Mazy, E., Rochus, P., Webb, D. F. and Simnett, G. M., 2008, "First Imaging of Coronal Mass Ejections in the Heliosphere Viewed from Outside the Sun Earth Line", *Solar Phys.*, **247**, 171–193. [DOI], [ADS]

Harrison, R. A., Davies, J. A., Rouillard, A. P., Davis, C. J., Eyles, C. J., Bewsher, D., Crothers, S. R., Howard, R. A., Sheeley, N. R., Vourlidas, A., Webb, D. F., Brown, D. S. and Dorrian, G. D., 2009, "Two Years of the STEREO Heliospheric Imagers. Invited Review", *Solar Phys.*, **256**, 219–237. [DOI], [ADS]

Harvey, J. W., 1965, "Coronal Polar Rays and Polar Magnetic Fields.", *Astrophys. J.*, **141**, 832. [DOI], [ADS]

Hollweg, J. V. and Yang, G., 1988, "Resonance absorption of compressible magnetohydrodynamic waves at thin 'surfaces'", *J. Geophys. Res.*, **93**, 5423–5436. [DOI], [ADS]

Hori, K., Ichimoto, K., Sakurai, T., Sano, I. and Nishino, Y., 2005, "Flare-associated Coronal Disturbances Observed with the Norikura Green-Line Imaging System. I. A Coronal Mass Ejection Onset", *Astrophys. J.*, **618**, 1001–1011. [DOI], [ADS]

Howard, R. A., Moses, J. D., Vourlidas, A., Newmark, J. S., Socker, D. G., Plunkett, S. P., Korendyke, C. M., Cook, J. W., Hurley, A., Davila, J. M., Thompson, W. T., St Cyr, O. C., Mentzell, E., Mehalick, K., Lemen, J. R., Wuelser, J. P., Duncan, D. W., Tarbell, T. D., Wolfson, C. J., Moore, A., Harrison, R. A., Waltham, N. R., Lang, J., Davis, C. J., Eyles, C. J., Mapson-Menard, H., Simnett, G. M., Halain, J. P., Defise, J. M., Mazy, E., Rochus, P., Mercier, R., Ravet, M. F., Delmotte, F., Auchere, F., Delaboudiniere, J. P., Bothmer, V., Deutsch, W., Wang, D., Rich, N., Cooper, S., Stephens, V., Maahs, G., Baugh, R., McMullin, D. and Carter, T., 2008, "Sun Earth Connection Coronal and Heliospheric Investigation (SECCHI)", *Space Sci. Rev.*, **136**, 67–115. [DOI], [ADS]

Howard, T. A. and DeForest, C. E., 2012, "The Thomson Surface. I. Reality and Myth", *Astrophys. J.*, **752**, 130. [DOI], [ADS]

Howard, T. A., Webb, D. F., Tappin, S. J., Mizuno, D. R. and Johnston, J. C., 2006, "Tracking halo coronal mass ejections from 0-1 AU and space weather forecasting using the Solar Mass Ejection Imager (SMEI)", *Journal of Geophysical Research (Space Physics)*, **111**, A04105. [DOI], [ADS]

Huang, Z., Madjarska, M. S., Xia, L., Doyle, J. G., Galsgaard, K. and Fu, H., 2014, "Explosive Events on a Subarcsecond Scale in IRIS Observations: A Case Study", *Astrophys. J.*, **797**, 88. [DOI], [ADS], [arXiv:1409.6425 [astro-ph.SR]]

Hundhausen, A. J., Sawyer, C. B., House, L., Illing, R. M. E. and Wagner, W. J., 1984, "Coronal mass ejections observed during the solar maximum mission - Latitude distribution and rate of occurrence", *J. Geophys. Res.*, **89**, 2639–2646. [DOI], [ADS]

Inhester, B., 2015, "Thomson Scattering in the Solar Corona", *ArXiv e-prints*. [ADS], [arXiv:1512.00651 [astro-ph.SR]]

Jahne, B., 1997, *Practical handbook on image processing for scientific applications*. [ADS]

Jiao, F., Xia, L., Li, B., Huang, Z., Li, X., Chandrashekhar, K., Mou, C. and Fu, H., 2015, "Sources of Quasi-periodic Propagating Disturbances above a Solar Polar Coronal Hole", *Astrophys. J. Lett.*, **809**, L17. [DOI], [ADS], [arXiv:1507.08440 [astro-ph.SR]]

Kahler, S. W. and Webb, D. F., 2007, "V arc interplanetary coronal mass ejections observed with the Solar Mass Ejection Imager", *Journal of Geophysical Research (Space Physics)*, **112**, A09103. [DOI], [ADS]

Kaiser, M. L., 2005, "The STEREO mission: an overview", *Advances in Space Research*, **36**, 1483–1488. [DOI], [ADS]

Kiddie, G., De Moortel, I., Del Zanna, G., McIntosh, S. W. and Whittaker, I., 2012, "Propagating Disturbances in Coronal Loops: A Detailed Analysis of Propagation Speeds", *Solar Phys.*, **279**, 427–452. [DOI], [ADS], [arXiv:1205.0891 [astro-ph.SR]]

Krishna Prasad, S., Banerjee, D., Van Doorsselaere, T. and Singh, J., 2012, "Omnipresent long-period intensity oscillations in open coronal structures", *Astron. Astrophys.*, **546**, A50. [DOI], [ADS], [arXiv:1209.2536 [astro-ph.SR]]

Kumar, P., Innes, D. E. and Inhester, B., 2013, "Solar Dynamics Observatory/Atmospheric Imaging Assembly Observations of a Reflecting Longitudinal Wave in a Coronal Loop", *Astrophys. J. Lett.*, **779**, L7. [DOI], [ADS], [arXiv:1409.3896 [astro-ph.SR]]

Kumar, P., Nakariakov, V. M. and Cho, K.-S., 2015, "X-Ray and EUV Observations of Simultaneous Short and Long Period Oscillations in Hot Coronal Arcade Loops", *Astrophys. J.*, **804**, 4. [DOI], [ADS], [arXiv:1502.07117 [astro-ph.SR]]

Lee, J., White, S. M., Kundu, M. R., Mikić , Z. and McClymont, A. N., 1999, "A Test for Coronal Magnetic Field Extrapolations", *Astrophys. J.*, **510**, 413–421. [DOI], [ADS]

Lemen, J. R., Title, A. M., Akin, D. J., Boerner, P. F., Chou, C., Drake, J. F., Duncan, D. W., Edwards, C. G., Friedlaender, F. M., Heyman, G. F., Hurlburt, N. E., Katz, N. L., Kushner, G. D., Levay, M., Lindgren, R. W., Mathur, D. P., McFeaters, E. L., Mitchell, S., Rehse, R. A., Schrijver, C. J., Springer, L. A., Stern, R. A., Tarbell, T. D., Wuelser, J.-P., Wolfson, C. J., Yanari, C., Bookbinder, J. A., Cheimets, P. N., Caldwell, D., Deluca, E. E., Gates, R., Golub, L., Park, S., Podgorski, W. A., Bush, R. I., Scherrer, P. H., Gummin, M. A., Smith, P., Auker, G., Jerram, P., Pool, P., Soufli, R., Windt, D. L., Beardsley, S., Clapp, M., Lang, J. and Waltham, N., 2012a, "The Atmospheric Imaging Assembly (AIA) on the Solar Dynamics Observatory (SDO)", *Solar Phys.*, **275**, 17–40. [DOI], [ADS]

Lemen, J. R., Title, A. M., Akin, D. J., Boerner, P. F., Chou, C., Drake, J. F., Duncan, D. W., Edwards, C. G., Friedlaender, F. M., Heyman, G. F., Hurlburt, N. E., Katz, N. L., Kushner, G. D., Levay, M., Lindgren, R. W., Mathur, D. P., McFeaters, E. L., Mitchell, S., Rehse, R. A., Schrijver, C. J., Springer, L. A., Stern, R. A., Tarbell, T. D., Wuelser, J.-P., Wolfson, C. J., Yanari, C., Bookbinder, J. A., Cheimets, P. N., Caldwell, D., Deluca, E. E., Gates, R., Golub, L., Park, S., Podgorski, W. A., Bush, R. I., Scherrer, P. H., Gummin, M. A., Smith, P., Auker, G., Jerram, P., Pool, P., Soufli, R., Windt, D. L.,

Beardsley, S., Clapp, M., Lang, J. and Waltham, N., 2012b, "The Atmospheric Imaging Assembly (AIA) on the Solar Dynamics Observatory (SDO)", *Solar Phys.*, **275**, 17–40. [DOI], [ADS]

Liu, W. and Ofman, L., 2014, "Advances in Observing Various Coronal EUV Waves in the SDO Era and Their Seismological Applications (Invited Review)", *Solar Phys.*, **289**, 3233–3277. [DOI], [ADS], [arXiv:1404.0670 [astro-ph.SR]]

Lugaz, N., Vourlidas, A. and Roussev, I. I., 2009, "Deriving the radial distances of wide coronal mass ejections from elongation measurements in the heliosphere - application to CME-CME interaction", *Annales Geophysicae*, **27**, 3479–3488. [DOI], [ADS], [arXiv:0909.0534 [astro-ph.SR]]

Luhmann, J. G., Curtis, D. W., Schroeder, P., McCauley, J., Lin, R. P., Larson, D. E., Bale, S. D., Sauvaud, J.-A., Aoustin, C., Mewaldt, R. A., Cummings, A. C., Stone, E. C., Davis, A. J., Cook, W. R., Kecman, B., Wiedenbeck, M. E., von Rosenvinge, T., Acuna, M. H., Reichenthal, L. S., Shuman, S., Wortman, K. A., Reames, D. V., Mueller-Mellin, R., Kunow, H., Mason, G. M., Walpole, P., Korth, A., Sanderson, T. R., Russell, C. T. and Gosling, J. T., 2008, "STEREO IMPACT Investigation Goals, Measurements, and Data Products Overview", *Space Sci. Rev.*, **136**, 117–184. [DOI], [ADS]

Luhmann, J. G., Li, Y., Liu, Y., Jian, L., Russell, C. T., Kilpua, E., Petrie, G. J. and Hoeksema, J. T., 2011, "Heliospheric Space Weather at the Start of Cycle 24", *AGU Fall Meeting Abstracts*. [ADS]

Luna, M., Terradas, J., Oliver, R. and Ballester, J. L., 2008, "Transverse Oscillations of Two Coronal Loops", *Astrophys. J.*, **676**, 717-727. [DOI], [ADS], [arXiv:0707.0758]

Luna, M., Terradas, J., Oliver, R. and Ballester, J. L., 2009, "Transverse Oscillations of Systems of Coronal loops", *Astrophys. J.*, **692**, 1582–1589. [DOI], [ADS], [arXiv:0809.4230]

Luna, M., Terradas, J., Oliver, R. and Ballester, J. L., 2010, "Transverse Oscillations of a Multi-stranded Loop", *Astrophys. J.*, **716**, 1371–1380. [DOI], [ADS], [arXiv:0912.4491 [astro-ph.SR]]

Madjarska, M. S., 2011, "Dynamics and plasma properties of an X-ray jet from SUMER, EIS, XRT, and EUVI A B simultaneous observations", *Astron. Astrophys.*, **526**, A19. [DOI], [ADS], [arXiv:1008.3983 [astro-ph.SR]]

Madjarska, M. S., Doyle, J. G. and de Pontieu, B., 2009, "Explosive Events Associated with a Surge", *Astrophys. J.*, **701**, 253–259. [DOI], [ADS], [arXiv:0906.2544 [astro-ph.SR]]

Mandal, S., Yuan, D., Fang, X., Banerjee, D., Pant, V. and Van Doorsselaere, T., 2016, "Reflection of Propagating Slow Magneto-acoustic Waves in Hot Coronal Loops: Multi-instrument Observations and Numerical Modeling", *Astrophys. J.*, **828**, 72. [DOI], [ADS], [arXiv:1604.08133 [astro-ph.SR]]

Manoharan, P. K. and Mujiber Rahman, A., 2011, "Coronal mass ejectionsPropagation time and associated internal energy", *Journal of Atmospheric and Solar-Terrestrial Physics*, **73**, 671–677. [DOI], [ADS], [arXiv:1011.3687 [astro-ph.SR]]

Markwardt, C. B., 2009, "Non-linear Least-squares Fitting in IDL with MPFIT", in *Astronomical Data Analysis Software and Systems XVIII*, (Eds.) Bohlender, D. A., Durand, D., Dowler, P., Astronomical Society of the Pacific Conference Series, 411, [ADS], [arXiv:0902.2850 [astro-ph.IM]]

Mathioudakis, M., Jess, D. B. and Erdélyi, R., 2013, "Alfvén Waves in the Solar Atmosphere. From Theory to Observations", *Space Sci. Rev.*, **175**, 1–27. [DOI], [ADS], [arXiv:1210.3625 [astro-ph.SR]]

McIntosh, S. W., Innes, D. E., de Pontieu, B. and Leamon, R. J., 2010, "STEREO observations of quasi-periodically driven high velocity outflows in polar plumes", *Astron. Astrophys.*, **510**, L2. [DOI], [ADS], [arXiv:1001.3377 [astro-ph.SR]]

Moreno-Insertis, F. and Galsgaard, K., 2013, "Plasma Jets and Eruptions in Solar Coronal Holes: A Three-dimensional Flux Emergence Experiment", *Astrophys. J.*, **771**, 20. [DOI], [ADS], [arXiv:1305.2201 [astro-ph.SR]]

Moreton, G. E. and Ramsey, H. E., 1960, "Recent Observations of Dynamical Phenomena Associated with Solar Flares", *Pub. Astron. Soc. Pac.*, **72**, 357. [DOI], [ADS]

Morgan, H., Byrne, J. P. and Habbal, S. R., 2012, "Automatically Detecting and Tracking Coronal Mass Ejections. I. Separation of Dynamic and Quiescent Components in Coronagraph Images", *Astrophys. J.*, **752**, 144. [DOI], [ADS]

Möstl, C., Amla, K., Hall, J. R., Liewer, P. C., De Jong, E. M., Colaninno, R. C., Veronig, A. M., Rollett, T., Temmer, M., Peinhart, V., Davies, J. A., Lugaz, N., Liu, Y. D., Farrugia, C. J., Luhmann, J. G., Vršnak, B., Harrison, R. A. and Galvin, A. B., 2014, "Connecting Speeds, Directions and Arrival Times of 22 Coronal Mass Ejections from the Sun to 1 AU", *Astrophys. J.*, **787**, 119. [DOI], [ADS], [arXiv:1404.3579 [astro-ph.SR]]

Mueller, D. A. N. and Antiochos, S. K., 2008, "A Mechanism for Coronal Hole Jets", *Ann. Geophys.*, **26**, 1–8. [DOI], [arXiv:0804.3995 [astro-ph]]

Nakariakov, V. M., 2000, "Flare-generated coronal loop oscillations: A tool for MHD coronal seismology", in *Waves in Dusty, Solar, and Space Plasmas*, (Eds.) Verheest, F., Goossens, M., Hellberg, M. A., Bharuthram, R., American Institute of Physics Conference Series, 537, [DOI], [ADS]

Nakariakov, V. M. and Ofman, L., 2001, "Determination of the coronal magnetic field by coronal loop oscillations", *Astron. Astrophys.*, **372**, L53–L56. [DOI], [ADS]

Nakariakov, V. M. and Verwichte, E., 2005, "Coronal Waves and Oscillations", *Living Reviews in Solar Physics*, **2**. [DOI], [ADS]

Nakariakov, V. M., Ofman, L., Deluca, E. E., Roberts, B. and Davila, J. M., 1999a, "TRACE observation of damped coronal loop oscillations: Implications for coronal heating", *Science*, **285**, 862–864. [DOI], [ADS]

Nakariakov, V. M., Ofman, L., Deluca, E. E., Roberts, B. and Davila, J. M., 1999b, "TRACE observation of damped coronal loop oscillations: Implications for coronal heating", *Science*, **285**, 862–864. [DOI], [ADS]

Newkirk, Jr., G. and Harvey, J., 1968, "Coronal Polar Plumes", *Solar Phys.*, **3**, 321–343. [DOI], [ADS]

Nishizuka, N. and Hara, H., 2011, "Spectroscopic Observations of Continuous Outflows and Propagating Waves from NOAA 10942 with Extreme Ultraviolet Imaging Spectrometer/Hinode", *Astrophys. J. Lett.*, **737**, L43. [DOI], [ADS]

Nisticò, G., Bothmer, V., Patsourakos, S. and Zimbardo, G., 2009, "Characteristics of EUV Coronal Jets Observed with STEREO/SECCHI", *Solar Phys.*, **259**, 87–108. [DOI], [ADS], [arXiv:0906.4407 [astro-ph.SR]]

Nisticò, G., Nakariakov, V. M. and Verwichte, E., 2013, "Decaying and decayless transverse oscillations of a coronal loop", *Astron. Astrophys.*, **552**, A57. [DOI], [ADS]

Ofman, L., 2009, "Three-Dimensional Magnetohydrodynamic Models of Twisted Multithreaded Coronal Loop Oscillations", *Astrophys. J.*, **694**, 502–511. [DOI], [ADS]

Ofman, L. and Wang, T., 2002, "Hot Coronal Loop Oscillations Observed by SUMER: Slow Magnetosonic Wave Damping by Thermal Conduction", *Astrophys. J. Lett.*, **580**, L85–L88. [DOI], [ADS]

Ofman, L., Romoli, M., Poletto, G., Noci, G. and Kohl, J. L., 1997, "Ultraviolet Coronagraph Spectrometer Observations of Density Fluctuations in the Solar Wind", *Astrophys. J. Lett.*, **491**, L111. [DOI], [ADS]

Ofman, L., Nakariakov, V. M. and Deforest, C. E., 1999, "Slow Magnetosonic Waves in Coronal Plumes", *Astrophys. J.*, **514**, 441–447. [DOI], [ADS]

Ofman, L., Wang, T. J. and Davila, J. M., 2012, "Slow Magnetosonic Waves and Fast Flows in Active Region Loops", *Astrophys. J.*, **754**, 111. [DOI], [ADS], [arXiv:1205.5732 [astro-ph.SR]]

Olmedo, O., Zhang, J., Wechsler, H., Poland, A. and Borne, K., 2008, "Automatic Detection and Tracking of Coronal Mass Ejections in Coronagraph Time Series", *Solar Phys.*, **248**, 485–499. [DOI], [ADS]

O'Shea, E., Banerjee, D. and Doyle, J. G., 2006, "Magnetoacoustic wave propagation in off-limb polar regions", *Astron. Astrophys.*, **452**, 1059–1068. [DOI], [ADS]

O'Shea, E., Srivastava, A. K., Doyle, J. G. and Banerjee, D., 2007, "Evidence for wave harmonics in cool loops", *Astron. Astrophys.*, **473**, L13–L16. [DOI], [ADS]

Pant, V., Dolla, L., Mazumder, R., Banerjee, D., Krishna Prasad, S. and Panditi, V., 2015, "Dynamics of On-disk Plumes as Observed with the Interface Region Imaging Spectrograph, the Atmospheric Imaging Assembly, and the Helioseismic and Magnetic Imager", *Astrophys. J.*, **807**, 71. [DOI], [ADS], [arXiv:1505.04473 [astro-ph.SR]]

Pant, V., Mazumder, R., Yuan, D., Banerjee, D., Srivastava, A. K. and Shen, Y., 2016a, "Simultaneous Longitudinal and Transverse Oscillations in an Active-Region Filament", *Solar Phys.*, **291**, 3303–3315. [DOI], [ADS], [arXiv:1611.03984 [astro-ph.SR]]

Pant, V., Willems, S., Rodriguez, L., Mierla, M., Banerjee, D. and Davies, J. A., 2016b, "Automated Detection of Coronal Mass Ejections in STEREO Heliospheric Imager Data", *Astrophys. J.*, **833**, 80. [DOI], [ADS], [arXiv:1610.01904 [astro-ph.SR]]

Pant, V., Tiwari, A., Yuan, D. and Banerjee, D., 2017, "First Imaging Observation of Standing Slow Wave in Coronal Fan Loops", *Astrophys. J. Lett.*, **847**, L5. [DOI], [ADS], [arXiv:1708.06946 [astro-ph.SR]]

Paraschiv, A. R., Lacatus, D. A., Badescu, T., Lupu, M. G., Simon, S., Sandu, S. G., Mierla, M. and Rusu, M. V., 2010, "Study of Coronal Jets During Solar Minimum Based on STEREO/SECCHI Observations", *Solar Phys.*, **264**, 365–375. [DOI], [ADS]

Payne-Scott, R., Yabsley, D. E. and Bolton, J. G., 1947, "Relative Times of Arrival of Bursts of Solar Noise on Different Radio Frequencies", *Nature*, **160**, 256–257. [DOI], [ADS]

Pesnell, W. D., Thompson, B. J. and Chamberlin, P. C., 2012, "The Solar Dynamics Observatory (SDO)", *Solar Phys.*, **275**, 3–15. [DOI], [ADS]

Petrie, G. J. D., 2013, "Solar Magnetic Activity Cycles, Coronal Potential Field Models and Eruption Rates", *Astrophys. J.*, **768**, 162. [DOI], [ADS], [arXiv:1303.1218 [astro-ph.SR]]

Petrie, G. J. D., 2015, "On the Enhanced Coronal Mass Ejection Detection Rate since the Solar Cycle 23 Polar Field Reversal", *Astrophys. J.*, **812**, 74. [DOI], [ADS], [arXiv:1508.06729 [astro-ph.SR]]

Plotnikov, I., Rouillard, A. P., Davies, J. A., Bothmer, V., Eastwood, J. P., Gallagher, P., Harrison, R. A., Kilpua, E., Möstl, C., Perry, C. H., Rodriguez, L., Lavraud, B., Génot, V., Pinto, R. F. and Sanchez-Diaz, E., 2016, "Long-Term Tracking of Corotating Density Structures Using Heliospheric Imaging", *Solar Phys.*, **291**, 1853–1875. [DOI], [ADS], [arXiv:1606.01127 [astro-ph.SR]]

Ramsey, H. E. and Smith, S. F., 1966, "Flare-initiated filamei it oscillations", *Astron. J.*, **71**, 197. [DOI], [ADS]

Raouafi, N.-E. and Stenborg, G., 2014, "Role of Transients in the Sustainability of Solar Coronal Plumes", *Astrophys. J.*, **787**, 118. [DOI], [ADS]

Raouafi, N.-E., Harvey, J. W. and Solanki, S. K., 2006, "Properties of Plasma Dynamics In The Polar Coronal Plumes", in *SOHO-17. 10 Years of SOHO and Beyond*, ESA Special Publication, 617, [ADS]

Raouafi, N.-E., Harvey, J. W. and Solanki, S. K., 2007, "Properties of Solar Polar Coronal Plumes Constrained by Ultraviolet Coronagraph Spectrometer Data", *Astrophys. J.*, **658**, 643–656. [DOI], [ADS], [astro-ph/0703745]

Raouafi, N.-E., Petrie, G. J. D., Norton, A. A., Henney, C. J. and Solanki, S. K., 2008, "Evidence for Polar Jets as Precursors of Polar Plume Formation", *Astrophys. J. Lett.*, **682**, L137–L140. [DOI], [ADS], [arXiv:0806.3045]

Riley, P., Schatzman, C., Cane, H. V., Richardson, I. G. and Gopalswamy, N., 2006, "On the Rates of Coronal Mass Ejections: Remote Solar and In Situ Observations", *Astrophys. J.*, **647**, 648–653. [DOI], [ADS]

Robbrecht, E. and Berghmans, D., 2004, "Automated recognition of coronal mass ejections (CMEs) in near-real-time data", *Astron. Astrophys.*, **425**, 1097–1106. [DOI], [ADS]

Robbrecht, E., Berghmans, D. and Van der Linden, R. A. M., 2009, "Automated LASCO CME Catalog for Solar Cycle 23: Are CMEs Scale Invariant?", *Astrophys. J.*, **691**, 1222–1234. [DOI], [ADS], [arXiv:0810.1252]

Roberts, B., Edwin, P. M. and Benz, A. O., 1984, "On coronal oscillations", *Astrophys. J.*, **279**, 857–865. [DOI], [ADS]

Robertson, D. and Ruderman, M. S., 2011, "Resonantly damped oscillations of two coronal loops", *Astron. Astrophys.*, **525**, A4. [DOI], [ADS]

Rosenberg, H., 1970, "Evidence for MHD Pulsations in the Solar Corona", *Astron. Astrophys.*, **9**, 159. [ADS]

Rouillard, A. P., Davies, J. A., Forsyth, R. J., Rees, A., Davis, C. J., Harrison, R. A., Lockwood, M., Bewsher, D., Crothers, S. R., Eyles, C. J., Hapgood, M.

and Perry, C. H., 2008, "First imaging of corotating interaction regions using the STEREO spacecraft", *Geophys. Res. Lett.*, **35**, L10110. [DOI], [ADS]

Rouillard, A. P., Davies, J. A., Lavraud, B., Forsyth, R. J., Savani, N. P., Bewsher, D., Brown, D. S., Sheeley, N. R., Davis, C. J., Harrison, R. A., Howard, R. A., Vourlidas, A., Lockwood, M., Crothers, S. R. and Eyles, C. J., 2010, "Intermittent release of transients in the slow solar wind: 1. Remote sensing observations", *Journal of Geophysical Research (Space Physics)*, **115**, A04103. [DOI], [ADS]

Rouppe van der Voort, L., De Pontieu, B., Pereira, T. M. D., Carlsson, M. and Hansteen, V., 2015, "Heating Signatures in the Disk Counterparts of Solar Spicules in Interface Region Imaging Spectrograph Observations", *Astrophys. J. Lett.*, **799**, L3. [DOI], [ADS], [arXiv:1412.4531 [astro-ph.SR]]

Ruderman, M. S. and Erdélyi, R., 2009, "Transverse Oscillations of Coronal Loops", *Space Sci. Rev.*, **149**, 199–228. [DOI], [ADS]

Ruderman, M. S. and Roberts, B., 2002, "The damping of coronal loop oscillations", *Astrophys. J.*, **577**, 475–486

Saito, K., 1958, "Polar Rays of the Solar Corona", *Pub. Astron. Soc. Japan*, **10**, 49. [ADS]

Saito, K., 1965, "Polar Rays of the Solar Corona, II.", *Pub. Astron. Soc. Japan*, **17**, 1. [ADS]

Saito, K. and Tanaka, Y., 1957, "Polar Faculae of the Sun", *Pub. Astron. Soc. Japan*, **9**, 106. [ADS]

Sakao, T., Kano, R., Narukage, N., Kotoku, J., Bando, T., DeLuca, E. E., Lundquist, L. L., Tsuneta, S., Harra, L. K., Katsukawa, Y., Kubo, M., Hara, H., Matsuzaki, K., Shimojo, M., Bookbinder, J. A., Golub, L., Korreck, K. E., Su, Y., Shibasaki, K., Shimizu, T. and Nakatani, I., 2007, "Continuous Plasma

Outflows from the Edge of a Solar Active Region as a Possible Source of Solar Wind", *Science*, **318**, 1585–1588. [DOI], [ADS]

Samanta, T., Pant, V. and Banerjee, D., 2015, "Propagating Disturbances in the Solar Corona and Spicular Connection", *Astrophys. J. Lett.*, **815**, L16. [DOI], [ADS], [arXiv:1511.07354 [astro-ph.SR]]

Sarkar, S., Pant, V., Srivastava, A. K. and Banerjee, D., 2016, "Transverse Oscillations in a Coronal Loop Triggered by a Jet", *Solar Phys.*, **291**, 3269–3288. [DOI], [ADS], [arXiv:1611.04063 [astro-ph.SR]]

Savani, N. P., Rouillard, A. P., Davies, J. A., Owens, M. J., Forsyth, R. J., Davis, C. J. and Harrison, R. A., 2009, "The radial width of a Coronal Mass Ejection between 0.1 and 0.4 AU estimated from the Heliospheric Imager on STEREO", *Annales Geophysicae*, **27**, 4349–4358. [DOI], [ADS]

Savcheva, A., Cirtain, J., Deluca, E. E., Lundquist, L. L., Golub, L., Weber, M., Shimojo, M., Shibasaki, K., Sakao, T., Narukage, N., Tsuneta, S. and Kano, R., 2007, "A Study of Polar Jet Parameters Based on Hinode XRT Observations", *Pub. Astron. Soc. Japan*, **59**, S771–S778. [DOI], [ADS]

Schou, J., Scherrer, P. H., Bush, R. I., Wachter, R., Couvidat, S., Rabello-Soares, M. C., Bogart, R. S., Hoeksema, J. T., Liu, Y., Duvall, T. L., Akin, D. J., Allard, B. A., Miles, J. W., Rairden, R., Shine, R. A., Tarbell, T. D., Title, A. M., Wolfson, C. J., Elmore, D. F., Norton, A. A. and Tomczyk, S., 2012, "Design and Ground Calibration of the Helioseismic and Magnetic Imager (HMI) Instrument on the Solar Dynamics Observatory (SDO)", *Solar Phys.*, **275**, 229–259. [DOI], [ADS]

Schrijver, C. J., Title, A. M., Berger, T. E., Fletcher, L., Hurlburt, N. E., Nightingale, R. W., Shine, R. A., Tarbell, T. D., Wolfson, J., Golub, L., Bookbinder, J. A., Deluca, E. E., McMullen, R. A., Warren, H. P., Kankelborg, C. C., Handy, B. N. and de Pontieu, B., 1999, "A new view of the solar outer atmosphere by

the Transition Region and Coronal Explorer", *Solar Phys.*, **187**, 261–302. [DOI], [ADS]

Schrijver, C. J., Aschwanden, M. J. and Title, A. M., 2002, "Transverse oscillations in coronal loops observed with TRACE I. An Overview of Events, Movies, and a Discussion of Common Properties and Required Conditions", *Solar Phys.*, **206**, 69–98. [DOI], [ADS]

Schwenn, R., 1996, "An Essay on Terminology, Myths and Known Facts: Solar Transient - Flare - CME - Driver Gas - Piston - BDE - Magnetic Cloud - Shock Wave - Geomagnetic Storm", *Astrophys. Space Sci.*, **243**, 187. [DOI], [ADS]

Schwenn, R., 2006, "Space Weather: The Solar Perspective", *Living Reviews in Solar Physics*, **3**, 2. [DOI], [ADS]

Sheeley, Jr., N. R., Herbst, A. D., Palatchi, C. A., Wang, Y.-M., Howard, R. A., Moses, J. D., Vourlidas, A., Newmark, J. S., Socker, D. G., Plunkett, S. P., Korendyke, C. M., Burlaga, L. F., Davila, J. M., Thompson, W. T., St. Cyr, O. C., Harrison, R. A., Davis, C. J., Eyles, C. J., Halain, J. P., Wang, D., Rich, N. B., Battams, K., Esfandiari, E. and Stenborg, G., 2008a, "Heliospheric Images of the Solar Wind at Earth", *Astrophys. J.*, **675**, 853-862. [DOI], [ADS]

Sheeley, Jr., N. R., Herbst, A. D., Palatchi, C. A., Wang, Y.-M., Howard, R. A., Moses, J. D., Vourlidas, A., Newmark, J. S., Socker, D. G., Plunkett, S. P., Korendyke, C. M., Burlaga, L. F., Davila, J. M., Thompson, W. T., St. Cyr, O. C., Harrison, R. A., Davis, C. J., Eyles, C. J., Halain, J. P., Wang, D., Rich, N. B., Battams, K., Esfandiari, E. and Stenborg, G., 2008b, "SECCHI Observations of the Sun's Garden-Hose Density Spiral", *Astrophys. J. Lett.*, **674**, L109. [DOI], [ADS]

Shen, Y., Liu, Y. D., Chen, P. F. and Ichimoto, K., 2014, "Simultaneous Transverse Oscillations of a Prominence and a Filament and Longitudinal Oscillation of Another Filament Induced by a Single Shock Wave", *Astrophys. J.*, **795**, 130. [DOI], [ADS], [arXiv:1409.1304 [astro-ph.SR]]

Shibata, K., Ishido, Y., Acton, L. W., Strong, K. T., Hirayama, T., Uchida, Y., McAllister, A. H., Matsumoto, R., Tsuneta, S., Shimizu, T., Hara, H., Sakurai, T., Ichimoto, K., Nishino, Y. and Ogawara, Y., 1992, "Observations of X-ray jets with the YOHKOH Soft X-ray Telescope", *Pub. Astron. Soc. Japan*, **44**, L173–L179. [ADS]

Shibata, K., Nitta, N., Strong, K. T., Matsumoto, R., Yokoyama, T., Hirayama, T., Hudson, H. and Ogawara, Y., 1994, "A gigantic coronal jet ejected from a compact active region in a coronal hole", *Astrophys. J. Lett.*, **431**, L51–L53. [DOI], [ADS]

Shibata, K., Masuda, S., Shimojo, M., Hara, H., Yokoyama, T., Tsuneta, S., Kosugi, T. and Ogawara, Y., 1995, "Hot-Plasma Ejections Associated with Compact-Loop Solar Flares", *Astrophys. J. Lett.*, **451**, L83. [DOI], [ADS]

Shibata, K., Nakamura, T., Matsumoto, T., Otsuji, K., Okamoto, T. J., Nishizuka, N., Kawate, T., Watanabe, H., Nagata, S., UeNo, S., Kitai, R., Nozawa, S., Tsuneta, S., Suematsu, Y., Ichimoto, K., Shimizu, T., Katsukawa, Y., Tarbell, T. D., Berger, T. E., Lites, B. W., Shine, R. A. and Title, A. M., 2007, "Chromospheric Anemone Jets as Evidence of Ubiquitous Reconnection", *Science*, **318**, 1591–. [DOI], [ADS], [arXiv:0810.3974]

Shimojo, M. and Shibata, K., 2000, "Physical Parameters of Solar X-Ray Jets", *Astrophys. J.*, **542**, 1100–1108. [DOI], [ADS]

Socker, D. G., Howard, R. A., Korendyke, C. M., Simnett, G. M. and Webb, D. F., 2000, "NASA Solar Terrestrial Relations Observatory (STEREO) mission heliospheric imager", in *Instrumentation for UV/EUV Astronomy and Solar Missions*, (Eds.) Fineschi, S., Korendyke, C. M., Siegmund, O. H., Woodgate, B. E., , 4139, [DOI], [ADS]

Sonett, C. P., Colburn, D. S., Davis, L., Smith, E. J. and Coleman, P. J., 1964, "Evidence for a Collision-Free Magnetohydrodynamic Shock in Interplanetary Space", *Physical Review Letters*, **13**, 153–156. [DOI], [ADS]

Srivastava, A. K. and Dwivedi, B. N., 2010, "Signature of slow acoustic oscillations in a non-flaring loop observed by EIS/Hinode", *New Astronomy*, **15**, 8–15. [DOI], [ADS]

St. Cyr, O. C., Burkepile, J. T., Hundhausen, A. J. and Lecinski, A. R., 1999, "A comparison of ground-based and spacecraft observations of coronal mass ejections from 1980-1989", *J. Geophys. Res.*, **104**, 12 493–12 506. [DOI], [ADS]

Tappin, S. J. and Howard, T. A., 2009, "Direct Observation of a Corotating Interaction Region by Three Spacecraft", *Astrophys. J.*, **702**, 862–870. [DOI], [ADS]

Tappin, S. J., Howard, T. A., Hampson, M. M., Thompson, R. N. and Burns, C. E., 2012, "On the autonomous detection of coronal mass ejections in heliospheric imager data", *Journal of Geophysical Research (Space Physics)*, **117**, A05103. [DOI], [ADS]

Tappin, S. J., Eyles, C. J. and Davies, J. A., 2016, "", *Solar Phys.*, p. Submitted

Taroyan, Y. and Bradshaw, S., 2008, "Coronal loop oscillations and diagnostics with Hinode/EIS", *Astron. Astrophys.*, **481**, 247–252. [DOI], [ADS]

Taroyan, Y., Erdélyi, R., Doyle, J. G. and Bradshaw, S. J., 2005, "Footpoint excitation of standing acoustic waves in coronal loops", *Astron. Astrophys.*, **438**, 713–720. [DOI], [ADS]

Taroyan, Y., Erdélyi, R., Wang, T. J. and Bradshaw, S. J., 2007, "Forward Modeling of Hot Loop Oscillations Observed by SUMER and SXT", *Astrophys. J. Lett.*, **659**, L173–L176. [DOI], [ADS]

Terradas, J., Arregui, I., Oliver, R., Ballester, J. L., Andries, J. and Goossens, M., 2008, "Resonant Absorption in Complicated Plasma Configurations: Applications to Multistranded Coronal Loop Oscillations", *Astrophys. J.*, **679**, 1611-1620. [DOI], [ADS], [arXiv:0802.0591]

Thompson, W. T., 2006, "Coordinate systems for solar image data", *Astron. Astrophys.*, **449**, 791–803. [DOI], [ADS]

Tian, H., McIntosh, S. W. and De Pontieu, B., 2011a, "The Spectroscopic Signature of Quasi-periodic Upflows in Active Region Timeseries", *Astrophys. J. Lett.*, **727**, L37. [DOI], [ADS], [arXiv:1012.5112 [astro-ph.SR]]

Tian, H., McIntosh, S. W., De Pontieu, B., Martínez-Sykora, J., Sechler, M. and Wang, X., 2011b, "Two Components of the Solar Coronal Emission Revealed by Extreme-ultraviolet Spectroscopic Observations", *Astrophys. J.*, **738**, 18. [DOI], [ADS], [arXiv:1106.1141 [astro-ph.SR]]

Tian, H., McIntosh, S. W., Habbal, S. R. and He, J., 2011c, "Observation of High-speed Outflow on Plume-like Structures of the Quiet Sun and Coronal Holes with Solar Dynamics Observatory/Atmospheric Imaging Assembly", *Astrophys. J.*, **736**, 130. [DOI], [ADS], [arXiv:1105.3119 [astro-ph.SR]]

Tian, H., McIntosh, S. W., Wang, T., Ofman, L., De Pontieu, B., Innes, D. E. and Peter, H., 2012, "Persistent Doppler Shift Oscillations Observed with Hinode/EIS in the Solar Corona: Spectroscopic Signatures of Alfvénic Waves and Recurring Upflows", *Astrophys. J.*, **759**, 144. [DOI], [ADS], [arXiv:1209.5286 [astro-ph.SR]]

Tian, H., DeLuca, E. E., Cranmer, S. R., De Pontieu, B., Peter, H., Martínez-Sykora, J., Golub, L., McKillop, S., Reeves, K. K., Miralles, M. P., McCauley, P., Saar, S., Testa, P., Weber, M., Murphy, N., Lemen, J., Title, A., Boerner, P., Hurlburt, N., Tarbell, T. D., Wuelser, J. P., Kleint, L., Kankelborg, C., Jaeggli, S., Carlsson, M., Hansteen, V. and McIntosh, S. W., 2014, "Prevalence of small-scale jets from the networks of the solar transition region and chromosphere", *Science*, **346**(27), 1255711. [DOI], [ADS], [arXiv:1410.6143 [astro-ph.SR]]

Torrence, Christopher and Compo, Gilbert P., 1998, "A Practical Guide to Wavelet Analysis", *Bulletin of the American Meteorological Society*, **79**, 61–78

Tousey, R., 1973, "The solar corona.", in *Space Research Conference*, (Eds.) Rycroft, M. J., Runcorn, S. K., Space Research Conference, 2, [ADS]

Tsiklauri, D., Nakariakov, V. M., Arber, T. D. and Aschwanden, M. J., 2004, "Flare-generated acoustic oscillations in solar and stellar coronal loops", *Astron. Astrophys.*, **422**, 351–355. [DOI], [ADS], [astro-ph/0402261]

Uchida, Y., 1970, "Diagnosis of Coronal Magnetic Structure by Flare-Associated Hydromagnetic Disturbances", *Pub. Astron. Soc. Japan*, **22**, 341–364. [ADS]

van de Hulst, H. C., 1950, "On the polar rays of the corona (Errata: 11 VIII)", *Bulletin of the Astronomical Institutes of the Netherlands*, **11**, 150. [ADS]

Van Doorsselaere, T., Ruderman, M. S. and Robertson, D., 2008, "Transverse oscillations of two parallel coronal loops", *Astron. Astrophys.*, **485**, 849–857. [DOI], [ADS]

Velli, M., Lionello, R., Linker, J. A. and Mikić, Z., 2011, "Coronal Plumes in the Fast Solar Wind", *Astrophys. J.*, **736**, 32. [DOI], [ADS]

Vernazza, J. E., Avrett, E. H. and Loeser, R., 1981, "Structure of the solar chromosphere. III - Models of the EUV brightness components of the quiet-sun", *Astrophys. J. Suppl.*, **45**, 635–725. [DOI], [ADS]

Verwichte, E., Aschwanden, M. J., Van Doorsselaere, T., Foullon, C. and Nakariakov, V. M., 2009, "Seismology of a Large Solar Coronal Loop from EUVI/STEREO Observations of its Transverse Oscillation", *Astrophys. J.*, **698**, 397–404. [DOI], [ADS]

Verwichte, E., Foullon, C. and Van Doorsselaere, T., 2010a, "Spatial Seismology of a Large Coronal Loop Arcade from TRACE and EIT Observations of its Transverse Oscillations", *Astrophys. J.*, **717**, 458–467. [DOI], [ADS]

Verwichte, E., Marsh, M., Foullon, C., Van Doorsselaere, T., De Moortel, I., Hood, A. W. and Nakariakov, V. M., 2010b, "Periodic Spectral Line Asymmetries in Solar Coronal Structures from Slow Magnetoacoustic Waves", *Astrophys. J. Lett.*, **724**, L194–L198. [DOI], [ADS]

Vourlidas, A. and Howard, R. A., 2006, "The Proper Treatment of Coronal Mass Ejection Brightness: A New Methodology and Implications for Observations", *Astrophys. J.*, **642**, 1216–1221. [DOI], [ADS]

Wang, T., 2011, "Standing Slow-Mode Waves in Hot Coronal Loops: Observations, Modeling, and Coronal Seismology", *Space Sci. Rev.*, **158**, 397–419. [DOI], [ADS], [arXiv:1011.2483 [astro-ph.SR]]

Wang, T., Solanki, S. K., Curdt, W., Innes, D. E. and Dammasch, I. E., 2002, "Doppler Shift Oscillations of Hot Solar Coronal Plasma Seen by SUMER: A Signature of Loop Oscillations?", *Astrophys. J. Lett.*, **574**, L101–L104. [DOI], [ADS]

Wang, T., Ofman, L., Davila, J. M. and Su, Y., 2012, "Growing Transverse Oscillations of a Multistranded Loop Observed by SDO/AIA", *Astrophys. J. Lett.*, **751**, L27. [DOI], [ADS], [arXiv:1204.1376 [astro-ph.SR]]

Wang, T., Ofman, L. and Davila, J. M., 2013, "Three-dimensional Magnetohydrodynamic Modeling of Propagating Disturbances in Fan-like Coronal Loops", *Astrophys. J. Lett.*, **775**, L23. [DOI], [ADS], [arXiv:1308.0282 [astro-ph.SR]]

Wang, T., Ofman, L., Sun, X., Provornikova, E. and Davila, J. M., 2015, "Evidence of Thermal Conduction Suppression in a Solar Flaring Loop by Coronal Seismology of Slow-mode Waves", *Astrophys. J. Lett.*, **811**, L13. [DOI], [ADS], [arXiv:1509.00920 [astro-ph.SR]]

Wang, T. J., Solanki, S. K., Curdt, W., Innes, D. E., Dammasch, I. E. and Kliem, B., 2003a, "Hot coronal loop oscillations observed with SUMER: Examples and statistics", *Astron. Astrophys.*, **406**, 1105–1121. [DOI], [ADS]

Wang, T. J., Solanki, S. K., Innes, D. E., Curdt, W. and Marsch, E., 2003b, "Slow-mode standing waves observed by SUMER in hot coronal loops", *Astron. Astrophys.*, **402**, L17–L20. [DOI], [ADS]

Wang, T. J., Solanki, S. K., Innes, D. E. and Curdt, W., 2005, "Initiation of hot coronal loop oscillations: Spectral features", *Astron. Astrophys.*, **435**, 753–764. [DOI], [ADS]

Wang, Y.-M. and Colaninno, R., 2014, "Is Solar Cycle 24 Producing More Coronal Mass Ejections Than Cycle 23?", *Astrophys. J. Lett.*, **784**, L27. [DOI], [ADS]

Wang, Y.-M. and Muglach, K., 2008, "Observations of Low-Latitude Coronal Plumes", *Solar Phys.*, **249**, 17–35. [DOI], [ADS]

Wang, Y.-M. and Sheeley, Jr., N. R., 1995, "Coronal Plumes and Their Relationship to Network Activity", *Astrophys. J.*, **452**, 457. [DOI], [ADS]

Webb, D. F. and Howard, R. A., 1994, "The solar cycle variation of coronal mass ejections and the solar wind mass flux", *J. Geophys. Res.*, **99**, 4201–4220. [DOI], [ADS]

Webb, D. F. and Howard, T. A., 2012, "Coronal Mass Ejections: Observations", *Living Reviews in Solar Physics*, **9**, 3. [DOI], [ADS]

White, R. S. and Verwichte, E., 2012, "Transverse coronal loop oscillations seen in unprecedented detail by AIA/SDO", *Astron. Astrophys.*, **537**, A49. [DOI], [ADS]

Wilhelm, K., Abbo, L., Auchère, F., Barbey, N., Feng, L., Gabriel, A. H., Giordano, S., Imada, S., Llebaria, A., Matthaeus, W. H., Poletto, G., Raouafi, N.-E., Suess, S. T., Teriaca, L. and Wang, Y.-M., 2011, "Morphology, dynamics and plasma parameters of plumes and inter-plume regions in solar coronal holes", *Astron. Astrophys. Rev.*, **19**, 35. [DOI], [ADS], [arXiv:1103.4481 [astro-ph.SR]]

Woods, T. N., Eparvier, F. G., Hock, R., Jones, A. R., Woodraska, D., Judge, D., Didkovsky, L., Lean, J., Mariska, J., Warren, H., McMullin, D., Chamberlin, P., Berthiaume, G., Bailey, S., Fuller-Rowell, T., Sojka, J., Tobiska, W. K. and Viereck, R., 2012, "Extreme Ultraviolet Variability Experiment (EVE) on

the Solar Dynamics Observatory (SDO): Overview of Science Objectives, Instrument Design, Data Products, and Model Developments", *Solar Phys.*, **275**, 115–143. [DOI], [ADS]

Yashiro, S., Gopalswamy, N., Michalek, G., St. Cyr, O. C., Plunkett, S. P., Rich, N. B. and Howard, R. A., 2004, "A catalog of white light coronal mass ejections observed by the SOHO spacecraft", *Journal of Geophysical Research (Space Physics)*, **109**, A07105. [DOI], [ADS]

Yashiro, S., Akiyama, S., Gopalswamy, N. and Howard, R. A., 2006, "Different Power-Law Indices in the Frequency Distributions of Flares with and without Coronal Mass Ejections", *Astrophys. J. Lett.*, **650**, L143–L146. [DOI], [ADS], [astro-ph/0609197]

Yashiro, S., Michalek, G. and Gopalswamy, N., 2008, "A comparison of coronal mass ejections identified by manual and automatic methods", *Annales Geophysicae*, **26**, 3103–3112. [DOI], [ADS]

Young, P. R., Klimchuk, J. A. and Mason, H. E., 1999, "Temperature and density in a polar plume - measurements from CDS/SOHO", *Astron. Astrophys.*, **350**, 286–301. [ADS]

Yuan, D., Nakariakov, V. M., Chorley, N. and Foullon, C., 2011, "Leakage of long-period oscillations from the chromosphere to the corona", *Astron. Astrophys.*, **533**, A116. [DOI], [ADS]

Yuan, D., Van Doorsselaere, T., Banerjee, D. and Antolin, P., 2015, "Forward Modeling of Standing Slow Modes in Flaring Coronal Loops", *Astrophys. J.*, **807**, 98. [DOI], [ADS], [arXiv:1504.07475 [astro-ph.SR]]

Yuan, D., Su, J., Jiao, F. and Walsh, R. W., 2016, "Stochastic Transients as a Source of Quasi-periodic Processes in the Solar Atmosphere", *Astrophys. J. Suppl.*, **224**, 30. [DOI], [ADS], [arXiv:1603.08977 [astro-ph.SR]]

Zimovets, I. V. and Nakariakov, V. M., 2015a, "Excitation of kink oscillations of coronal loops: statistical study", *Astron. Astrophys.*, **577**, A4. [DOI], [ADS]

Zimovets, I. V. and Nakariakov, V. M., 2015b, "Excitation of kink oscillations of coronal loops: statistical study", *Astron. Astrophys.*, **577**, A4. [DOI], [ADS]

Zurbuchen, T. H. and Richardson, I. G., 2006, "In-Situ Solar Wind and Magnetic Field Signatures of Interplanetary Coronal Mass Ejections", *Space Sci. Rev.*, **123**, 31–43. [DOI], [ADS]